ABSTRACT

Title of dissertation: PHOTONIC ENGINEERING OF ABSORPTION AND EMISSION IN PHOTOVOLTAICS

Yunlu Xu, Doctor of Philosophy, 2016

Dissertation directed by: Professor Jeremy N. Munday
Department of Electrical and Computer Engineering

As modern society advances, the demand for clean and renewable energy resources becomes more and more important. The sun is by far the most abundant source of renewable energy and is indirectly responsible for many other energy resources on earth (e.g. sunlight enables photosynthesis, biofuels, wind, and even carbon-based fuels). A solar cell directly converts the energy of solar illumination into electricity through the photovoltaic effect and is expected to play a crucial role in the future total power generation globally. Our work has focused on photonic approaches to improving the conversion efficiency of solar cells. Toward this goal, we present results describing the use of quantum dot emission to redirect light within a solar cell, as well as the modification of absorption and emission of light from a solar cell using nanostructures and thin films to increase the efficiency to approach (or possibly surpass) the currently understood efficiency limits for traditional devices. The Shockley-Queisser (SQ) limit describes the maximum solar power conversion efficiency achievable for a p-n junction composed of a particular material and is the

standard by which new photovoltaic technologies are compared. This limit is based on the principle of detailed balance, which equates the photon flux into a device to the particle flux (photons or electrons) out of that device. Based on this theory, we describe how the efficiency of a photovoltaic cell is altered in the presence of new anti-reflection coatings, nanotexturing (e.g. plasmonic nanoparticle, nanowire), and more advanced photonic structures (e.g. photonic crystals) that are capable of modifying the absorption and emission of photons.

Nanostructured solar cells represent a novel class of photovoltaic devices. By careful selection of materials, as well as particle shapes and positions, the device performance can be improved by increasing the optical path length for scattered light, improving the modal distribution of the light within the absorber, and increasing light concentration (or angle restriction). For example, nanowires can yield microscale concentration effects to improve device performance; however, it has been unclear whether or not they can exceed the Shockley-Queisser limit. We show that single-junction nanostructured solar cells have a theoretical maximum efficiency of $\sim$ 42% under AM 1.5 solar illumination. While this exceeds the efficiency of a non-concentrating planar device, it does not exceed the Shockley-Queisser limit for a planar device with optical concentration. For practical devices, we include the effect of diffuse illumination and find that with the modest optical concentration available from nanostructures ($\times$ 1,000), an efficiency of 35.5% is achievable even with 25% diffusive solar radiation.

Finally, we discuss how photon emission modification offers an approach for low bandgap materials to achieve higher efficiencies. By incorporating specifically

designed photonic structures that restrict the absorption and emission of above bandgap photons, the bandgap of materials can be effectively tuned. Similarly, restriction of the emission angle leads to increased optical concentration. For realistic devices, we consider how both of these effects are affected by non-ideal materials and photonic structures. We find that the photonic crystal bandgap required to achieve maximum efficiency depends critically on the reflectivity of the photonic crystal. We experimentally demonstrated that the semiconductor bandgap of a material need not be an intrinsic property of that material but can be changed through photonic structuring of the surrounding layers. GaAs has a natural bandgap of 1.43 eV; however, we show that optical reflectors can be used to induce photon-recycling effects, which result in a bandgap shift of 0.13 eV. When a p-n junction is created within the GaAs, we find that its electrical properties are also shifted resulting in a 1.71 mV improvement in the open-circuit voltage of the device under 0.6 suns equivalent illumination. These results show that both the optical and electrical properties of a semiconductor can be modified purely by photonic manipulation, which enables a fundamentally new method for designing semiconductor structures and devices. We anticipate that our result will enable a range of optoelectronic devices.

PHOTONIC ENGINEERING OF ABSORPTION AND EMISSION IN PHOTOVOLTAICS

by

Yunlu Xu

Dissertation submitted to the Faculty of the Graduate School of the
University of Maryland, College Park in partial fulfillment
of the requirements for the degree of
Doctor of Philosophy
2016

Advisory Committee:
Professor Jeremy N. Munday/Advisor
Professor Edo Waks
Professor Julius Goldhar
Professor Steve Rolston
Professor Steven Anlage

To my father Jian Xu

and

mother Meiyun Wang

For their continuous support and unconditional love.

Acknowledgments

Pursuing doctoral degree is like taking a trip of adventure, the process is filled with significant challenges. It takes enthusiasm, passion and determination to explore the unknown world of science. I feel blessed to work with and learn from so many extraordinary scientists, researchers and staff members at the University of Maryland.

First and foremost, I would like to express my greatest gratitude to my academic and research advisor Professor Jeremy N. Munday for his constant patience, motivation and support throughout my doctoral study. Professor Munday has always been generous with his time, insight and attention. It has been a great pleasure to work with and learn from such an extraordinary and excellent scientist.

I would like to thank all members of Munday Lab-Dakang Ma, Dan Goldman, David Somers, Dongheon Ha, Joe Garret, Joseph Murray, Lisa Krayer and Tao Gong for their help throughout my time at the University of Maryland. In particular, I would like to thank my officemates Dongheon Ha, Joseph Murray and Tao Gong for their discussions and inspirations.

I wish to thank all members of my dissertation committee, namely Professor Jeremy Munday, Professor Edo Waks, Professor Julius Goldhar, Professor Steve Rolston and Professor Steven Anlage for sparing their precious time and effort.

My sincere gratitude also goes to Professor Edo Waks, Professor Marina Leite and Professor Liangbing Hu for their generosity in sharing resources and insights. I'm also grateful to their students Dr. Jehyung Kim, Sabyasachi Barik, Beth Ten-

nyson, Dr. Jiayu Wan and Dr. Colin Preston for their help with the theoretical and experimental work.

I would also like to give my thanks to the staff members in the Nanocenter at University of Maryland−Tom Loughran, Jonathan Hummel, John Abrahams and Mark Lecatesand, who have provided great support in tools for fabrication and measurement.

I owe my deepest thanks to all of my family members who have always stood by me and guided me in every struggle and pain that I have gone through.

Yunlu Xu

07/18/2016

University of Maryland

Table of Contents

List of Tables

List of Figures

List of Publications

Yunlu Xu et al., All-photonic semiconductor bandgap engineering through photon-recycling. (manuscript in preparation)

Yunlu Xu, Tao Gong and Jeremy N. Munday, The generalized Shockley-Queisser limit for nanostructured solar cells. *Scientific reports*, **5** (2015).

Yunlu Xu, Edo Waks and Jeremy N. Munday, Improved voltage response in III-V solar cells based on engineered spontaneous emission. *IEEE 42nd Photovoltaic Specialist Conference (PVSC)*, 1-4 (2015).

Jeremy N. Munday and **Yunlu Xu**, Photonic Crystal Devices for Energy Applications. *Frontiers in Optics 2015, OSA Technical Digest (online) (Optical Society of America, 2015)*, paper FTu3C.2 (2015).

Yunlu Xu and Jeremy N. Munday, Designing photonic materials for effective bandgap modification and optical concentration in photovoltaics. *IEEE Journal of Photovoltaics*, **4**, 233-236 (2014).

Yunlu Xu and Jeremy N. Munday, Light trapping in a polymer solar cell by tailored quantum dot emission. *Optics express*, **22**, A259-A267 (2014).

Yunlu Xu, Joseph Murray and Jeremy N. Munday, Photonics and Plasmonics for Enhanced Photovoltaic Performance. *Quantum Dot Solar Cells*, 349-382 (2014).

Wenzhong Bao, Jiayu Wan, Xiaogang Han, Xinghan Cai, Hongli Zhu, Dohun Kim, Dakang Ma, **Yunlu Xu**, Jeremy N Munday, H Dennis Drew, Michael S Fuhrer and Liangbing Hu, Approaching the limits of transparency and conductivity in graphitic materials through lithium intercalation. *Nature communications*, **5** (2014).

Colin Preston, **Yunlu Xu**, Xiaogang Han, Jeremy N. Munday and Liangbing Hu, Optical haze of transparent and conductive silver nanowire films. *Nano Research*, **6**, 461-468 (2013).

List of Abbreviations and Key Variables

IREAP	Institute for Research in Electronics and Applied Physics
USEIA	United States Energy Information Administration
PV	Photovoltaic
QD	Quantum dots
NW	Nanowire
PL	Photoluminescence
IQY	Internal (florescence) quantum yield
TM	transverse magnetic
TE	transverse electric
ARC	Anti-reflection coating
PC	Photonic crystal
V_{oc}	Open circuit voltage
J_{sc}	Short circuit current density
I_{sc}	Short circuit current
J_L	Light generated current density
I_L	Light generated current
J_R	Reverse saturation current density
I_R	Reverse saturation current
J_D	Dark current density
I_D	Dark current
A_{cell}	Surface area of the solar cell
k_B	Boltzmann constant
T_c	Temperature of the cell
T_s	Temperature of the sun
θ_s	Emission angle from the sun
θ_c	Emission angle from the device
h	Plank constant
n	Ideality factor
q	Charge of a single electron
R_s	Series resistance of the solar cell
R_c	Shunt resistance of the solar cell

FF	Fill factor
α	Absorptivity of a material
κ	Imaginary part of the refractive index of a material
a	Absorption of a device
D_p	Diameter of the scatter
λ	Wavelength of light
σ_{abs}	Absorption cross section
σ_{scat}	Scattering cross section
σ_{ext}	Extinction cross section
σ_{geom}	Geometric cross section
Q_{scat}	Normalized scattering cross section
Q_{abs}	Normalized absorption cross section
η_{scat}	Scattering efficiency
$f_{forward}$	Forward scattering fraction
H_i	Magnetic field component in i direction
E_i	Electrical field component in i direction
k	Wave number
ω	Angular frequency

Chapter 1: Background and fundamentals of photovoltaic devices

Photovoltaic devices (PV) are devices that use the photovoltaic effect to transfer solar energy into electricity. With the development of modern technology, many countries and companies are putting great effort into research and commercialization of PV devices, which have both long-term environmental and economic benefits over traditional power sources. Numerous approaches are proposed and tested every year to improve the efficiency of PV devices, and various figures-of-merit and methodologies are needed to compare and contrast various technologies. In this chapter, we introduce photovoltaic devices and the basic modeling needed to define several key parameters that can be used to evaluate these approaches.

1.1 Introduction

Modern technology is driving the continued growth in demand for energy. The US Energy Information Administration (USEIA) predicted in their recently released International Energy Outlook 2016 that the world's energy consumption will increase by 48% between 2012 and 2040, from 549 quadrillion British thermal unit (Btu) to 815 quadrillion Btu [1]. At the same time, energy production and consumption have undergone significant changes. Although petroleum, natural gas and coal are still dominating the market, their market shares are expected to drop to 27% in 20 years, resulting in a market dominated by a combination of renewables, nuclear and hydroelectricity [2]. According to the prediction of the USEIA, the largest portion of renewable energy growth in the OECD (Organization for Economic Cooperation and Development) countries comes from wind and solar [1].

In spite of the tremendous progress in solar industry, there are still several difficulties that need to be overcome for photovoltaics to replace traditional methods of power generation. One of the main problems for the past several decades has been the cost per watt. In order to meet the great demand for energy, scientists need to find ways to build cheap, lightweight, flexible and efficient solar cells. To better evaluate and compare solar cells, we first introduce different theoretical models that have been developed and describe the key parameters of solar cells that determine their efficiency.

1.2 Diode equation and device model

A solar cell is a device that uses photovoltaic effect to generate electricity. When the light is absorbed by a solar cell, electron-hole pairs are generated. The electrons go through the external load and generate power. In 1945, Shockley proposed his well-known diode equation to describe the current-voltage characteristic of a p-n junction [3]:

$$I = I_R \left(e^{\frac{qV}{k_B T}} - 1 \right) \tag{1.1}$$

where V is the voltage across the p-n junction, I is the current through an external circuit, k_B is the Boltzmann constant, q is the electron charge, T is the temperature of the diode, and I_R is the reverse saturation current. A single p-n junction solar cell is nothing more than a diode that absorbs sunlight and transfers solar energy into electricity. Under illumination, the diode equation can be modified as:

$$I = I_L - I_R \left(e^{\frac{qV}{k_B T_c}} - 1 \right) \tag{1.2}$$

where I_L is the light generated current, T_c is the temperature of the cell. In this equation, the reverse saturation current I_R can be calculated by taking both radiative and non-radiative recombination of the junction into account [4]:

$$\begin{aligned} I_R &= qA_{cell} \left[\frac{n_i^2}{N_D} \frac{L_h}{\tau_h} \frac{s_h \cosh \frac{W_C}{L_h} + \frac{L_h}{\tau_h} \sinh \frac{W_C}{L_h}}{s_h \sinh \frac{W_C}{L_h} + \frac{L_h}{\tau_h} \cosh \frac{W_C}{L_h}} \right. \\ &\quad \left. + \frac{n_i^2}{N_A} \frac{L_e}{\tau_e} \frac{s_e \cosh \frac{W_A}{L_e} + \frac{L_e}{\tau_e} \sinh \frac{W_A}{L_e}}{s_e \sinh \frac{W_A}{L_e} + \frac{L_e}{\tau_e} \cosh \frac{W_A}{L_e}} \right] \end{aligned} \tag{1.3}$$

where W_A is the diode anode thickness, W_C is the diode cathode thickness, L_e is the electron diffusion length, L_h is the hole diffusion length, n_i is the intrinsic carrier concentration, N_A is the net acceptor concentration in the anode, N_D is the net donor concentration in the cathode, τ_e is the electron lifetime, τ_h is the hole lifetime, s_e is the electron surface recombination velocity, s_h is the hole surface recombination velocity, and A_{cell} is the area of the device. This model is also known as device model.

In most solar cells, the device model works fine. However, the effectiveness of the device model can be severely diminished in highly efficient solar cells such as gallium arsenide, because photons created by radiative recombination can be reabsorbed by the cell and create a new electron-hole pair. This re-absorption and re-generation process is called photon recycling.

1.3 Detailed balance theory and Shockley-Queisser limit

In order to better describe the characteristics of highly efficient solar cells, Shockley and Queisser developed a theoretical framework for determining the limiting efficiency of a single junction solar cell, which is known as Shockley-Queisser limit, based on the principle of detailed balance, which took photon recycling effects into account. This model is based on the following hypotheses [5, 6]:

- Radiative recombination is the only recombination mechanism that exists in the solar cell. Nonradiative recombination can be ignored.

- The photon-to-electron conversion efficiency is 100%.

- The carrier mobility is sufficiently large so that each generated electron-hole pair can be collected.
- Carrier population obeys Maxwell-Boltzmann statistics.
- Photon recycling effects exist in the cell.

The Shockley-Queisser limit is reached by applying the principle of detailed balance to the particle flux into and out of the semiconductor. The total current that flows through the external circuit of a plannar solar cell is:

$$I_{total} = q\left[N_{abs} - N_{emit}\left(V\right)\right] \tag{1.4}$$

where q is the charge of an electron, and N_{abs} and N_{emit} are the numbers of photons per unit time that are absorbed or emitted by the photovoltaic device, respectively. These rates can be calculated as [4]:

$$N\left(\theta_{max}, V, T\right) = A_{cell}\int_0^{\infty}\int_{\phi=0}^{2\pi}\int_{\theta=0}^{\theta_{max}} a\left(\theta,\phi,E\right)\times F\left(E,T,V\right)\cos\left(\theta\right)\sin\left(\theta\right)d\phi d\theta dE \tag{1.5}$$

where A_{cell} is the top illuminated surface area of the cell, $a(\theta, \phi, E)$ is the angle dependent probability of photon absorption/emission for incident/emitted photons of energy E, θ_{max} is the maximum angle for absorption (for N_{abs}) or emission (for N_{emit}), and $F(E, T, V)$ is the spectral photon flux that can be obtained from the generalized Planck blackbody law [7]:

$$F_s\left(E,T,V\right)=\frac{2n^2}{h^3c^2}\frac{E^2}{e^{\frac{E}{k_BT_s}}-1} \tag{1.6}$$

$$F_c\left(E,T,V\right)=\frac{2n^2}{h^3c^2}\frac{E^2}{e^{\frac{E-qV}{k_BT_c}}-1} \tag{1.7}$$

where T is the temperature of the sun or the cell, h is Planck constant, k_B is Boltzmann constant, c is the speed of light, n is the refractive index of the surroundings, which is usually taken to be vacuum ($n=1$), and qV characterizes the quasi-Fermi level splitting when describing emission from the cell. If the cell is under thermal equilibrium, we have:

$$I_{total}=q\left[N_{abs}-N_{emit}\left(0\right)\right]=0 \tag{1.8}$$

If the radiation on the solar cell only comes from the surroundings (dark condition), $F_s=F_c$, so the emissivity of the cell equals the absorptivity of the cell.

If $V<E_g-3kT$, $F_c\left(E,T,V\right)$ can be rewritten as:

$$F_c\left(E,T,V\right)=\frac{2n^2}{h^3c^2}\frac{E^2}{e^{\frac{E}{k_BT}}}e^{\frac{qV}{kT}}=F_c\left(E,T,0\right)e^{\frac{qV}{k_BT}} \tag{1.9}$$

so the solar cell's emission rate at voltage V can be rewritten as

$$N_{emit}\left(E,T,V\right)=N_{emit}\left(E,T,0\right)e^{\frac{qV}{k_BT}} \tag{1.10}$$

At open-circuit conditions, there is no current extracted, and the current balance equation becomes

$$0 = qN\left(\theta_s, T_s, V=0\right) + qN\left(\theta_c, T_c, V=0\right) - qN\left(\theta_c, T_c, V=0\right) e^{\frac{qV_{oc}}{k_B T_c}} \tag{1.11}$$

where the middle term corresponds to absorption due to emission from the ambient surroundings, also at $T = T_c = 300$ K; however, this term is much smaller than the flux from the sun. Thus, the light generated current is given by $I_L = qN(\theta_s, T_s, V = 0)$ and the dark current, in the radiative limit, is given by $I_D = I_R\left[\exp(\frac{qV}{k_B T_c}) - 1\right] = qN(\theta_c, T_c, V) - qN(\theta_c, T_c, V = 0)$, where $I_R = qN\left(\theta_c, T_c, V = 0\right)$ is the reverse saturation current. Solving Eq. [1.11] for the voltage yields the common expression for the open-circuit voltage [5, 8]:

$$V_{oc} = \frac{k_B T_c}{q} \ln\left(\frac{I_L}{I_R} + 1\right) \approx \frac{k_B T_c}{q} \ln\left(\frac{I_L}{I_R}\right) \tag{1.12}$$

The efficiency of solar cell is defined as $\eta = \frac{V_{oc} J_{sc} FF}{P_{in}}$ where FF is the fill factor which describes the ratio of the maximum power a solar cell can generate to the product of V_{oc} and I_{sc}, as is shown in Fig. 1.1.

1.4 Ideal bandgap for single junction solar cell

In the detailed balance model, the semiconductor bandgap determines both which photons can be absorbed, and at open circuit, which photons must be emitted. Absorption of above bandgap photons gives rise to a current, which can be withdrawn from the device. Under open-circuit conditions, the cell still absorbs light; however, no current is removed by the external circuit. In order to maintain a detailed balance, radiative recombination of excess carriers leads to a flux of pho-

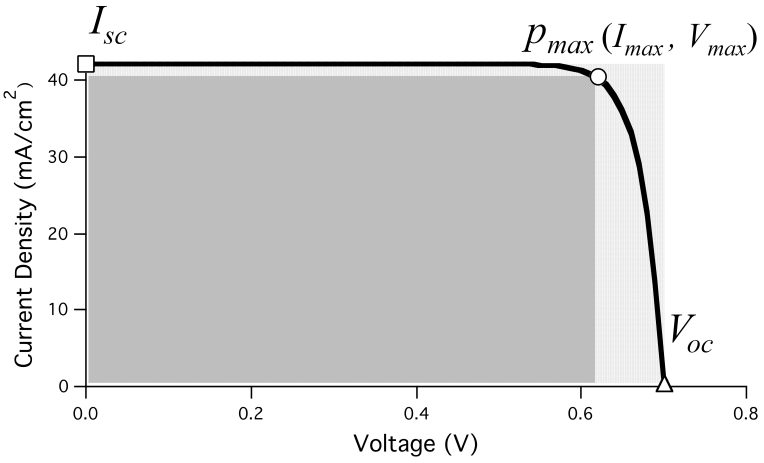

Figure 1.1: Current and voltage characteristics of a solar cell. The fill factor is defined as the ratio of the maximum generated power(dark grey area) to the product of V_{oc} and I_{sc} (light and dark grey areas).

tons out of the cell equal in number to those entering the cell. The emission rate is determined by the absorption rate and the bandgap. Thus, in the ideal case considered by Shockley and Queisser, the bandgap alone is all that is need to describe the absorption and emission processes. With this the conversion efficiency can be determined for an ideal device, as is shown in Fig. 1.2.

Based on the detailed balance model, the ideal bandgap for a single junction solar cell is around 1.26 eV. It can be seen from Fig. 1.2 that silicon ($E_g = 1.11$ eV) and GaAs ($E_g = 1.43$ eV) are on the left and right side of the peak respectively. This explains why silicon and GaAs are two popular materials in use. The modification of the absorption and emission of a cell can lead to spectral shifts and effective bandgap modifications of the device. This can be realized by putting a photonic

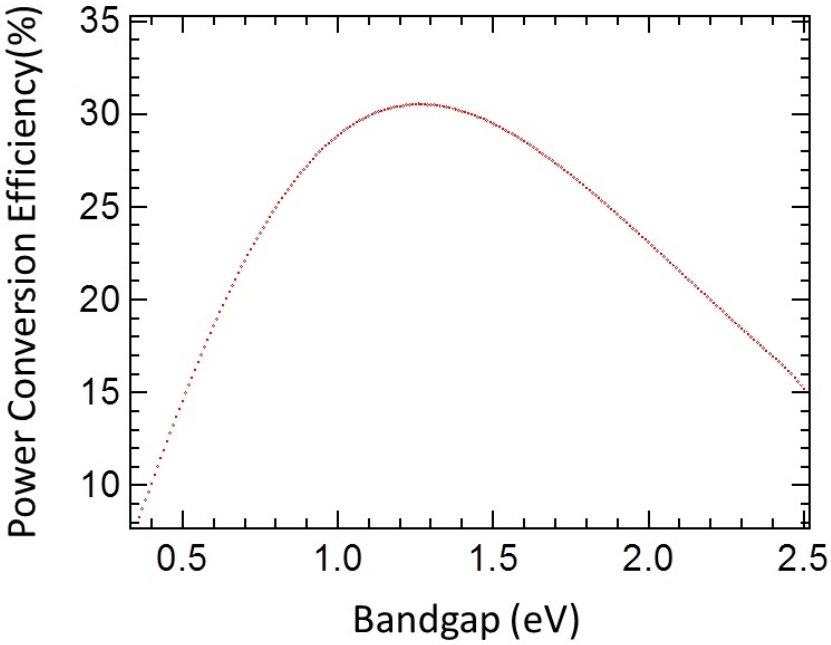

Figure 1.2: The power conversion efficiency of a single junction solar cell determined by the bandgap of the semiconductor based on the detailed balance model with a solar illumination modeled by the black body radiation at 6000 K. The red circles corresponds to the efficiency at the calculated bandgap. The power conversion efficiency first increases and then decreases with the increasing bandgap energy. The most ideal bandgap for a single junction solar cell is calculated to be around 1.26 eV.

crystal (PC) atop the cell. However, we found that the introduction of even small amounts of loss in a PC can result in significant efficiency degradations.

1.5 Double diode equation

The diode equation assumes that the solar cell can be treated as a single diode. However, a more realistic case considers the photo-current in a solar cell as being generated by multiple, parallel connected diodes in the junction area. These diodes

together determine the characteristics of the solar cell. The electrical characteristics of the solar cell can be equivalently transformed into the diagram shown in Fig. 1.2, where R_{SH} is the shunt resistance and R_S is the series resistance. All diodes are connected in parallel, and their effects are summed up as one single source with a light generated current of I_L.

The total number of parallel connection can be simplified to two to describe the characterization of a solar cell at both low and high voltage regions. The overall current is the summation of the two diodes, resulting in light condition behavior given by [9–12]:

$$I = I_L - I_1 \left[\exp \frac{q\left(V + IR_s\right)}{kT_c} - 1\right] - I_2 \left[\exp \frac{q\left(V + IR_s\right)}{nkT_c} - 1\right] - \frac{V + IR_s}{R_{shunt}} \quad (1.13)$$

where I_L is the light generated current, I_1 is the dark current coefficient in high voltage region, I_2 is the dark current coefficient in low voltage region, R_s is the series resistance, R_{shunt} is the shunt resistance, and n is the ideality factor of the diode in low voltage region. Similarly, in dark condition [9–12]:

$$I = I_1 \left[\exp \frac{q\left(V - IR_s\right)}{kT_c} - 1\right] + I_2 \left[\exp \frac{q\left(V - IR_s\right)}{nkT_c} - 1\right] + \frac{V - IR_s}{R_{shunt}} \quad (1.14)$$

1.6 Outline of thesis

This thesis focuses on design, modeling, measurement, and applications of photonic technologies in solar cells. An overview of the following chapters is given here:

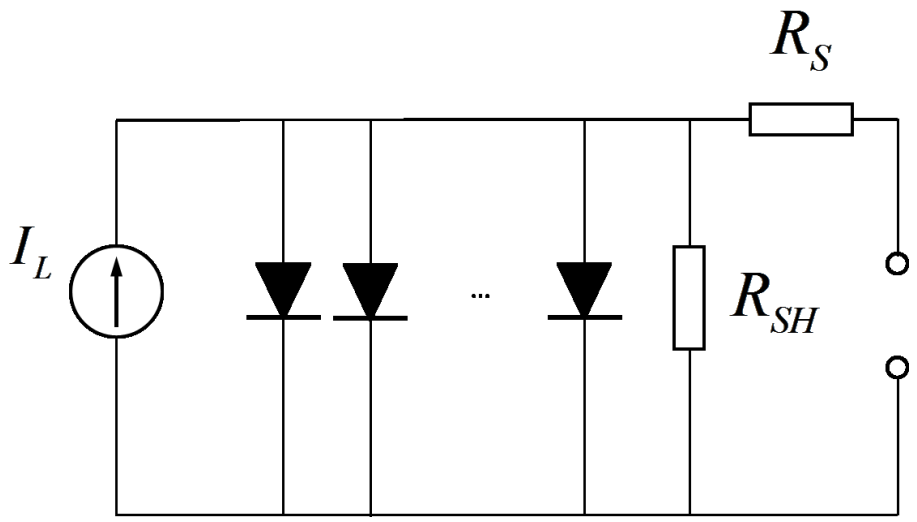

Figure 1.3: The circuit diagram of a multiple diode model for a solar cell including parasitic series and shunt resistances.

- Chapter 2 introduces plasmonic and photonic effects used in photovoltaic devices and their influence on photon absorption within the semiconductor. This chapter gives an overview of the traditional light trapping methods, design principles and limitations. This chapter is based in part on Xu, Y., Murray, J. & Munday, J. N. Quantum Dot Solar Cells 349–382 (Springer New York, 2014).

- Chapter 3 explores the possibility of using quantum dots for a new scattering mechanism in solar cells. We demonstrated the effectiveness of adding a layer of quantum dots to increase the absorption within a solar cell. This chapter is based on Xu, Y. & Munday, J. N. "Light trapping in a polymer solar cell by tailored quantum dot emission" Opt. Express 22(S2),A256-A267(2014).

- Chapter 4 generalizes the detailed balance equation in nanostructured solar

cells and explores the upper bound of their power conversion efficiency. This chapter is based on Xu, Y., Gong, T. & Munday, J. N. "The Shockley-Queisser Limit for Nanostructured Solar Cells" Scientific Reports 5, 13536 (2015).

- Chapter 5 discusses the possibility of adding photonic bandgap structures to modify the emission and effective bandgap of semiconductors and how solar cells can benefit from it. This chapter is based on Xu, Y. & Munday, J. N.,"Designing Photonic Materials for Effective Bandgap Modification and Optical Concentration in Photovoltaics" IEEE J.PV. 4(1), 233-236(2014).

- Chapter 6 focuses on our experiments in effective bandgap modification. In this chapter, we show how the bandgap of a GaAs solar cell is modified by adding photonic bandgap structures atop it and its benefits. This chapter is based on a manuscript in preparation.

- Chapter 7 expands the discussion of photonic bandgap structures to photonic crystals and explores the influence of the Purcell factor in photonic crystal solar cells. This chapter is based on Xu,Y. Waks, E. & Munday, J.N., "Improved voltage response in III-V solar cells based on engineered spontaneous emission" Photovoltaic Specialist Conference (PVSC), 2015 IEEE 42nd, 1-4

- Chapter 8 concludes the current work and offers potential extensions in the future.

Chapter 2: Plasmonics and photonics in photovoltaic devices

Nearly all photovoltaic devices require a compromise between light absorption and carrier collection. For planar structures, a thick film is sought for light absorption, while a thin film is sought for efficient carrier extraction. In this chapter, we circumvent these contrary requirements through the use of photonic and plasmonic structures. These structures allow for strong concentration of light into small volumes-simultaneously attaining large absorption enhancement and efficient carrier collection. The improved optical response is obtained by (1) increasing the optical path length and reducing the reflection through particle scattering, (2) enhancing the local field strength through the excitation of localized resonances, or (3) waveguiding. While these concepts are important to all light collection devices, they are of particular interest to quantum dot solar cells, where the need for thin structures that can absorb nearly all of the incident light is a critical design criterion.

2.1 Introduction

While traditional photovoltaics have relied on relatively thick semiconductor layers to ensure maximum light absorption from the sun, the latest devices rely on thin film structures either out of necessity (due to small carrier diffusion lengths) or for market specific applications (e.g. cost reduction, flexibility, weight, etc). However, a reduction of the semiconductor's thickness also reduces the amount of incident light that can be absorbed. This leads to a trade-off between absorption, carrier collection, flexibility, etc.

For planar photovoltaic devices, light absorption is exponential. The intensity of the incident illumination decreases from the front surface of the device as:

$$I = I_0 e^{-\alpha L} \tag{2.1}$$

whereI_0 is the incident intensity that enters the material, L is optical path length (i.e. the depth) within the planar structure, and α is the absorption coefficient which is related to the wavelength λ and imaginary refractive index of the material κ by:

$$\alpha = \frac{4\pi\kappa}{\lambda} \tag{2.2}$$

Similarly, the fraction of the incident power (P_0) that is absorbed (P_{abs}) is given by $a(\alpha, L) = P_{abs}/P_0 = (1 - e^{-\alpha L})$. κ, and hence α, generally tends toward zero at the semiconductor bandgap, where the material becomes transparent. Thus,

the short wavelengths are more easily absorbed near the front surface, while longer wavelengths (near the band-edge) are absorbed deeper within the cell. Fig. 2.1 shows the power absorbed per unit area for a single optical pass through a silicon slab with thicknesses of 1 μm, 10 μm, and 100 μm. While the 100 μm slab absorbs 85% of the above bandgap energy photons, the 1 μm slab only absorbs 36%, making additional light trapping structures necessary to improve the absorption.

For high collection efficiency, the cell generally needs to be significantly thinner than the minority carrier diffusion length, L_D. This condition can be easily met in thin film devices; however, for thick devices, bulk recombination results in reduced carrier collection. Fig. 2.2 shows the combined effects of light absorption and carrier collection. For thin devices, nearly all generated carriers are collected; however, a significant fraction of the long wavelength incident solar radiation is not absorbed. Conversely, for thick devices, nearly all of the incident light is absorbed; however, carrier collection is impeded by the large distance the minority carriers must travel without recombining with bulk trap states to be collected at the leads. For a given material, this trade-off leads to an optimum thickness for maximum efficiency.

For GaAs, this trade-off results in a device thickness of $\sim$ 3 μm (see Fig. 2.3). If a reflective back surface (e.g. a mirror) is added, the device can be half as thick and still absorb the same amount of light. By reducing the thickness, carrier collection is improved without suppressing the absorption, which leads to a thinner device that is more efficient.

From a design point-of-view, we can first pick a semiconductor thickness that allows for easy carrier collection, and then determine the appropriate optical design

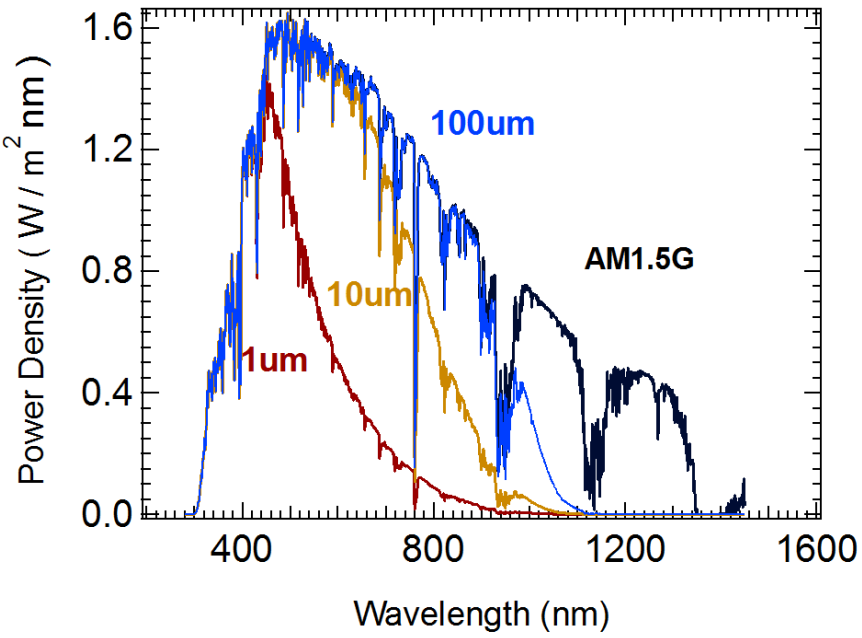

Figure 2.1: Solar spectrum (AM 1.5G) and representative absorption for thick and thin Si devices. Short wavelength light is absorbed in all structures; however, thin slabs are ineffective at absorbing long wavelength photons.

to allow for sufficient light absorption. Traditional light management is achieved through anti-reflection coatings and micro-scale texturing (Fig. 2.4). For planar structures, anti-reflection coatings are generally constructed by adding one or two additional (non-absorbing) layers to the top of the device to help couple the incident plane waves into the semiconductor. The thickness and index of refraction of the layers are chosen so that there is destructive interference for the reflected wave. To minimize the reflection, two conditions must be met. First the phase of the reflected light from the surfaces should differ by 180°. For normal incidence light, this occurs when the thickness of the film is equal to a quarter wavelength of the incident light:

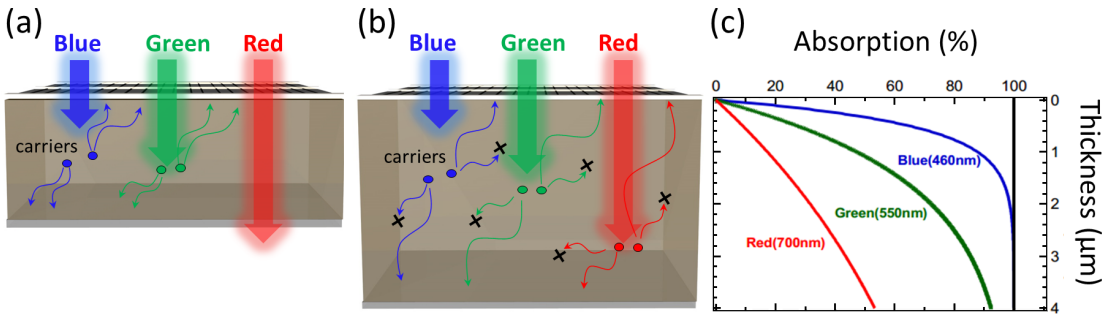

Figure 2.2: Schematic of absorption depth and carrier collection for different wavelengths of incident light and film thicknesses. (a) A thin slab efficiently collects generated carriers; however, long wavelength photons are not absorbed resulting in reduced current. (b) A thick device absorbs nearly all of the light; however, the long path for collection increases the likelihood of carrier recombination without collection. (c) Absorption profile for different wavelengths of light.

$L = \lambda/(4n_1)$, where n_1 is the refractive index of the film. The second condition is that the amplitudes of the reflected waves are equal. This conditions specifies that the index of refraction for the ARC should be: $n_1 = \sqrt{n_0 n_2}$, where n_0 and n_2 are the refractive indices of free space ($n_0 = 1$) and the substrate respectively. The general expression for the reflectivity using a single layer ARC is [13]:

$$R = \frac{(n_0 - n_2)^2 + (n_0 n_2/n_1 - n_1)^2 \tan^2\phi}{(n_0 + n_2)^2 + (n_0 n_2/n_1 + n_1)^2 \tan^2\phi} \tag{2.3}$$

where $\phi = 2\pi n_1 L cos\theta_i/\lambda$ is the phase shift of the light incident with an angle θ_i from the normal and has a free space wavelength of λ. Because the reflectivity is wavelength dependent, a compromise must be reached that allows for the maximum amount of light to enter the cell over a broad range of wavelengths (see Fig. 2.5). Multi-layer ARCs can also be used to allow for reduced reflection over a larger

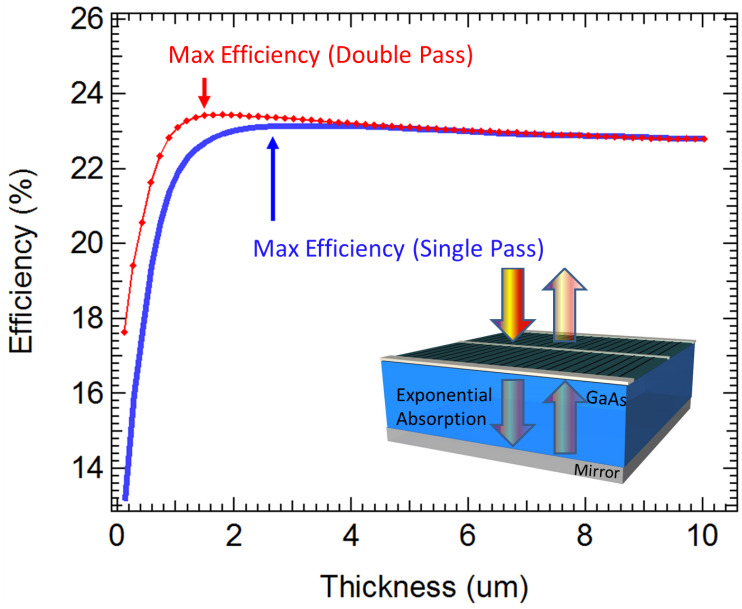

Figure 2.3: Maximum efficiency is a trade-off between high absorption efficiency (thick device) and high carrier collection efficiency (thin device). The use of a mirror back reflector allows a device to be half as thick and still absorb the same amount of light.

bandwidth.

In order to achieve broadband anti-reflection properties, the index of refraction of the ARC film can be continuously varied so that there is never an abrupt change in the refractive index, as shown by Lord Rayleigh mathematically in the 1880s [14]. These structures, referred to as graded-index coatings, have been demonstrated experimentally by partial filling the ARC layer with air [15,16], using oblique-angle deposition of thin films [17], or using nanostructured cones or pyramids that mimic the functionality of moth eyes [18]. In addition interference-based thin film ARCs, which are used for nearly all commercial solar cells, pyramidal structuring is also common

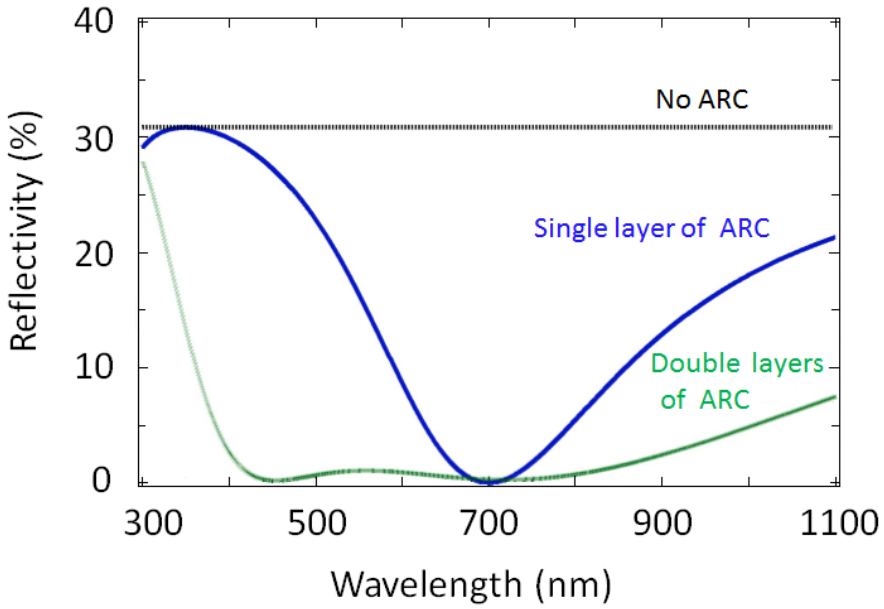

Figure 2.4: Reflectivity from a surface with $n_2 = 3.5$ using no ARC, a single-layer ARC, and a double layer ARC optimized for $\lambda = 700$ nm.

in silicon (Fig. 2.5). Such structures can be easily created through anisotropic etching of crystalline Si. Texturing typically results in pyramidal structures ($\sim$ 10s μm), which allow incident light multiple entrance attempts at the surface as well as increased path lengths (Fig. 2.6).

As solar cell device thicknesses become comparable to the wavelength of the incident light, new optical structures and scattering processes must be designed to function on the subwavelength scale. The ability of a particle to scatter incident light is strongly dependent upon the index of refraction contrast between the particle and its surrounding, as discussed in section 2.2. For this reason metals often make excellent scattering objects, so long as the ohmic loss within the metal is minimized. There are three main mechanisms for increasing light absorption within a

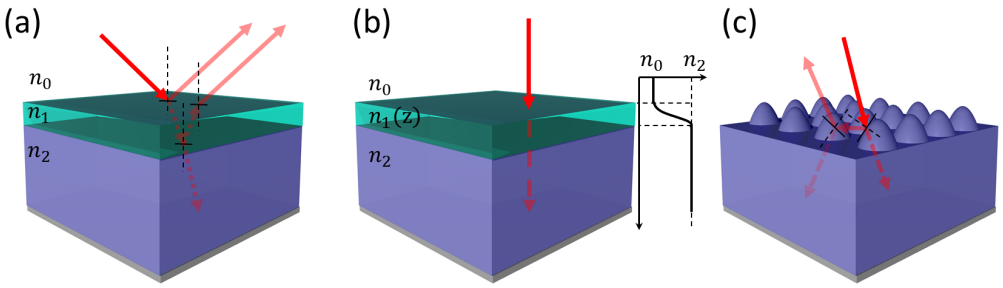

Figure 2.5: Typical anti-reflection techniques for macroscopic solar cells: (a) destructive interference of reflected plane waves, (b) graded index structures, (c) pyramidal surface texturing.

semiconductor device using metal nanoparticles (see Fig. 2.6). First, the nanoparticles can be used to increase forward scattering and hence reduce reflection (Fig. 2.6(a)). Second, metal particles or gratings can be used to concentrate the incident light into a small volume, acting as a subwavelength antenna (Fig. 2.6(b)). Third, the metal nanostructures can be used to couple the incident free-space light into waveguide modes of the structure, which in-turn dramatically increases the optical path length (Fig. 2.6(c)).

Metallic structures are particularly useful for concentrating and trapping light because of the excitation of surface plasmons [19], i.e. charge density excitations that result from a coupling of the incident electromagnetic radiation and the surface charge density of the metal (Fig. 2.7). For nano-structures, this coupling can result in localized excitions with field enhancements of many orders of magnitude. When light is incident on a planar structure, the excitation can result in a surface plasmon polariton, which may be capable of traveling several microns along the surface of

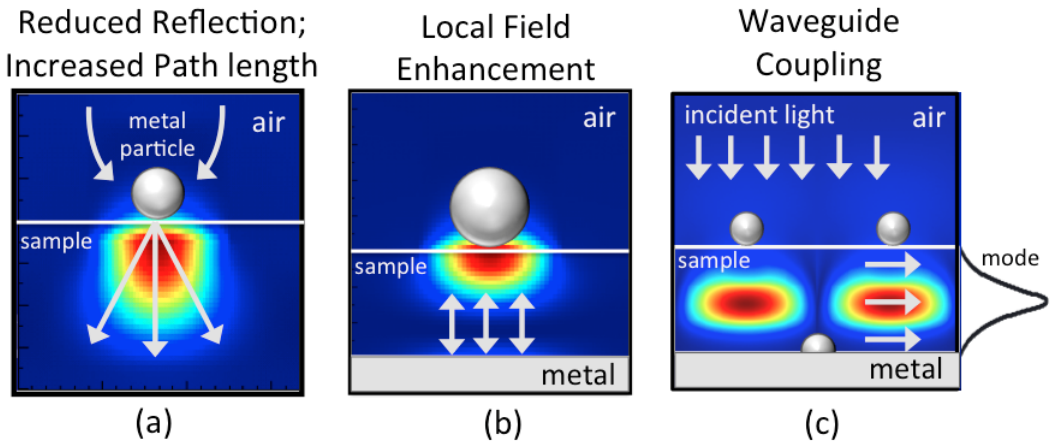

Figure 2.6: Plasmonic nanoparticles can improve photovoltaics by (a) reducing reflection and increasing path length, (b) creating high local fields, or (c) coupling incident light into waveguide modes of the structure.

the metal. Both localized and propagating modes can be tailored to meet the specific frequency range specification required for a particular photovoltaic application through tuning either the geometry of the structure or the materials involved (choice of metal and surrounding dielectrics). This tunability will be explored in further detail in the following sections.

During the past several years, there has been a great deal of research into the use of surface plasmons for increasing the light absorption in thin film photovoltaic devices [20–22]. Early studies were conducted by Stuart and Hall in the mid-1990s and showed nearly a 20x enhancement of the photocurrent for long wavelength incident light in a Si photodetector due to metallic nanoparticles that were formed on top of the device [23]. Since these first studies, improved current generation has been found for a variety of scattering structures placed on top of, within, or

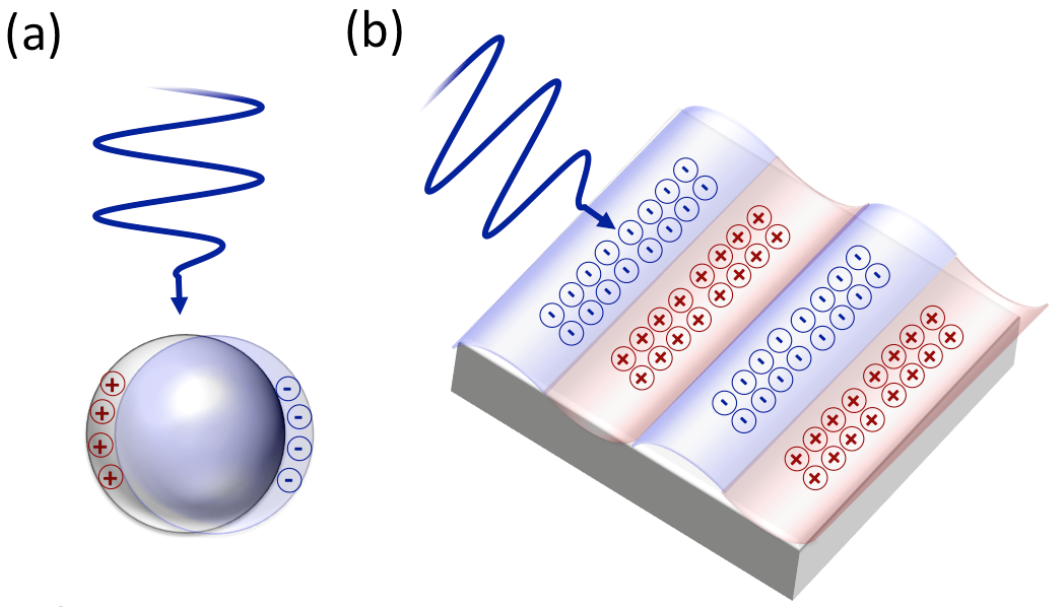

Figure 2.7: Excitation of surface plasmons. (a) The incident light is coupled to the free electrons in a metal nanoparticle resulting in excitation of a localized surface plasmon resonance. (b) When light is incident on a planar structure, the coupling results in a propagating surface wave called a surface plasmon polariton.

on the bottom of photovoltaic devices. In addition to Si solar cells, enhancements have been achieved for a variety of structures and materials including quantum dot/well structures, GaAs solar cells, polymer solar cells, and dye-sensitized solar cells. Quantum dot solar cells are particularly well suited for plasmonic enhancement due to the thinness of most devices. Excitation of a surface plasmon results in high field intensities near the metal interface, which decay with distance from the metal surface. With appropriate incoupling to a surface plasmon mode, even a monolayer of quantum dots can lead to nearly complete optical absorption. Further, the plasmon resonance can be tuned through geometry and material choice in order

to overlap with the absorption spectrum of the quantum dots. In the next section we will discuss the different types of optical modes, the scattering properties, and the ways to tune the resonance.

In order to increase light absorption within the semiconductor, we must increase the amount of time that the light spends within the layer. The increased time that the light spends within the semiconductor improves the likelihood of photon absorption and ultimately leads to increased carrier collection and photocurrent. When light is scattered into a waveguide mode of the structure, the optical path length is effectively increased, because the vertical propagation has been converted into horizontal propagation, and the optical path can be many times longer than the thickness of the semiconductor layer. Depending on the boundary conditions at the interfaces, either photonic or plasmonic modes can be excited. Photonic modes are the result of light guiding based on a contrast in the index of refraction as used in fiber optic waveguides and can exist as either TE or TM modes (as described below). Surface plasmon polariton (SPP) modes are electromagnetic surface waves coupled to oscillations of conduction electrons at the interface of a metal and a dielectric and generally only exist as TM modes in planer structures. In addition to the SPP modes, non-propagating surface plasmons (SP) can be excited in metallic nanostructures, such as nanoparticles or grooves, and lead to various resonance and scattering effects. The next two sections will discuss light scattering by particles and waveguide modes of planar structures.

2.2 Scattering

Subwavelength particles can help a photovoltaic device absorb more of the incident spectrum by increasing the amount of light that is incoupled into the device and also by increasing the optical path length of light that enters the cell. For a bulk material, the Beer-Lambert law describes the exponential absorption of photons within the slab. As discussed above, the intensity decays as $I = I_0 e^{-\alpha L}$. Once a material has been chosen for the photovoltaic device, α is fixed. Thus, to increase the absorption within the solar cell, we need to increase the optical path length. As we shall see in this sub-section, nanoparticles can make for excellent scatterers, which can increase the optical path length and lead to enhanced absorption within the solar cell.

Optical scattering is the process by which normally incident light acquires components perpendicular to its original path. When light is transmitted through an optically inhomogeneous material, energy is dispersed throughout the complete solid angle of 4π and leads to the existence of energy in a direction perpendicular to the original propagation. As light encounters a small particle, the atomic orbitals of the molecules in the scattering particle tend to oscillate at the frequency of the incident light-inducing a dipole moment. This dipole moment serves as a secondary source and radiates in all directions. This re-radiated light can either be in phase with the incident beam or out of phase depending on the frequency of the incident light and the resonant frequency of the scatterer.

When a scattering particle is placed on top of a solar cell, the normally incident

light is scattered at an angle θ. The path length is increased from L to $L/\cos\theta$, causing the intensity to decrease more rapidly due to increased absorption at a given depth. In this way, scattering particles can increase the optical path length and improve absorption within the solar cell.

Scattering models can be classified into two categories: linear (e.g. Rayleigh) and nonlinear (e.g. Raman). In this chapter we only consider linear scattering processes because, in the absence of a strong optical pumping source (e.g. a laser or very intense concentration), nonlinear effects will be very weak. Light scattering is fully described by Maxwell's equations; however, there are two regimes where approximate solutions can be obtained and are quite useful: Rayleigh scattering (elastic scattering by particles much smaller than the wavelength of the light) and Mie scattering (solutions represented in the form of an infinite series, which can describe scattering when the wavelength of light is comparable to the size of the particle). In order to consider when these approximate solutions can be used, we introduce a size parameter:

$$\alpha_x = \frac{\pi D_p}{\lambda} \tag{2.4}$$

where D_p is the diameter of the scatterer. This parameter describes the relationship between the size of the scatterer and the wavelength of the incident light.

If $\alpha_x < 0.1$, scattering can be described in the domain of Rayleigh scattering. Larger α_x lead to larger scattering intensities.

If $0.1 < \alpha_x < 10$, the dependence of scattering intensity on incident wavelength

weakens with increasing of α_x; however, maxima and minima occur in the scattering intensity resulting of excitations of resonances within the particle.

If $\alpha_x > 10$, scattering intensity becomes less dependent on the incident wavelength. Eventually the realm of geometric optics is valid.

Although we introduced Rayleigh and Mie scattering above, it doesn't necessarily mean that the scattering can be easily labeled as either Rayleigh or Mie. Both of these are approximate solutions that are sometimes convenient for obtaining analytical solutions; however, in some situations it is necessary to solve Maxwell's equations numerically to determine the appropriate scattering properties. In the following subsections, we solve Maxwell's equations numerically using the method of Finite Difference Time Domain (FDTD). For further details on analytical models for light scattering from particles, see Ref [24].

2.3 Figures of merit

In order to quantify a particle's ability to scatter light, several figures of merit need to be defined. In the following sub-sections, we describe the various scattering cross sections, scattering efficiencies, and scattering fractions necessary to describe light scatting by particles.

In the realm of geometric optics, we can define a scattering cross section in terms of the geometric size of the particle; however, for subwavelength particles the scattering cross section can often be much larger than the particle's geometric size due to the wave nature of light. The extinction cross section of a particle is the sum of

two hypothetical areas: the effective area over which the particle acts like a scatterer and the effective area over which it acts like an absorber. Because the absorption and scattering properties depend on the wavelength dependent permittivity, the cross sections are similarly a function wavelength. The extinction cross section is thus defined as:

$$\sigma_{ext}(\lambda) = \sigma_{scat}(\lambda) + \sigma_{abs}(\lambda) \tag{2.5}$$

where $\sigma_{scat}(\lambda) = P_{scat}(\lambda)/I_{source}(\lambda)$ is the scattering cross section and $\sigma_{abs}(\lambda) = P_{abs}(\lambda)/I_{source}(\lambda)$ is the absorption cross section. $P_{scat}(\lambda)$ is the power scattered, $P_{abs}(\lambda)$ is the power absorbed, and $I_{source}(\lambda)$ is the intensity of the incident source. Typically, these cross sections are normalized to the geometric cross section of the particle, σ_{geom}, to obtain the normalized scattering cross sections:

$$Q_{scat}(\lambda) = \frac{P_{scat}(\lambda)/I_{source}(\lambda)}{\sigma_{geom}} \tag{2.6}$$

$$Q_{abs}(\lambda) = \frac{P_{abs}(\lambda)/I_{source}(\lambda)}{\sigma_{geom}} \tag{2.7}$$

If the particle is used to efficiently scatter light into a solar cell, we want a large scattering cross section and a small absorption cross section, because the absorbed energy in the scatterer is converted into heat instead of exciting electron hole pairs in the surrounding semiconductor and thus leads to the loss of energy. An important figure of merit to describe the fraction of light scattered to the total extinction is the scattering efficiency, which is given by the ratio of the scattering cross section to the extinction cross section:

$$\eta_{scat} = \frac{\sigma_{scat}}{\sigma_{ext}} = \frac{\sigma_{scat}}{\sigma_{scat} + \sigma_{abs}} \tag{2.8}$$

Thus, a higher scattering efficiency tends to better performance by more efficiently scattering the light. In some cases, the cross sections have can be described analytically. One example is a plane wave incident on a sphere. For simplicity, we treat the problem in the quasistatic limit, assuming that the sphere is much smaller than the wavelength of incident light so that the field on the particle is uniform. The scattering and absorption cross sections are:

$$\sigma_{scat} = \frac{1}{6\pi}\left(\frac{2\pi}{\lambda}\right)^4 |\alpha_{sp}|^2 \tag{2.9}$$

$$\sigma_{abs} = \frac{2\pi}{\lambda} Im\left[\alpha_{sp}\right] \tag{2.10}$$

where α_{sp} is the polarizability of the sphere:

$$\alpha_{sp} = 4\pi r^3 \frac{\varepsilon_m - \varepsilon_s}{\varepsilon_m + 2\varepsilon_s} \tag{2.11}$$

and ε_s and ε_m are the permittivities of the surround material and of the material making up the sphere, respectively.

While having a large scattering cross section ensure that a large fraction of the light is scattered, only light that is scattered in the forward direction will be useful if the particles are placed on top of the solar cell (likewise, backward scattering is important for photovoltaic applications where the particles are placed on the backside of the device). In order to evaluate the portion of the total scattered energy that goes forward into the cell, we introduce another important figure of

merit: the forward scattering fraction $f_{forward}(\lambda)$. This parameter is calculated by dividing the forward scattered power $P_{forward-scattered}(\lambda)$ by total scattered power $P_{scattered}(\lambda)$:

$$f_{forward}(\lambda) = \frac{P_{forward-scattered}(\lambda)}{P_{scattered}} \tag{2.12}$$

For a very small spherical particle, the scattering behavior is similar to that of a dipole emitter. In fact, because the scattering phenomenon is the result of re-emission of atomic dipole moments, the forward scattering fraction is nearly the same for these two cases. Figure 2.8 shows the forward scattering fraction for both a 50 nm particle sitting on the surface of the substrate ($n = 1.4$) and for a dipole source 50 nm above the substrate. Both structures result in approximately 60-70% of the incident light scattering in the forward direction, indicating that a dipole source can be used to roughly estimate the forward scattering properties of the particle.

2.4 Scattering parameters

A particle's scattering properties depend upon its composition, shape, size, surroundings, and its distance from the surface. In this subsection, we explore how these variables affect the particle's scattering properties.

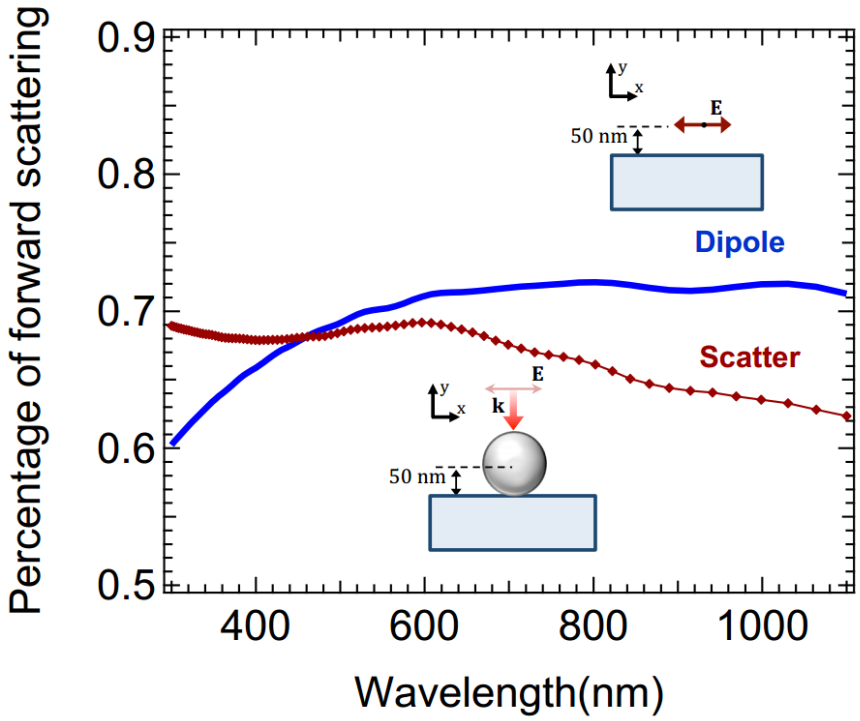

Figure 2.8: The percentage of forward scattering in the two cases. The diagram showed two cases. Case I, plane wave incident on a spherical silver scatterer with a radius of 50 nm sitting on an n = 1.4 substrate. Case II, dipole source above the substrate.

2.4.1 Particle material

Scattering particles can be made from metals, dielectrics, or semiconductors. A large index contrast between the particle and the surround environment can increase optical scattering and suggests that materials whose indices vary significantly from 1 are of interest. In particular, many semiconductors have indices of refraction between 3 and 4 in the visible and thus can be used effectively as Mie scatterers [24, 25]. Metals, on the other hand, have a permittivity that can be negative. For a spherical metal particle with permittivity ε_m embedded in a medium with ε_s, a

dipolar surface plasmon resonance can be excited when $\varepsilon_m = -2\varepsilon_s$. This corresponds to a maximum in the polarizability (Eq. 2.11) and hence scattering cross section. Given this unique situation achievable with metals, it is worthwhile to discuss a few typical metals such as silver, gold, copper, and aluminum in more detail.

Using the Drude model, the dielectric permittivity can be expressed as:

$$\varepsilon = 1 - \frac{\omega_p^2}{\omega^2 + i\omega\Gamma_p} \tag{2.13}$$

where ω_p is the plasmon frequency of the material and Γ_p is the damping rate. Because ω_p is unique to the type of metal, different metals have different optical responses, thus leading to the possibility of having different peaks in its scattering cross section spectrum. When choosing which material to use as the scatterer, it is desirable to choose a material whose scattering peak has sufficient overlap with the solar cell's absorption spectrum. In that case, the particle can efficiently scatter as much power as possible. We put metallic spheres with radii of 50 nm in the vacuum and change the materials among silver, aluminum, gold and copper to check the scattering and absorption cross section to get Fig. 2.9.

Plots in Fig. 2.9 clearly demonstrate that in vacuum environment and for a sphere with a radius of 50 nanometers, the scattering efficiency of silver and aluminum is much higher than that of the copper and gold. That is to say in this case, silver and aluminum have higher potential to be good scattering material.

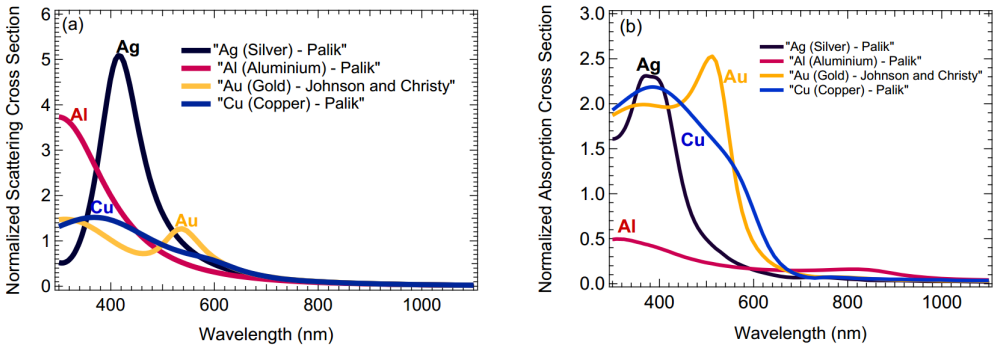

Figure 2.9: (a) The spectrum of normalized scattering cross section of particles made from silver, aluminum, gold and copper. (b) The spectrum of normalized absorption cross section of particles made from silver, aluminum, gold and copper. Particles are in a vacuum environment (n = 1) and have a spherical shape with a diameter of 100 nm.

2.4.2 Surrounding material

In the preceding subsection, the scattering particles where consider to be in free space (n = 1). However, these particles are usually embedded within another material of index n_s or are put on top of a substrate, e.g. on top of a solar cell. We can expect that the scattering performance of the particles will be influenced by that layer due to the fact that the effective permittivity of the optical space would change. The surroundings in turn can modify the plasmon resonance peak and hence scattering cross sections. To understand how the surroundings will influence the scattering, we consider a spherical silver particle surrounded by dielectric materials with different refractive indices.

Fig. 2.10 shows that there is a red shift of the surface plasmon resonance when the refractive index of the surrounding material increases. Also, the peak of

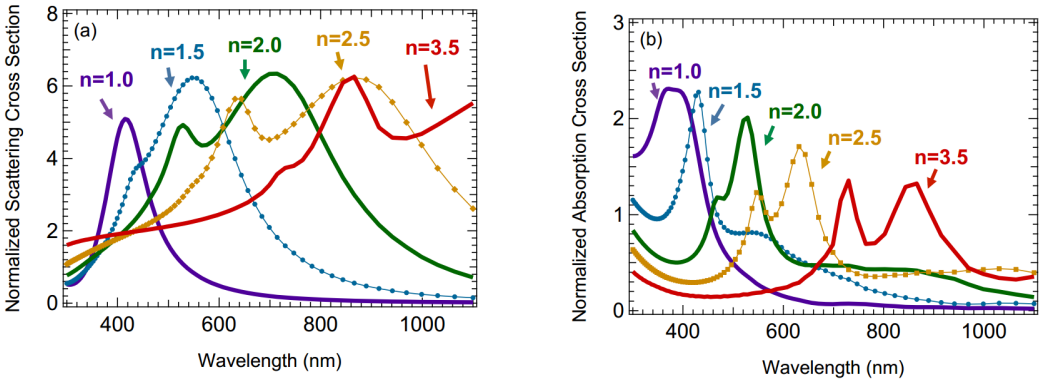

Figure 2.10: (a) normalized scattering cross section changes with refractive index: n = 1 (e.g. air), n = 1.5 (e.g. SiO_2), n = 2 (e.g. Si_3N_4), n = 2.5 (e.g. TiO_2) and n = 3.5 (e.g. GaAs) (b) normalized absorption cross section changes with refractive index.

the scattering cross section first increases dramatically, in the range of 1.5 to 2. On the other hand, the absorption cross section decreases with the increasing refractive index of the surroundings. Multiple peaks are evident in the cases within a larger index of refraction due to excitation of higher order resonances (e.g. quadruple moments).

Then we consider the real case, to put a scatterer on the top of a solar cell. The interesting thing here is that we can make a rough assumption for the scattering and absorption cross sections if we know the ones in the cases where the scatterer is inside certain materials. Why do we want to make such a kind of assumption? The reason is that it is always easier to deal with the calculations in a homogeneous environment.

In the following part, we are going to show the way to make that assumption. We put a gold sphere (r = 25 nm) half inside an n = 2 substrate. Assuming

that the substrate is semi-infinite and half of the sphere is in the air, it is obvious that permittivity of the whole space should be 1.5 on average. Will there be any similarities if we put the sphere inside an n = 1.5 material? The answer is yes. As is shown in Fig. 2.11, the differences in the cross sections between the two cases are fairly small.

2.4.3 Particle shape

The particle shape also plays a crucial role in determining the scattering property. For simplicity, we consider a few typical examples (sphere, cylinder, and cube). All shapes are made from silver and sit directly on the top of an infinite substrate with n = 2. As can be seen from the Fig. 2.12, the cube and the cylinder have very similar forward scattering fractions, $f_{forward}(\lambda)$. However, $f_{forward}(\lambda)$ for sphere is quite different. The reason for this effect is that the cube and cylinder have almost the same fraction of their volumes close to the substrate, while the volume of the sphere is centered farther away from the substrate.

2.4.4 Particle size

The size of the particles is important in determining scattering cross section (see for example that the radius enters into the polarizabilty for spherical particles in Eq 2.11). When the particle is fairly small, σ_{scat} is much smaller than σ_{abs}, which indicates that $\sigma_{scat} + \sigma_{abs} \approx \sigma_{abs}$ and absorption plays the dominant role. However, with the increasing size, σ_{scat} will increase much faster thanσ_{abs} and eventually

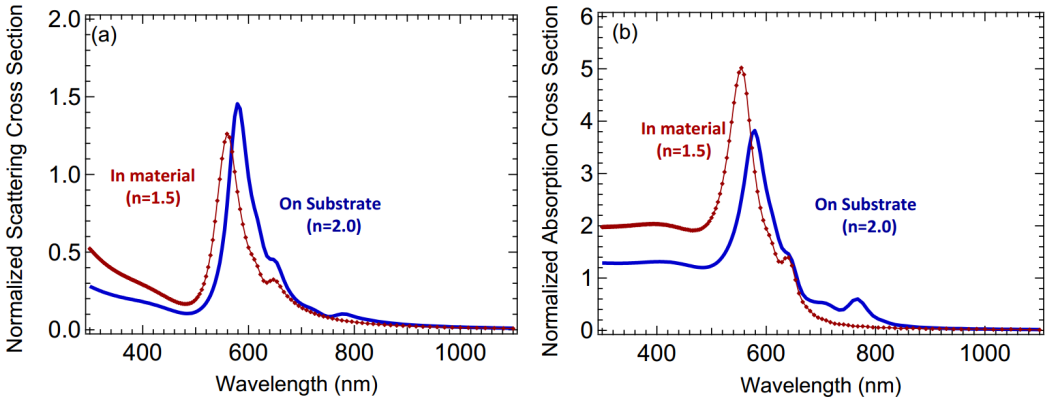

Figure 2.11: (a) Normalized scattering cross section (b) Normalized absorption cross section. Two cases are compared. Case I: a gold sphere is put on a substrate with a refractive index of 2 (red lines). Case II: a gold sphere is surrounded by a material with a refractive index of 1.5 (blue lines). The radiuses of the spheres are 25 nm in both cases.

dominates. As the size of the particle approaches the wavelength of light ($\alpha \sim 1$), the quasistatic limit will be broken and multipolar modes may become important.

Although the various cross sections increase with radius, the normalized cross section will vary depending on the geometrical cross section. Fig. 2.13 shows that the normalized scattering cross section increases with radius, while the normalized absorption cross section decreases with radius. That is to say, larger scatterers have higher scattering efficiency because scattering plays a dominant role in deciding the extinction cross section. A sphere with a 50 nm radius has a scattering efficiency of 60 - 80%, while a sphere with a radius of 30 nm only has a scattering efficiency $\sim$ 30% (Fig. 2.13(b)).

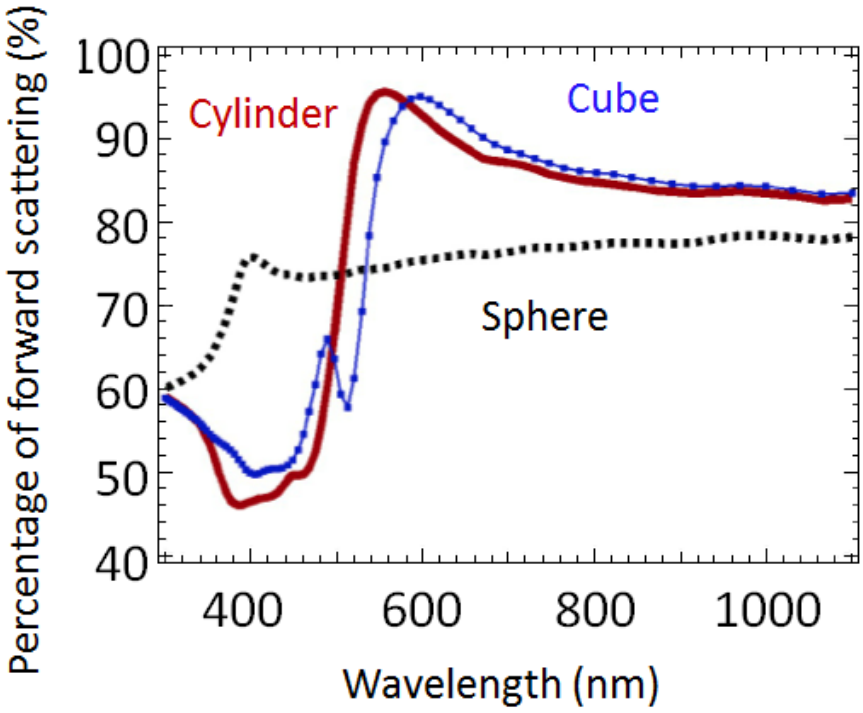

Figure 2.12: Spectrum of percentage of forward scattering corresponding to different particle shapes. There are three shapes of the silver particle: sphere (d = 100 nm: blue line), cylinder (r = 50 nm, h = 100 nm: red line) and cube (d = 100 nm: green line). All of them are put on an n = 2 dielectric substrate.

2.4.5 Distance from surface

Previously we considered an isolated particle in free space, completely within a material, and half embedded within the material. As a particle approaches a surface, it scattering properties will change as it begins to be influenced by the refractive index of the substrate. Fig. 2.14 shows the shift in frequency and magnitude of the normalized scattering cross section of a 50 nm Ag nanoparticle as it approaches the surface of a semi-infinite substrate of index n = 2. The nanoparticle begins at a

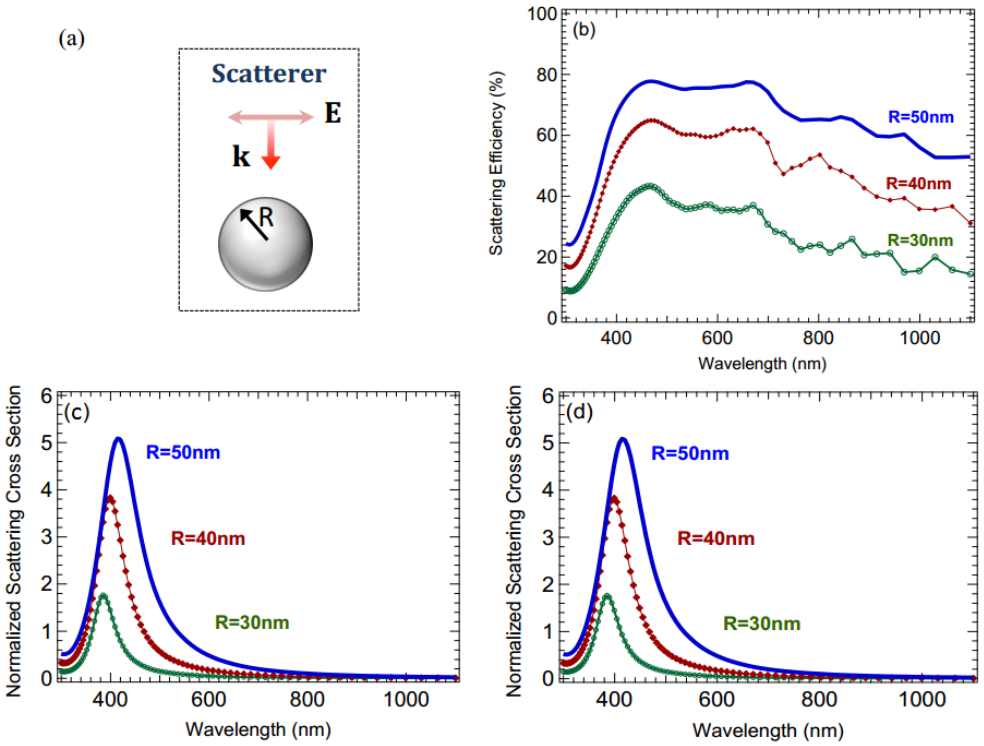

Figure 2.13: (a) The diagram of the simulation (b) Scattering efficiency (c) Normalized scattering cross section (d) Normalized absorption cross section. Silver spheres with radius of 30 nm, 40 nm and 50 nm are put in vacuum (n = 1).

distance d = 50 nm above the surface. As the particle approaches the surface, the normalized scattering cross section decrease. As the particle approaches the surface (d = 0 nm), a very slight red shift of the resonance occurs. As the particle enters the dielectric (d < 0), a significant red shift occurs until the particle's resonance corresponds to that of the particle surrounded by a uniform material of index n = 2. It is also interesting to note that the normalized scattering cross section decreased in magnitude as the sphere approach the surface from either above or below.

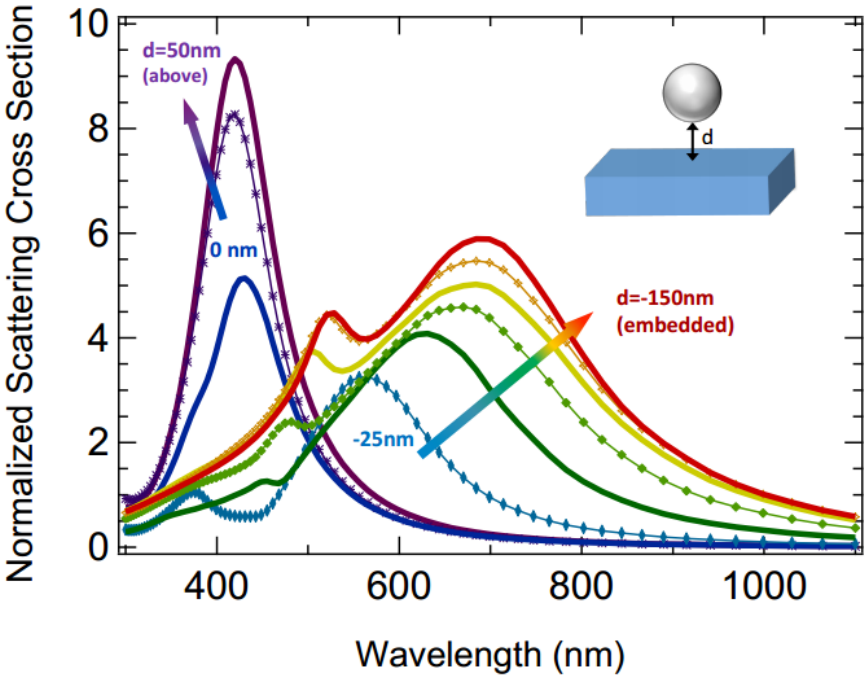

Figure 2.14: Normalized scattering cross section of a spherical silver particle changes with its distance to the substrate. The radius of the sphere is 50 nm. d is the distance from the bottom of the sphere to the surface of the substrate. The distance between each line in the arrows is 25 nm.

2.5 Waveguiding

The simplest waveguide structure consists of a core material surrounded by two cladding dielectric layers. For most guided modes, the refractive index of the core layer is greater than the cladding layers. The solutions to Maxwell's equations in homogeneous media are plane waves of the form:

$$E\left(x,z,t\right) \sim E_0 e^{ik_x x} e^{-k_z|z|} \tag{2.14}$$

where x is the direction of propagation, and k_x and k_z are the wave vector components in the x- and z-directions for angular frequency ω. Two independent sets of solutions exist, transverse magnetic (TM) and transverse electric (TE) modes. TE modes have their electric field component completely in the plane, corresponding to the y-direction in Fig. 2.15. Thus, only the H_x, H_z, and E_y field components exist. For TM modes, the magnetic field is completely in the plane, so that only the E_x, E_z, and H_y components are present. For both sets of confined modes, the boundary conditions at the interfaces dictate that the fields decay exponentially outside of the core region.

By solving Maxwell's equations subject to the appropriate boundary conditions, we obtain the field intensity profiles for the various waveguide modes of a planer multilayer structure. Fig. 2.16 shows the modal profiles (calculated from simulation) at 600 nm with both TE and TM polarizations for a 100 nm thick layer of CdS on the top and either air (a and c) or Ag (b and d) on the backside. These modal profiles are represented by the E-field intensity as a function of position in the waveguide. The modes are largely within the core and decay sharply into the surrounding air or Ag. While we have only depicted a single mode for each case, the number of modes present in the waveguide depends on both the thickness of the slab and on the wavelength of the incident light. All of these modes can contribute significantly to the absorption within the semiconductor, but the differing overlap ratios within the cladding will change the fraction of power in each mode that contributes to useful absorption and the fraction that is lost to other processes.

With the addition of a metal interface, the TE mode changes its shape slightly,

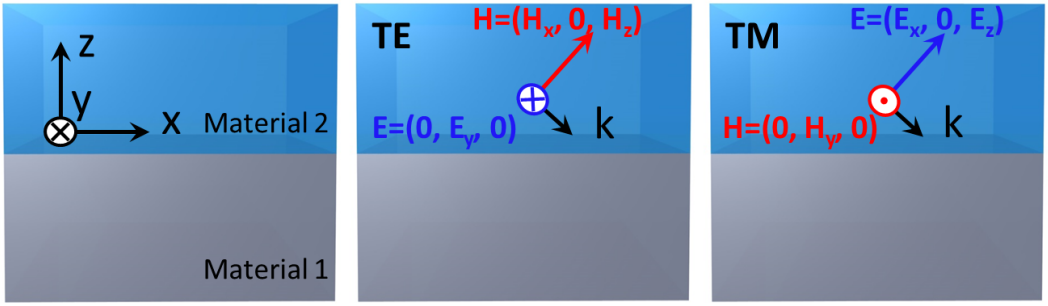

Figure 2.15: TE and TM modes for a simple two-material waveguide. The interface corresponds to $z = 0$.

but there is no substantial change in the location of power. In the TM case, a fundamentally different type of mode is visible when one of the interfaces is metal: the surface plasmon polariton (SPP) mode (Fig. 2.16(d)), which is tightly confined to the semiconductormetal interface and decays exponentially away from each side of the boundary. To further understand this SPP mode, we consider the field components in a simple two material waveguide structure (Fig. 2.15). Letting material 1 be a metal and material 2 be a dielectric, we have the following field components for the TM modes [19]:

$$H_y^2 = H_0 e^{ik_x x} e^{-k_{z_2} z} \tag{2.15}$$

$$E_x^2 = iH_0 \frac{k_{z_2}}{\omega \varepsilon_0 \varepsilon_2} e^{ik_x x} e^{-k_{z_2} z} \tag{2.16}$$

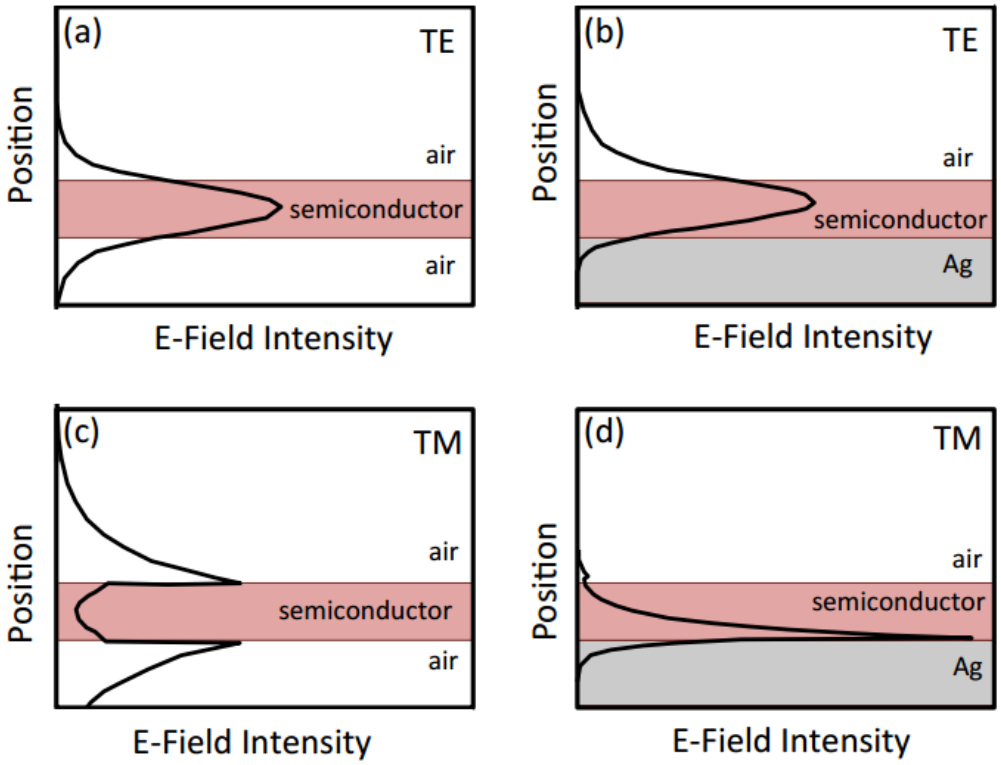

Figure 2.16: Mode profiles for the lowest order TE [(a) and (b)] and TM [(c) and (d)] modes of a simple slab waveguide. When the backside is a metal, it is possible to excite a surface plasmon polariton, which is tightly confined to the metal-semiconductor interface (d).

$$E_z^2 = -H_0 \frac{k_x}{\omega \varepsilon_0 \varepsilon_2} e^{ik_x x} e^{-k_{z_2} z} \tag{2.17}$$

$$H_y^1 = H_0 e^{ik_x x} e^{k_{z_1} z} \tag{2.18}$$

$$E_x^1 = -iH_0 \frac{k_{z_1}}{\omega \varepsilon_0 \varepsilon_1} e^{ik_x x} e^{k_{z_1} z} \tag{2.19}$$

$$E_z^1 = -H_0 \frac{k_x}{\omega \varepsilon_0 \varepsilon_2} e^{ik_x x} e^{k_{z_1} z} \tag{2.20}$$

where the metal has complex $\varepsilon_1(\omega)$ and corresponding k_{z_1}, and the semiconductor has $\varepsilon_2(\omega)$ and k_{z_2}. In the above notation, E_x^1 corresponds to the x-component of the field in material 1.

Enforcing continuity of the tangential component of E (i.e. $E_x^1 = E_x^2$) and the normal component of D (i.e. $\varepsilon_1 E_z^1 = \varepsilon_2 E_z^2$) at the interface yields:

$$\frac{-k_{z_1}}{k_{z_2}} = \frac{\varepsilon_1}{\varepsilon_2} \tag{2.21}$$

which can be satisfied for a metal interface because $Re[\varepsilon_1] < 0$ and both $Re[k_{z,1}] > 0$ and $Re[k_{z,2}] > 0$. Because the H_y component in both materials must satisfy the wave equation, we also have:

$$k_{z1,2}^2 = \varepsilon_{1,2} \left(\frac{\omega}{c}\right)^2 - k_x^2 \tag{2.22}$$

Combining these relations yields the surface plasmon dispersion relation

$$k_x = \frac{\omega}{c} \sqrt{\frac{\varepsilon_1 \varepsilon_2}{\varepsilon_1 + \varepsilon_2}} \tag{2.23}$$

which describes how the wave propagation varies with frequency.

Fig. 2.17 shows the dispersion relation for an SPP mode at the Ag/air interface. Modes to the right of the light line, which describes light propagation in material 2, are bound to the interface. At low frequency, the SPP modes are close to, but to the right of, the light line. At resonance, where $\varepsilon_1 = -\varepsilon_2$, the modes are

highly confined with large wave vectors, and propagation lengths are very short, $\sim 1/(2Im(k_x))$. Changes in the optical properties of the surrounding materials can tune the position of resonance throughout the spectrum. Because the modes are confined to the interface, a propagating SPP has most of its power in a small volume of material, and it has been shown that a monolayer of CdSe quantum dots can be made optically thick by SPP absorption [26].

We now show that for the TE case, no bound surface modes exist. Using Maxwell's equations for TE polarization,

$$E_y^2 = E_0 e^{ik_x x} e^{-k_{z_2} z} \tag{2.24}$$

$$H_x^2 = -iE_0 \frac{k_{z_2}}{\omega\mu_0} e^{ik_x x} e^{-k_{z_2} z} \tag{2.25}$$

$$H_z^2 = E_0 \frac{k_x}{\omega\mu_0} e^{ik_x x} e^{-k_{z_2} z} \tag{2.26}$$

$$E_y^1 = E_0 e^{ik_x x} e^{k_{z_1} z} \tag{2.27}$$

$$H_x^1 = iE_0 \frac{k_{z_1}}{\omega\mu_0} e^{ik_x x} e^{k_{z_1} z} \tag{2.28}$$

$$H_z^1 = E_0 \frac{k_x}{\omega\mu_0} e^{ik_x x} e^{k_{z_1} z} \tag{2.29}$$

Note that for this case, $E_x = E_z = H_y = 0$. Enforcing continuity at the interface for the E_y and H_x terms yields:

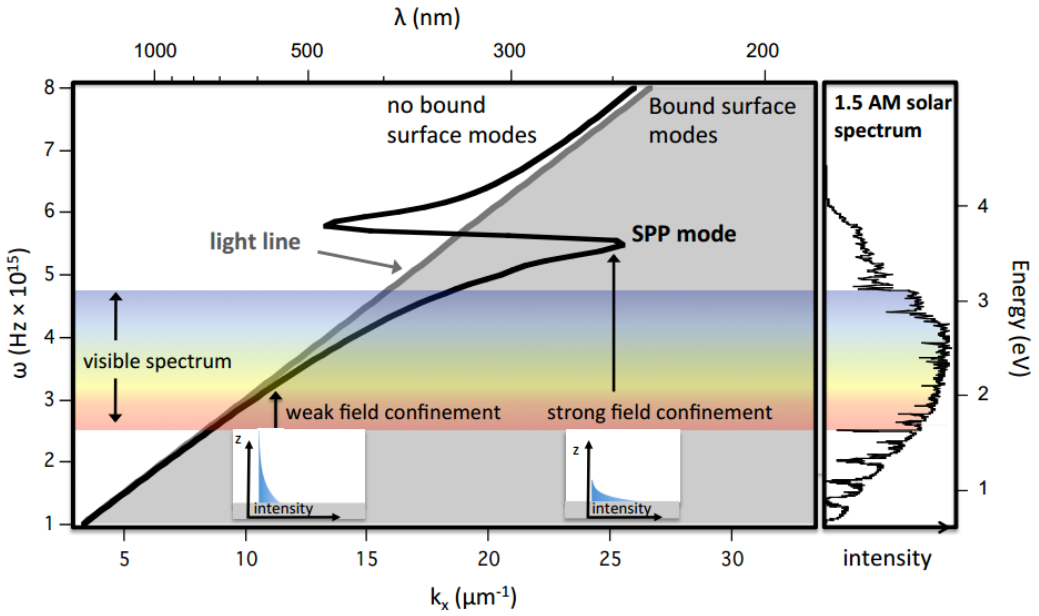

Figure 2.17: Dispersion relation for the surface plasmon polariton mode at the silver/air interface. A significant fraction of the solar spectrum overlaps with the surface plasmon mode. Figure adapted from Ref [21]

$$E_0 \left(k_{z_1} + k_{z_2}\right) = 0 \tag{2.30}$$

Because both $Re\left[k_{z_1}\right] > 0$ and $Re\left[k_{z_2}\right] > 0$, we must have $E_0 = 0$, and thus no surface mode exists under TE polarization.

2.6 Conclusions

For thin film photovoltaic devices, light trapping and optical confinement are critical to device performance. Small metallic particles can be used as high efficiency scatterers that can reduce reflection, yield high local absorption, and increase the

optical path length of the incident light. Further, by coupling into waveguide modes, the incident light can be transformed into confined propagating modes that will increase the absorption probability. All of these effects rely on designing photonic and plasmonic structures that efficiently convert the free space sunlight into localized and propagating modes within the absorber. By careful selection of materials and particle shapes, these resonances can be tailored to most effectively match the absorption properties of the solar cell.

Chapter 3: Quantum dots used as new scatters

In this chapter, we propose a polymer photovoltaic device with a new scattering mechanism based on photon absorption and re-emission in a quantum dot layer. A matrix of aluminum nanorods with optimized radius and period are used to modify the coupling of light emitted from the quantum dots into the polymer layer. Our analysis shows that this architecture is capable of increasing the absorption of an ordinary polymer photovoltaic device by 28%.

3.1 Introduction

Photovoltaic devices offer an appealing alternative to fossil fuel-based energy sources; however, the cost-per-Watt of solar power in many regions is prohibitively high, resulting in a need for low-cost photovoltaics concepts. To this end, polymers have become an attractive alternative to traditional inorganic semiconductors due to their low-cost and ease of fabrication [27–30]. Despite these benefits, polymer photovoltaics have been hindered by their relatively low efficiencies [31] when compared to traditional, inorganic cells. Ineffective absorption and carrier collection results in a decrease of both the short circuit current and the open circuit voltage.

Many routes have been taken to improve the solar conversion efficiencies of polymer solar cells. One option for improving the voltage is the development of tandem polymer cells [32–34]. These devices typically consist of two or three junctions configured in a tandem fashion, which allows for the summation of their voltages, hence resulting in increased power output [35–37]. However, this process adds complexity to the fabrication process due to the requirement of tunnel junctions and current matching conditions throughout the device [38].

In order to increase the generated current in an optically thin cell, higher absorption is needed within the polymer. This can be achieved through the use of surface texturing, nanostructing, plasmonics, or other light trapping architectures [21, 22, 39–50].

Here, we proposed a new mechanism for increasing the efficiency of polymer solar cells through the use of quantum dot (QD) scatterers. QDs are widely used

in photovoltaic applications either as the traditional active layer or to generate multiple excitons from a single incident photon [51]. Recently, QDs have also been used to modify the incoming spectrum for tandem devices to improve the current matching conditions for such a devices [52]. Rather than focusing on multiple carrier generation or modification of the spectrum, we describe the use of QDs to change the directionality of the incident photons to improve coupling to the nearby photoactive layer. High lumenescence QDs can absorb photons that are transmitted through the photoactive polymer layer and then re-emit photons back into waveguide modes of the structure, which can be absorbed with high probability within the active polymer layer. Unlike the traditional usage of QDs for multi-exiton generation or intermediate band solar cells, we use quantum dots as scatterers to boost the absorption within a thin active layer of the cell. We further introduce nanorod structures surrounding the QDs to allow for current collection from the polymer. These nanorods also enable control of the coupling of the incident light to the polymer and of the QD emission into waveguide modes within the device, which can further increase the absorption.

3.2 Modeling

In order to determine the generated photocurrent, we calculate the absorption, emission, and re-absorption rates within the various layers of our structure (Fig. 3.1). The calculation proceeds as follows. First, Maxwell's equations are solved numerically using the Finite Difference Time Domain method (Lumerical FDTD

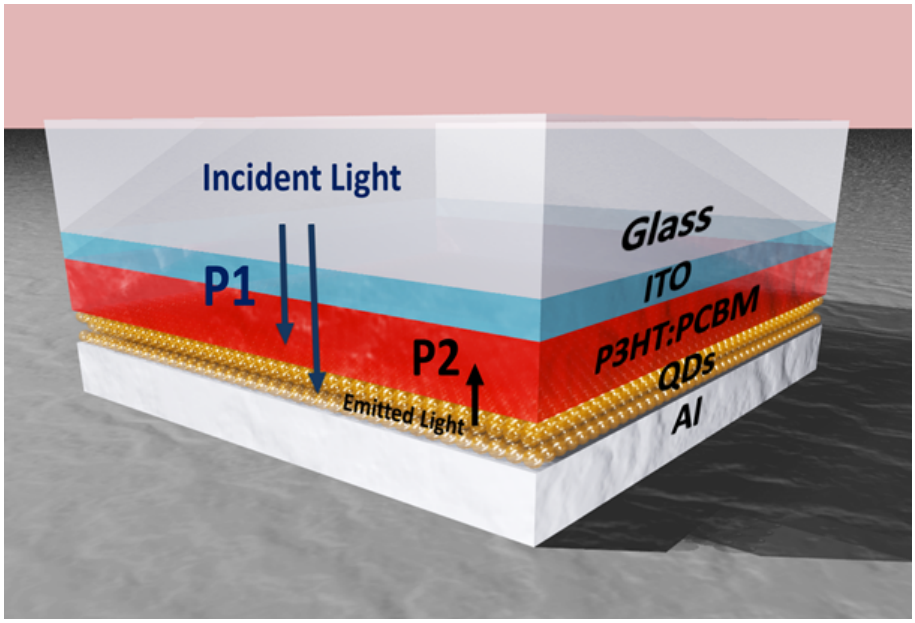

Figure 3.1: Schematic of the polymer cell and simulation procedure. Light is incident from the glass, and useful absorption during the first path (P1) occurs in both the polymer (P3HT:PCBM) and within the QD layer. The QDs will emit photons with a particular probably resulting in a second path (P2) through the cell, which can be absorbed in the polymer.

Solutions) for the structure shown in Fig. 3.1. In this first part, the QDs are treated simply as an absorbing layer described by a complex index of refraction. The number of photons absorbed in both the polymer layer, $N_{poly}(\lambda)$, and in the QD layer, $N_{QDs}(\lambda)$, due to the injection of a plane wave source is calculated [21]. In the second part, we simulate the re-emission of the QDs. The QDs are treated as dipole sources that are distributed uniformly, and the emission spectrum is described by a Gaussian function, $D(\lambda)$, peaked at the emission wavelength. For a typical simulation, 1080 dipoles per unit volume (thickness times the period squared) are used, and the strength of each dipole is weighed by the local absorption due to

plane wave injection. During the emission simulation, the dipole is assumed to be surrounded by a dielectric slab, whose index of refraction is completely real. This assumption restricts further absorption within the QD layer; however, as we show in the following sections, the QDs typically emit into modes with weak overlap with the QD layer. We define the absorptance of the re-emitted photons within the polymer layer, $A_{2nd}(\lambda)$, as the ratio of the number of absorbed photons to the number of emitted photons from the dipole sources. The total number of absorbed photons within the polymer due to both processes is:

$$N_{tot} = \int_{Solar} N_{poly}(\lambda)\, d\lambda + \int_{Solar} N_{QDs}\left(\lambda'\right) d\lambda' \int_{Emission} D(\lambda)\, A_{2nd}(\lambda)\, d\lambda \tag{3.1}$$

The QDs are modeled after experimental data from CdSe quantum dots [53]. In order to obtain the refractive index of the QD layer, we treat the layer as a bulk material and calculate the refractive index from $n = \sqrt{\mu\epsilon}$. With $\mu = 1$, we use a Drude-Lorentz model to calculate the electrical permittivity, ϵ. Using the Beer-Lambert law, we compare the calculated absorption spectrum of a 3 nm thick layer of CdSe QDs with experimental data [53]. Figure 3.2 shows the refractive index used for the simulations is in good agreement with the experimental absorption data [54].

3.3 Results

Following the calculation procedure described above for a simple planar structure (Fig. 3.1), we find that the expected photocurrent is enhanced by 29.4% when the QD layer is present compared to the same structure without the QD layer (5.31

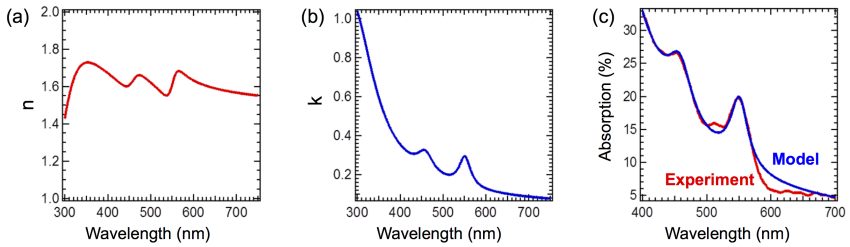

Figure 3.2: The (a) real and (b) imaginary parts of the refractive index of the quantum dots used in our model. (c) Comparison of absorption spectrum of the quantum dots in the model (blue) to the experimental data (red) shows good agreement.

$\times$ 10^{20} photons absorbed). 5.8% of the enhancement is due to absorption in the polymer as a result of the emission of the QDs, and the rest of enhancement results from thin film interference effects that occur due to the addition of the QD layer. Despite the relatively large expected photocurrent generation, photocurrent collection would be difficult for the structure of Fig. 3.1. Because the QDs are acting predominantly as optical scattering structures, an additional conduction path is needed for carriers generated within the polymer. To solve this problem, aluminum nanorods are inserted between the polymer and the aluminum contact to allow electrical conductivity to the back contact, as is shown in Fig. 3.3.

We repeat the simulation procedure outlined in Section 2 for a nanorod array with a period of 220 nm and a nanorod radius of 70 nm. The photons absorbed in the polymer and QD layers are 6.44 $\times$ 10^{20} and 0.52 $\times$ 10^{20}, respectively, during the first simulation. The re-emission from the QDs results in 0.04 $\times$ 10^{20} photons being absorbed during the second step of the simulation. Surprisingly, the total number of photons absorbed in the polymer is 6.48 $\times$ 10^{20}, which is slightly lower

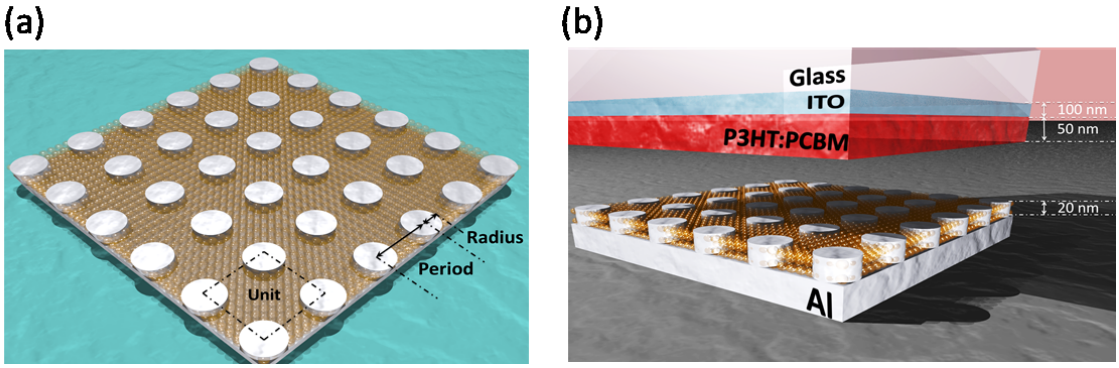

Figure 3.3: (a) Schematic diagram of the aluminum nanorod layer filled with uniformly distributed quantum dots (orange) and (b) cross section of the entire solar cell structure. The orange dotted box in (a) is the simulated unit volume, which contains 1080 dipoles.

than the result obtained from the structure without nanorods. This is the result of inefficient coupling between the incoming light and the structure as well as poor coupling between the QD emission and the polymer absorption.

Optimization. In order to improve the absorption and coupling, a parameter sweep of the radius and period is performed. This optimization process is depicted in Fig. 3.4. The first path absorption shows increased absorption in the polymer layer for large periods and increased absorption in the QD layer for short periods and small radii [Figs. 3.4(a) and 3.4(b)]. Absorption in the aluminum nanorods increases for short periods and large radii due to the increased fraction of metal in the layer containing QDs [Fig. 3.4(c)]. Thus, it is important to reduce the metal fraction in order to avoid ohmic loss. Figure 3.4(d) shows that the coupling efficiency (i.e. the ratio of the number of photons absorbed in the polymer layer due to quantum dot emission to the number of photons emitted by the QDs) is

fairly uniform (second path absorption); however, optimal points are found where the emission is coupled more efficiently into the polymer layer rather than out of the cell or into the surrounding metal.

Because the final absorption consists of two parts (initial absorption in the polymer and secondary absorption in the polymer from QD emission), there is a trade-off between these parameters. Figure 3.5 shows the total number of absorbed photons in the polymer after the entire calculation. Although the total number of photons absorbed depends on both the radius and the periodicity of the array, the overall absorption is relatively insensitive to the exact value of the radius and period for periods in the range of 260 to 500 nm and for radii in the range of 30 to 70 nm. It is possible to couple to both localized and propagating surface plasmon modes by changing the period and radius of the rods [55]; however, the overall absorption is relatively insensitive to these changes for the structure under consideration. The highest value of absorption occurs in the structure with nanorods of 30 nm radius and 260 nm period. This is because the loss in the aluminum is relatively low in nanorods with smaller radii. The total number of photons absorbed in the polymer is 6.84×10^{20}, which has a 28.6% enhancement, and one fifth of the enhancement (6%) comes from the emission of the QDs. The photocurrent enhancement in this structure is comparable to that of the planar structure; however, there is now a conduction path for carrier collection.

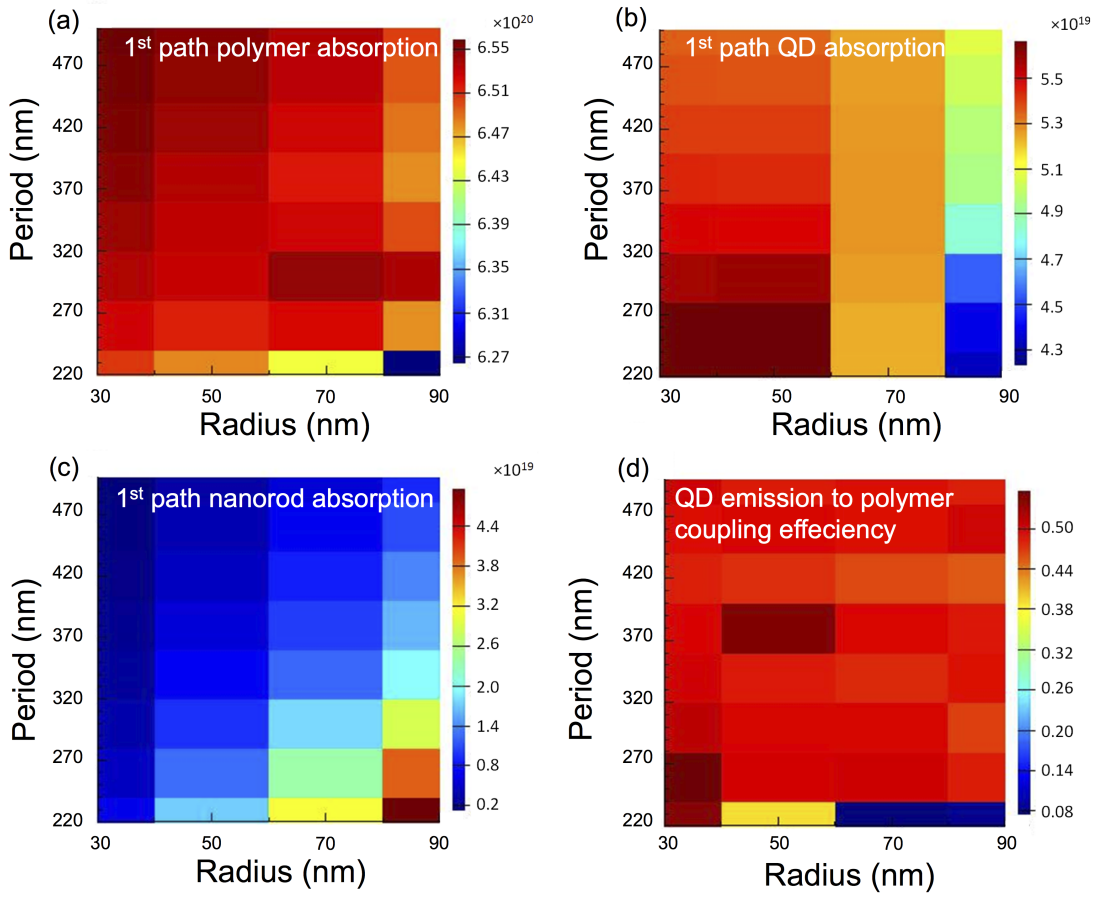

Figure 3.4: The number of photons absorbed in (a) the polymer, (b) the QD layer, and (c) the aluminum nanorods during the first path. (d) The coupling efficiency of the emitted photons from the QDs to the polymer layer.

3.4 Discussion

Because the inclusion of a QD layer can lead to absorption enhancements either through modifying the initial absorption or through the reemission process, it is necessary to consider both effects in further detail.

By adding the QD layer to the structure, we find that the peak in the number of absorbed photons moves toward the middle of the polymer layer instead of staying on

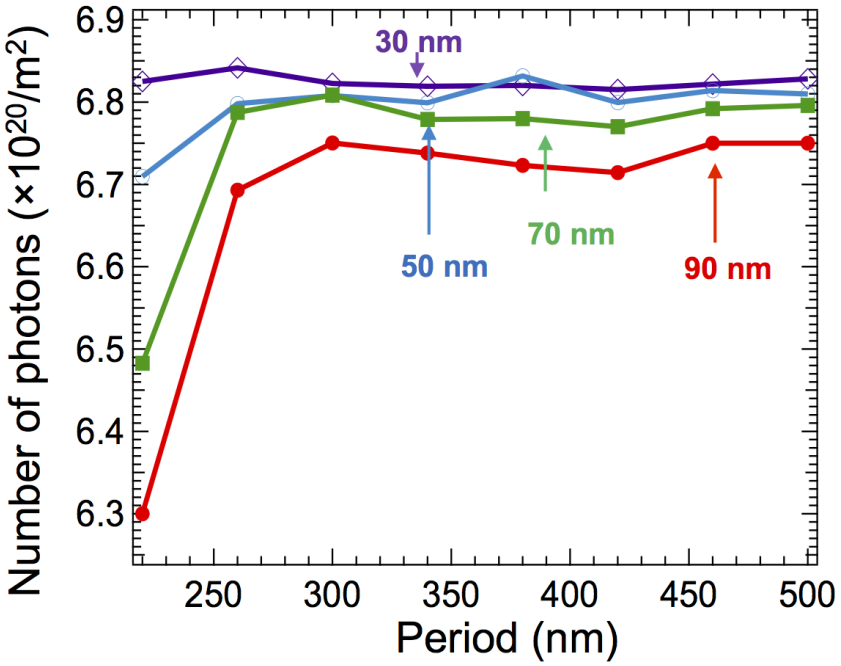

Figure 3.5: Total number of photons absorbed in the polymer for different radii and periods of the nanopillar array (including the absorption from the emission of QDs). The radii are 30 nm (purple), 50 nm (blue), 70 nm (green), 90 nm (red).

the top boundary, as is shown in Fig. 3.6(a). Figure 3.6(c) shows that the absorption enhancement occurs over almost the entire polymer region, when compared to Fig. 3.6(b). In addition, because the QDs absorb a certain fraction of the energy that would otherwise be lost to absorption within the aluminum [compare Figs. 3.6 (b) and (c)], this energy has the possibility of being recovered through the re-emission process. Further, because the QD emission allows for a second absorption path for photons in the polymer, this process leads to an additional enhancement, as can clearly be seen in Fig. 3.7. Interestingly, the absorption around 559 nm reaches 100% even though the QD to polymer coupling efficiency is less than 100%. This is

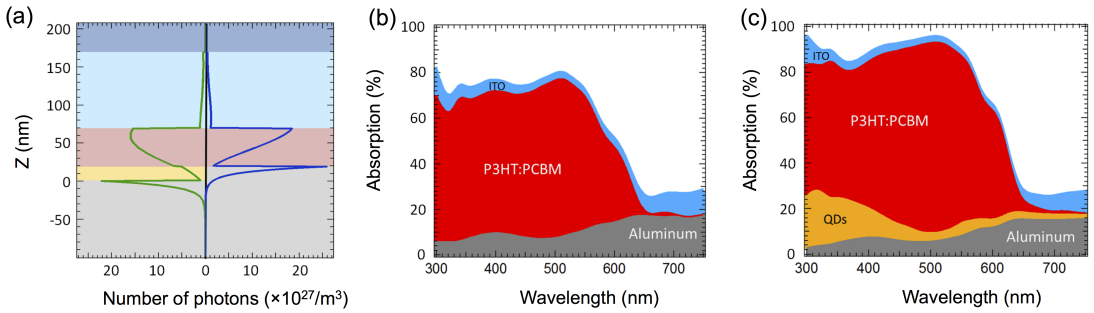

Figure 3.6: Absorption comparison during the first path for the traditional polymer cell and the QD enhanced polymer cell. (a) Cross section showing the number of absorbed photons per cubic meter with (green solid line) and without (blue solid line) the QD layer. (b) The absorption in each layer of the ordinary polymer cell. (c) The absorption in each layer of our QD enhanced polymer cell. The absorption in the QDs occurring for $\lambda > 600$ nm will not contribute to the re-emission process because they do not contain sufficient energy to cause emission.

due to fact that photons emitted at 559 nm could have resulted from the absorption of photons of a different wavelength. Thus, because there are more 559 nm photons available after emission than there were from the initial spectrum, the absorption could in principle exceed 100% at a particular wavelength. If the QDs do not have 100% fluorescence efficiency, the peak absorption is reduced, as shown in Fig. 3.7.

To explain the increased absorption, we note that the QDs can emit into waveguide modes of the structure. Here we consider the waveguide modes that exist within the planar structures at a wavelength of 559 nm, which corresponds to the emission peak of the QDs. Our simulations show that two modes can exist in the structures with or without the QD layer: transverse electric (TE) and transverse magnetic (TM). The normalized electric field intensities of the TE and TM modes are depicted in Fig. 3.8.

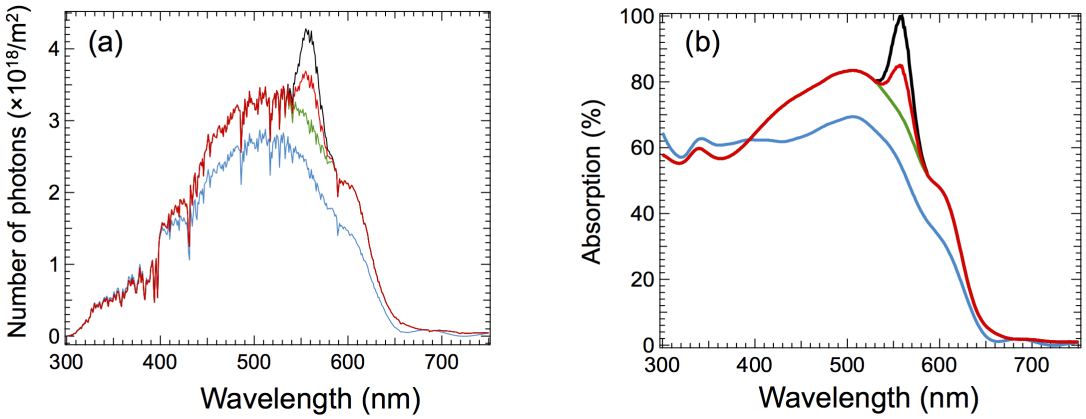

Figure 3.7: The comparison of absorption spectra of the polymer (blue) and the QD enhanced polymer (Green: without QD emission, Red: with 50% QD emission, Black: with 100% QD emission) cells without the nanorod array. (a) The absorbed number of photons as a function of wavelength under AM 1.5G solar illumination. (b) The percentage of photons absorbed compared to the incident solar illumination. Note: the peak at $\sim$ 560 nm results from the absorption of photons emitted from the QDs and could in principle exceed 100% due to the redistribution of higher energy photons. The radius and period of the nanorods are 30 nm and 260 nm, respectively.

To determine whether or not the QDs can emit efficiently into the guided modes of the structure, we determine the electric field intensity created by a dipole positioned in the center of the QD layer. Figure 3.9 shows that the field profiles, as determined 100 nm from the dipole in the X-Y direction, are very similar to the fundamental modes of the structure. This correspondence indicates that the QDs emit efficiently into either TE or TM modes depending on the dipole orientation. Because the dipole orientation is random, it is more likely for the dipoles to emit into the TE mode due to the symmetry of this 2-D structure. This result also suggests that our assumption of weak secondary absorption in the QD layer due to

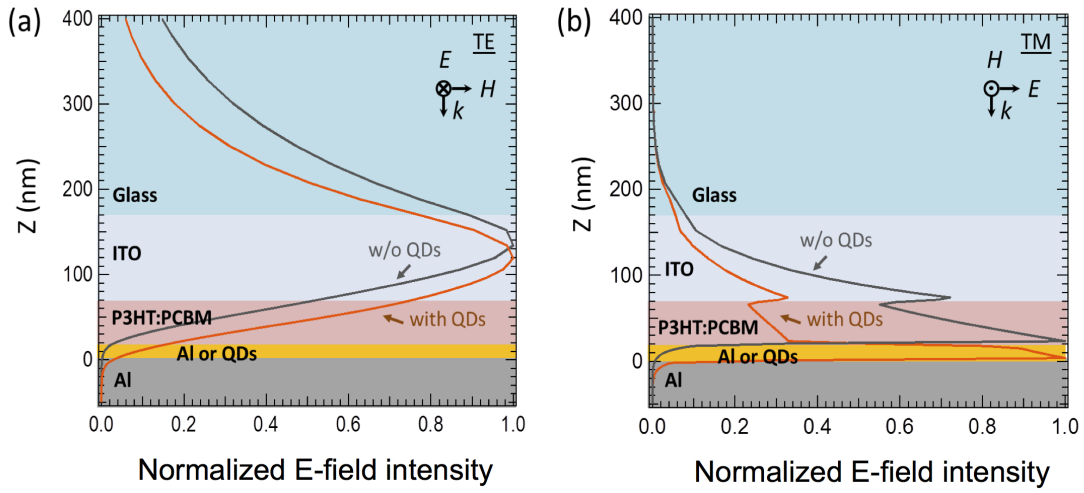

Figure 3.8: Electrical field intensity of fundamental (a) TE and (b) TM modes in the solar cell. Orange and gray lines are the field intensities for structures with and without quantum dots, respectively. The layers are depicted on the background: glass (blue), ITO (light blue), polymer (red), QDs (yellow), and aluminum (gray); note: for the structure without QDs, the yellow layer is aluminum. The analysis is performed at the emission peak of QDs (i.e. 559 nm).

QD emission is valid.

Although we have focused on a 50 nm thick polymer layer to ensure collection of generated charges, the enhancement persists for a range of thicknesses (Fig. 3.10). As the thickness increases more photons are absorbed by the polymer layer, leaving fewer photons to be absorbed by the QDs. As a result, the absorption due to QD emission becomes smaller. The effect of the QDs is most pronounced for polymer thicknesses below 80 nm. For thicker films the interference conditions change for the first pass absorption, and the structure without quantum dots performs better for polymer thicknesses from 80 to 140 nm. For thicker films, the QDs again improve the performance; however, charge collection becomes more critical to the design for

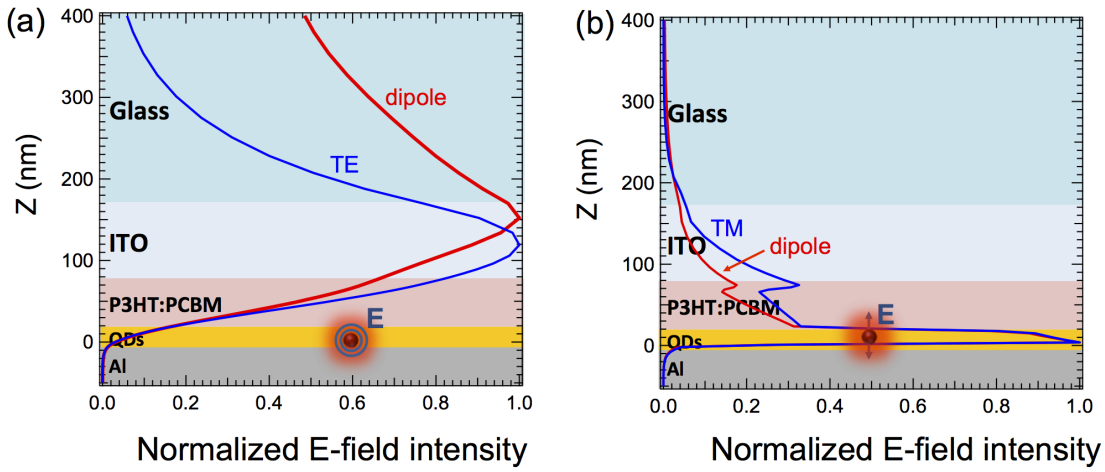

Figure 3.9: The coupling of dipole emission into the waveguide mode of the solar cell. Blue data are fundamental (a) TE and (b) TM modes, and red data are the field intensities resulting from dipole emission. The layers are depicted on the background: glass (blue), ITO (light blue), polymer (red), QDs (yellow) and aluminum (gray).

these thicker films.

3.5 Conclusion

In conclusion, we have shown that a new method, using QDs as scatters, has the ability to increase the absorption in a polymer layer of an organic solar cell while simultaneously reducing the loss in the aluminum contact layer, thus increasing the efficiency of the polymer solar cell. Further, the emission from the QDs can be coupled into waveguide modes of the structure, which leads to the largest enhancements. There are two possible modes that exist within these thin cells, and the TE mode plays the most important role in determining the absorption performance. While the results presented here pertain to polymer solar cells, these

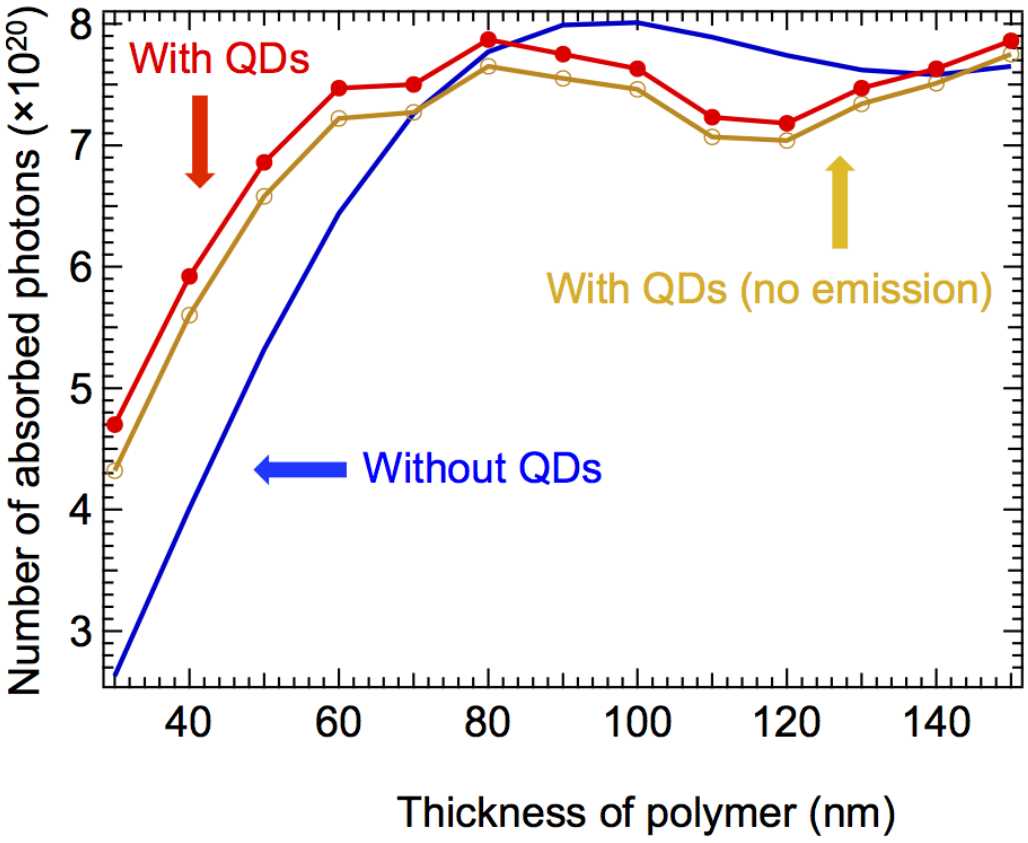

Figure 3.10: The number of absorbed photons is influenced by the thickness of the polymer layer. The structure with quantum dots outperforms the structure without quantum dots for polymer thicknesses below 80 nm. For thicker films, there is a tradeoff between carrier collection and thin-film interference effects.

concepts can be extended to other photovoltaic systems, detectors, or sensors.

Chapter 4: Nanostructured solar cells

The Shockley-Queisser limit describes the maximum solar energy conversion efficiency achievable for a particular material and is the standard by which new photovoltaic technologies are compared. This limit is based on the principle of detailed balance, which equates the photon flux into a device to the particle flux (photons or electrons) out of that device. Nanostructured solar cells represent a novel class of photovoltaic devices, and questions have been raised about whether or not they can exceed the Shockley-Queisser limit. In this chapter, we show that single-junction nanostructured solar cells have a theoretical maximum efficiency of $\sim 42\%$ under AM 1.5 solar illumination. While this exceeds the efficiency of a non-concentrating planar device, it does not exceed the Shockley-Queisser limit for a planar device with optical concentration. We consider the effect of diffuse illumination and find that with optical concentration from the nanostructures of only $\times 1000$, an efficiency of 35.5% is achievable even with 25% diffuse illumination. We conclude that nanostructured solar cells offer an important route towards higher efficiency photovoltaic devices through a built-in optical concentration.

4.1 Introduction

In 1961, Shockley and Queisser developed a theoretical framework for determining the limiting efficiency of a single junction solar cell based on the principle of detailed balance equating the incoming and outgoing fluxes of photons for a device at open-circuit conditions [5]. This model incorporates various light management and trapping techniques including photon recycling, optical concentration, and emission angle restriction [5, 6, 56]. It was recently suggested that a nanowire solar cell could exceed the Shockley-Queisser (SQ) limit based on its geometry [57]; however, without exploiting 3rd generation photovoltaic (PV) concepts which break the assumptions of Shockley and Queisser (e.g. multi-exciton generation, hot carrier collection, etc) [58–60], even nanowire solar cells should be bounded by the SQ limit. Here we show that for *any* nanostructured solar cell (e.g. composed from wires, cones, pyramids, etc.), the limiting efficiency is identical to that of a planar solar cell with concentrating optics and that the improvement results strictly from an increase in the open-circuit voltage. This formalism leads to a maximum efficiency of $\sim 42\%$ for a nanostructured semiconductor with a bandgap energy of ~ 1.43 eV (e.g. GaAs) under AM 1.5G illumination [8].

The SQ limit is reached by applying the principle of detailed balance to the particle flux into and out of the semiconductor [5]. For every above bandgap photon that is absorbed by the semiconductor, one electron-hole pair is generated. The maximum possible efficiency is achieved when non-radiative recombination is absent, and all generated carriers are either collected as current in the leads or recombine,

emitting a single photon per electron-hole pair. The total generated current is:

$$I_{total} = q\left[N_{abs} - N_{emit}\left(V\right)\right] \tag{4.1}$$

where q is the charge of an electron, and N_{abs} and N_{emit} are the numbers of photons per unit time that are absorbed or emitted by the photovoltaic device, respectively. These rates can be calculated as [6]:

$$\begin{aligned} N\left(\theta_{max}, V, T\right) &= \int_0^{\infty}\int_{\phi=0}^{2\pi}\int_{\theta=0}^{\theta_{max}} \sigma_{abs}\left(\theta,\phi,E\right) \\ &\quad \times F\left(E,T,V\right)\cos\left(\theta\right)\sin\left(\theta\right) d\phi d\theta dE \end{aligned} \tag{4.2}$$

where $\sigma_{abs}(\theta,\phi,E)$ is the absorption cross-section, $F(E,T,V)$ is the spectral photon flux, and θ_{max} is the maximum angle for absorption (for N_{abs}) or emission (for N_{emit}). For a bulk planar cell, the absorption cross-section is given by $\sigma_{abs}(\theta,\phi,E) = A_{cell} \times a(\theta,\phi,E)$, where A_{cell} is the top illuminated surface area of the cell and $a(\theta,\phi,E)$ is the angle dependent probability of photon absorption for incident photons of energy E. In the simplest case, $a(\theta,\phi,E)$ is a step-function going from 0 (for $E < E_g$) to 1 (for $E \geq E_g$). The spectral photon flux can be obtained from the generalized Planck blackbody law [7]:

$$F\left(E,T,V\right) = \frac{2n^2}{h^3c^2}\frac{E^2}{e^{\frac{E-qV}{k_bT}} - 1} \tag{4.3}$$

where h is Planck's constant, k_b is Boltzmann's constant, c is the speed of light, n is the refractive index of the surroundings, which is usually taken to be vacuum ($n = 1$), and qV characterizes the quasi-Fermi level splitting when describing emission from the cell. The incoming flux from the sun can be obtained from experimental data (e.g. AM 1.5 solar spectrum [8]) or from the blackbody expression above with $V = 0$ and where $\theta_{max} = \theta_s = 0.267°$ is the acceptance half-angle for incident light from the sun at temperature $T = T_s = 5760$ K. The outgoing flux from the cell

is given by Eq. [4.2] for a cell temperature $T_c = 300$ K, operating voltage V, and emission half-angle $\theta_{max} = \theta_c = 90°$. At open-circuit conditions, there is no current extracted, and the current balance equation becomes

$$\begin{aligned} 0 &= qN\left(\theta_s, T_s, V = 0\right) + qN\left(\theta_c, T_c, V = 0\right) \\ &\quad -qN\left(\theta_c, T_c, V = V_{oc}\right) \end{aligned} \tag{4.4}$$

where the middle term corresponds to absorption due to emission from the ambient surroundings, also at $T = 300\ K$; however, this term is much smaller than the flux from the sun. Thus, the light generated current is given by $I_L = qN(\theta_s, T_s, V = 0)$ and the dark current, in the radiative limit, is given by $I_0 = I_R\left[\exp(\frac{qV}{k_B T_c}) - 1\right] = qN(\theta_c, T_c, V) - qN(\theta_c, T_c, V = 0)$, where I_R is the reverse saturation current. Solving Eq. [4.4] for the voltage yields the common expression for the open-circuit voltage [5, 8]:

$$V_{oc} = \frac{k_B T_c}{q} \ln\left(\frac{I_L}{I_R} + 1\right) \approx \frac{k_B T_c}{q} \ln\left(\frac{I_L}{I_R}\right) \tag{4.5}$$

which is valid for both bulk planar solar cells and nanostructured solar cells with the appropriate absorption cross-sections as described in the next section.

4.2 Results

4.2.1 Nanostructured solar cells with built-in optical concentration.

To achieve the maximum efficiency, we need to increase the light generated current compared to its bulk form or reduce the reverse saturation current to increase V_{oc}. For any absorbing structure, Eqs. [4.2, 4.3, 4.4, 4.5] can be used to determine the

resulting V_{oc} numerically; however, for the limiting case, we will consider a simple analytical expression. For maximum V_{oc}, we want the absorption cross-section to be maximized for angles near normal incidence up to an angle θ_m (where $\theta_s \leq \theta \leq \theta_m$) and minimized for all other angles $\theta_m \leq \theta \leq \theta_c$, where θ_m is some angle defined by the structure. We can define this piece-wise function for the absorption cross-section as: $\sigma_{abs}(\theta : 0 \rightarrow \theta_m) = \sigma_{max}$ and $\sigma_{abs}(\theta : \theta_m \rightarrow \theta_c) = \sigma_{min}$, which allows us to perform the solid angle integration to determine the light and dark currents:

$$\begin{aligned} I_L &= qN\left(\theta_s, T_s, V=0\right) \\ &= q\sigma_{max}\int_{E_g}^{\infty}\int_{\phi=0}^{2\pi}\int_{\theta=0}^{\theta_s} F\left(E, T_s, V=0\right) \\ &\quad \times \cos\left(\theta\right)\sin\left(\theta\right) d\phi d\theta dE \\ &= \frac{\sigma_{max}}{A_{cell}} I_{L,0} \end{aligned} \tag{4.6}$$

where $\sigma_{abs} = 0$ for $E < E_g$, $I_{L,0}$ is the light generated current for an ideal bulk cell of area A_{cell}, and

$$\begin{aligned} I_R &= qN\left(\theta_c, T_c, V=0\right) \\ &= \frac{\pi q\sigma_{min}}{2}\left[\cos\left(2\theta_m\right) - \cos\left(2\theta_c\right)\right] \\ &\quad \times \int_{E_g}^{\infty} F\left(E, T_c, V=0\right) dE \\ &\quad + \frac{\pi q\sigma_{max}}{2}\left[1 - \cos\left(2\theta_m\right)\right] \\ &\quad \times \int_{E_g}^{\infty} F\left(E, T_c, V=0\right) dE \\ &= \frac{\sigma_{max}+\sigma_{min}+(\sigma_{min}-\sigma_{max})\times\cos(2\theta_m)}{2A_{cell}} I_{R,0} \end{aligned} \tag{4.7}$$

where $I_{R,0}$ is the reverse saturation current for a bulk cell. Substituting these expressions into Eq. [4.5], we have

$$
\begin{aligned}
V_{oc} &\approx \frac{k_B T_c}{q} \ln\left[\frac{2\sigma_{max}}{\sigma_{max}+\sigma_{min}+(\sigma_{min}-\sigma_{max})\cos(2\theta_m)}\right] \\
&\quad + \frac{k_B T_c}{q} \ln\left[\frac{I_{L,0}}{I_{R,0}}\right] \\
&= \frac{k_B T_c}{q}\left[\ln\left(\frac{I_{L,0}}{I_{R,0}}\right) + \ln(X)\right]
\end{aligned}
\tag{4.8}
$$

where

$$
X = \frac{2\sigma_{max}}{\sigma_{max} + \sigma_{min} + (\sigma_{min} - \sigma_{max})\cos(2\theta_m)} \tag{4.9}
$$

Thus, the open-circuit voltage for a nanostructured device takes on the same form as the open-circuit voltage for a macroscopic concentrating system, where X is the concentration factor [8]. For maximum concentration, we consider the limit as $\theta_m \to \theta_s$ and $\sigma_{min} \to 0$, yielding

$$
X = \frac{2}{1 - \cos(2\theta_s)} \approx 46,050 \tag{4.10}
$$

which is the same as the maximum concentration factor that is obtained for a macroscale concentrator and results in a maximum solar energy conversion efficiency of $\sim 42\%$. For practical devices it is reasonable to assume a minimum value of σ_{min} corresponding to the geometric cross-section of the device, $\sigma_{min} \to \sigma_{geo}$. For this case, and with $\cos(2\theta_m) = \cos(2\theta_s) \approx 1$, we get $X = \sigma_{max}/\sigma_{geo}$, and the open-circuit voltage reduces to:

$$
V_{oc} = \frac{k_B T_c}{q} \ln\left[\frac{\sigma_{max}}{\sigma_{geo}}\left(\frac{I_{L,0}}{I_{R,0}}\right)\right] \tag{4.11}
$$

Finally, the power conversion efficiency is given by $\eta = I_L V_{oc} FF / P_{in}$, where FF is the fill-factor, which can be obtained from the $I - V$ characteristic defined by Eq. [4.1], and P_{in} is the incident power from the sun. We note that the area used to calculate P_{in} is determined by the illumination area and not the geometric cross-section, which would lead to under counting the number of incident photons.

In general, optical concentration can be achieved using lenses, mirrors, or unique optical nanostructures (see Fig. 4.1(a)). A nanostructured solar cell can result in optical concentration that is similar to the concentration obtained using lens or parabolic mirrors but relies on the wave nature of light. Fig. 4.1(b) shows the power conversion efficiency of recently reported vertically aligned nanowire-based PV cells [57, 61–75]. The optical and geometrical cross-sections are extracted from the current density data and from the geometrical information provided within the references. The vast majority of the experiments are focused on Si, GaAs and InP radial or axial junction nanowire arrays fabricated with various techniques, such as MBE, MOVCD, reactive-ion etching, etc. Generally, $X = \frac{\sigma_{max}}{\sigma_{geo}}$ is found to fall in the range of 1-10 for these structures; however, the actual concentration factor is likely significantly smaller if $\sigma_{min} > \sigma_{geo}$. Additionally, the reduced efficiency in these nanowire structures compared to the theoretical limit is due to significant surface recombination and device and material constraints that could be improved with further experimental development.

4.2.2 The effect of entropic losses on V_{oc}

Next we consider an alternative, but equivalent, approach to understanding the maximum efficiency of a nanostructured PV device by considering the energetic and entropic loss mechanisms [76–78]. The generalized Planck equation can be used to determine the open-circuit voltage of a solar cell operating at the maximum efficiency limit [76, 79, 80]:

$$\begin{aligned} V_{oc} = \; & \frac{E_g}{q}\left(1-\frac{T_c}{T_s}\right)+\frac{k_B T_c}{q}\ln\left(\frac{\gamma_s}{\gamma_c}\right) \\ & -\frac{k_B T_c}{q}\ln\left(\frac{\Omega_{emit}}{\Omega_{abs}}\right) \end{aligned} \tag{4.12}$$

where γ_s and γ_c are blackbody radiation flux terms that depend on E_g, T_s, and T_c. The first term represents a voltage drop related to the conversion of thermal energy into work (sometimes called the Carnot factor). The second term occurs from the mismatch between Bose-Einstein distributions at T_c and T_s [81]. The third term is the voltage loss due to entropy generation as a result of a mismatch between the absorption solid angle and the emission solid angle of the cell. This third term represents a voltage drop of ~ 0.28 V, which can be recovered if $\Omega_{emit} = \Omega_{abs}$. Modification of the directionality of absorption and emission to improve the open-circuit voltage of a solar cell is well-known [82–84] and has recently been shown in experiments [85, 86].

The most common way to recover the entropy loss due to the mismatch between the absorption and emission solid angles is through optical concentration (Fig. 4.2(a)). For a planar solar cell without optical concentration, the absorption solid angle corresponds to the sun's angular extent, i.e. $\Omega_{abs} = 2\pi\left(1-\cos\left(\theta_s\right)\right) =$

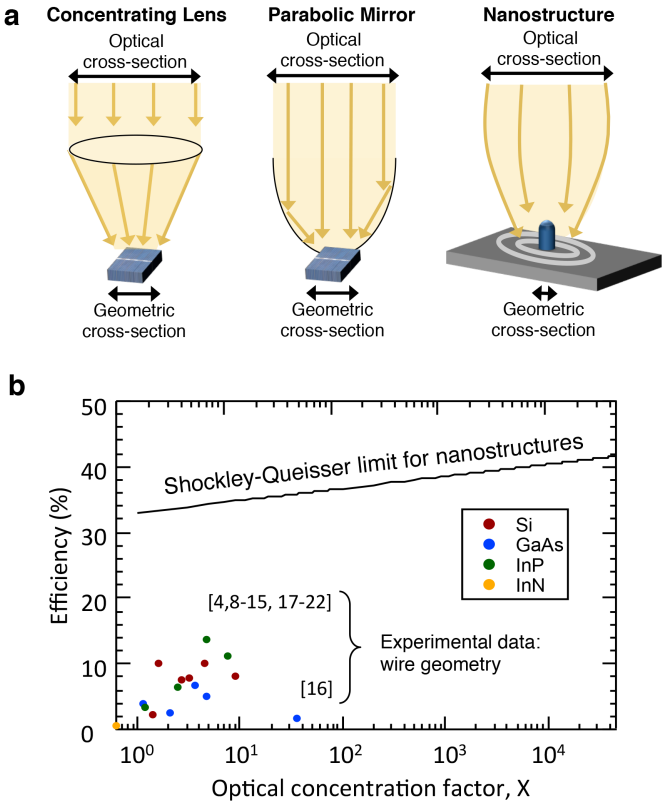

Figure 4.1: The Shockley-Queisser limit for nanostructures. (a) Schematic of the optical concentration implemented by a concentrating lens, parabolic mirror, and using a nanostructure itself (self concentration). (b) The efficiencies of cells with optical concentration. The solid line is the theoretical limit of nanostructured PV devices based on detailed balance, whereas individual dots represents experimental data reported in the literature [57, 61–75].

6.82×10^{-5} sr. However, emission from the cell occurs over $\Omega_{emit} = 4\pi$. The addition of a back reflector reduces the emission solid angle to $\Omega_{emit} = 2\pi$, resulting in a slight voltage improvement [6]. For more substantial voltage improvements, optical concentration is necessary. Optical concentration enables the absorption solid angle to exceed the sun's solid angle and approach the cell's emission solid angle (Fig. 4.2(a)), which could largely increase the V_{oc}.

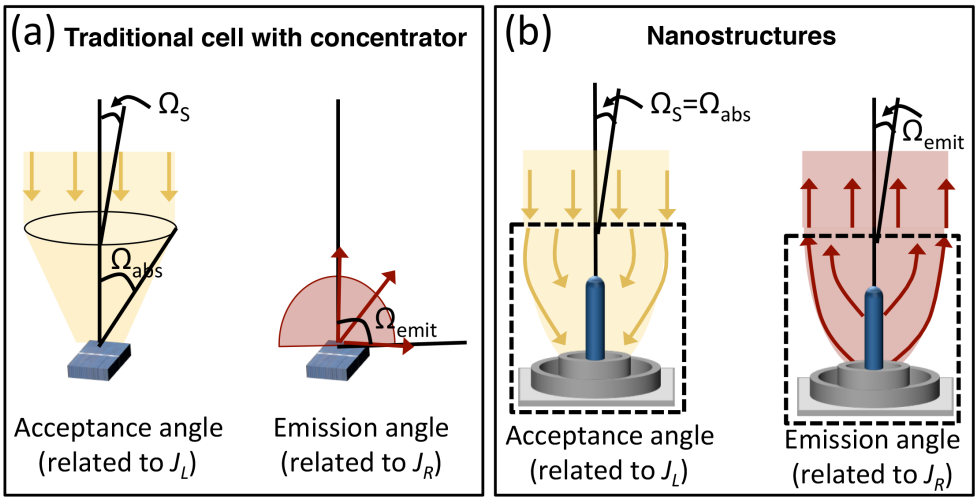

Figure 4.2: Nanostructures can reduce the mismatch between absorption and emission angles. (a) A traditional planar solar cell with concentrator increases Ω_{abs} to approach Ω_{emit}, thus reducing the entropy generation caused by their mismatch. (b) Similarly, a nanostructured solar cell can reduce the difference between Ω_{abs} and Ω_{emit}.

Properly designed photovoltaic nanostructures can have the same effect, reducing the entropy generation by either increasing Ω_{abs} or by reducing Ω_{emit} in an attempt to achieve $\Omega_{emit} = \Omega_{abs}$ (Fig. 4.2(b)). From a device point-of-view, Ω_{abs} is related to the light generated current density, $J_L = I_L/A$, and Ω_{emit} is related to the reverse saturation current density, $J_R = I_R/A$. Because the V_{oc} depends on their ratio (see Eq. [4.5]), increasing Ω_{abs} will have the same affect as decreasing Ω_{emit}. Thus, the voltage improvement can equivalently be seen from the thermodynamics of reduced entropy generation or from the device aspects of the p-n junction.

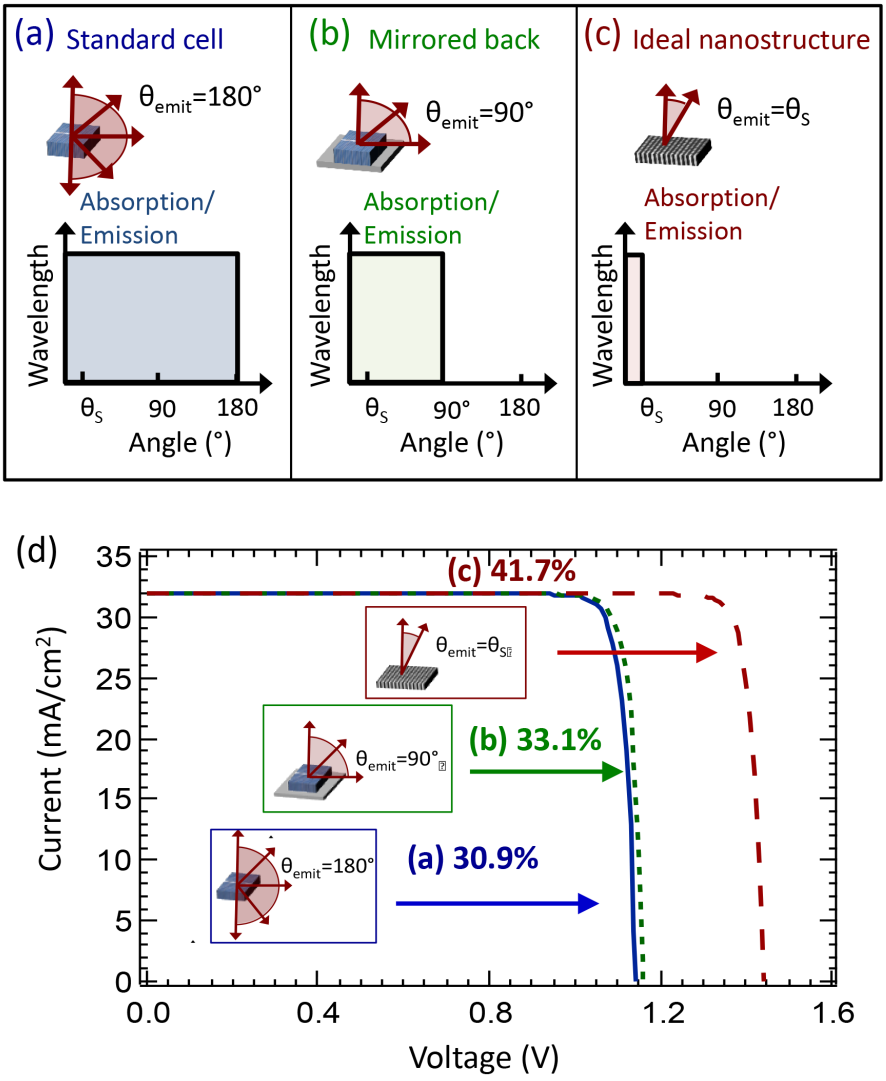

Figure 4.3: Modification of absorption and emission results in an ideal PV nanostructure achieving $> 40\%$ power conversion efficiency. Emission and absorption for (a) slab without back reflector (i.e. light can escape through the back surface without reflection), (b) slab with back reflector, and (c) ideal nanostructured cell. The emission and absorption are represented in terms of their half-angle, θ. Absorption/emission over all angles (standard cell) corresponds to $\theta = 180°$; however, the illumination from the sun is only over a subset of half-angles from 0 to θ_s. Thus, the mismatch between θ_s and θ_{emit} results in a decreased voltage. (d) I-V curves corresponding to the three structures (a-c). All structures are illuminated with the AM 1.5G spectrum and show increased V_{oc} as $\theta_{emit} \rightarrow \theta_s$.

According to Kirchhoff's law, the emissivity and absorptivity of a solar cell are equal in thermal equilibrium [6, 87]. For a standard cell without back reflector, the device can absorb the incident power from all directions and hence will emit in all directions (Fig. 4.3(a)). The addition of a back reflector reduces both absorption and emission from the back surface (Fig. 4.3(b)); however, this has no effect on the absorption of the incident solar power because no illumination is coming from the back. Thus, I_L is unaffected by the addition of the back reflector but I_R is reduced (note: technically I_L could be slightly increased due to an increased path length in thin or low absorption materials, resulting in a small increase in V_{oc}). An ideal nanostructure would allow for absorption only over the range of angles corresponding to the incident illumination of the source, i.e. the sun (Fig. 4.3(c)). The current-voltage characteristics for these devices show that a back reflector yields a $\sim 2\%$ increase in efficiency over the traditional planar device, and an ideal nanostructure yields a $\sim 11\%$ improvement, resulting in a $\sim 42\%$ efficient device.

4.2.3 Effect of diffuse illumination

While the maximum power conversion efficiency is achieved with 100% direct illumination (i.e. the incident light is completely within the solid angle defined by θ_s), an efficiency of $\sim 38\%$ can be achieved when 25% of the incident illumination is diffuse (Fig. 4.4), which is typical of many geographic regions. Incident illumination on earth contains both direct and diffuse components (due to scattering of the incident light). Using traditional macroscopic concentrating optics, light is concentrated for

all wavelengths, and only the direct components can be used. Alternatively, nanostructures typically have a wavelength-dependent response and may only be able to concentrate light over a particular bandwidth, e.g. from the semiconductor bandgap energy (E_{sc}) to some cut-off energy ($E_{cut-off}$). This limited bandwidth for concentration is beneficial when the illumination is not 100% direct, because the diffuse components that lie outside this range can still be collected.

Fig. 4.4 shows that efficiencies $> 35\%$ can be achieved even when the illumination contains a significant fraction of diffuse light. The nanostructures depicted in Fig. 4.4 are able to concentrate the incident light from E_{sc} to $E_{cut-off}$ and are unable to concentrate light with energies $> E_{cut-off}$, which corresponds to absorption of diffuse light in that bandwidth. For $E_{cut-off} = 1.74$ eV, X = 1,000, and 25% diffuse illumination, the nanostructured devices reach an efficiency of 35.5%.

4.2.4 Numerical simulation of nanowire PV.

While the above discussion is general and provides the limiting efficiency of *any* nanostructured solar cell (e.g. wires, cones, pyramids, etc.), explicate cell architectures can be studied via numerical simulation. There are no implicit assumption about the directionality of the absorption or emission; these quantities are numerically calculated directly for each structure. We have simulated a bulk (80 μm thick) GaAs solar cell and a nanowire solar cell with the same thickness (with periodicity of 300 nm and radius of 75 nm) using the S4 simulation package [88] to obtain the absorption profiles. We then solved the detailed balance expression numerically [89,90].

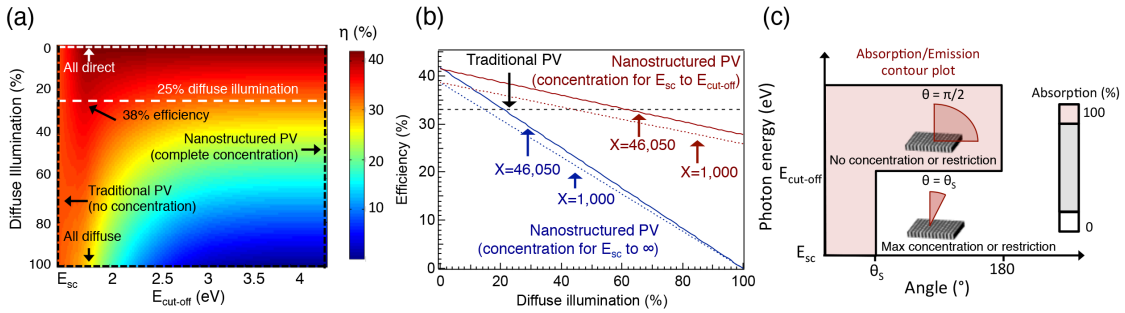

Figure 4.4: Effect of diffuse illumination. (a) Contour plot showing the influence of diffuse illumination on nanostructured PV as the cut-off energy for nanoscale concentration ($E_{cut-off}$) is varied, assuming maximum concentration (X = 46,050). E_{sc} corresponds to the semiconductor bandgap of the device. (b) 3 slices of the contour plot in (a) corresponding to $E_{cut-off}$ = 1.43 eV (traditional PV), $E_{cut-off}$ = 1.74 eV (concentration for photons from E_{sc} to $E_{cut-off}$), and $E_{cut-off} \rightarrow \infty$ (concentration for all incident photons); similar calculations performed for X = 1,000 are also shown. The nanostructured device with complete concentration (i.e. concentration for all energies of incident photons) outperforms traditional PV when diffuse illumination accounts for $< 20\%$ of the incident light. The nanostructured device with partial concentration (corresponding to concentrating only light with energies 1.43 - 1.74 eV) outperforms the traditional device when the incident light is $< 60\%$ diffuse. With only modest concentration (X = 1,000), the device has an efficiency of 35.5% under 25% diffuse illumination. (c) Absorption contour plot and schematic depicting a nanoscale device that is able to concentrate light with energies E_{sc} to $E_{cut-off}$ but unable to concentrate light with energy greater than $E_{cut-off}$.

A similar method was recently used to calculate the detailed balance efficiency for an InP nanowire array, and an efficiency improvement of 1.5% was reported compared to a bulk device [91]. For simplicity, we used the blackbody spectrum in the following calculations. The nanowires are embedded within a material with an index of refraction of n = 2.66, and both the nanowire and planar structures are coated with a double-layer antireflection coating (a 52 nm layer with n = 2.66 and a 98

nm layer with n = 1.46). The antireflection coating is designed to maximize the efficiency of the bulk GaAs cell. The integrated short circuit current density is almost identical for both cases ($< 1\%$ difference); however, the emitted power density is significantly different. Because a large amount of the radiated power is near the bandgap, the lower absorption rate near the bandgap that occurs with the nanowire structure leads to a decrease in emission. This effect is demonstrated in Fig. 4.5(d), where the bulk cell has a higher reverse saturation current density compared to the nanowire cell with same thickness. The reverse saturation current of the nanowire cell decreases by 3.46%, and the absorption increases by 0.38%. As a result, the V_{oc} increases by 1 mV due to these combined effects in the nanowire device, and thus, the nanowire solar cell has a slightly higher efficiency than the bulk device (28.22% vs. 28.09%).

Ideally, an optical structure should be designed to minimize absorption for angles greater than θ_s, particularly near the semiconductor bandgap, which is where the emission is peaked. To emphasize this effect, we consider a smaller radius nanowire (40 nm), which will have increased optical concentration. In order to minimize the loss in photogenerated current, the periodicity is decreased to 200 nm, and the nanowire length is set to 2 μm, which is a reasonable thickness for a GaAs cell. Fig. 4.5(c) shows this device whose absorption near the bandgap is limited so that the reverse saturation current density is one order of magnitude smaller than that of the bulk cell (Fig. 4.5(d)). This nanostructuring leads to the reverse saturation current decreasing from 8.751×10^{-18} to 9.946×10^{-19} A/m^2. Although the absorption is also decreased (J_L decreased from 362.68 to 237.55 A/m^2), the

V_{oc} is increased from 1.169 V to 1.214 V, showing an improvement of 45 mV in V_{oc}. This result suggests that nanostructures that incorporate more complexity may yield higher V_{oc}'s without loss in I_L.

4.3 Discussion

While the overall performance of nanostructured solar cells is still bounded by the SQ limit, one must consider the built-in optical concentration when applying this theory. Recently an InP nanowire solar cell was found to have a V_{oc} in excess of the record InP planar device [72, 92]. This improvement is likely the result of the built-in optical concentration, which leads to higher carrier densities and hence a higher V_{oc}. Although the best devices to date are $< 14\%$ efficient [57, 61–75], there is great potential for improvement, which could allow nanowire solar cells to exceed 40% solar power efficiency. Here we have shown that besides the possibility of improved carrier collection that has been previously reported [93–95], another key advantage of nanostructured solar cells over planar ones is that the optical concentration is already built-in, yielding the possibility of higher efficiencies than planar devices.

The main limitations for exploiting these concepts in practical devices lie in minimization of non-radiative recombination and achieving appropriate optical design. Minimizing both surface and bulk non-radiative recombination is important for all PV technologies, and great strides have been achieved recently. GaAs has been shown to have an internal luminescence efficiency of $> 99\%$, leading to solar cells that operate in the radiative limit [96, 97], a key requirement for exploiting

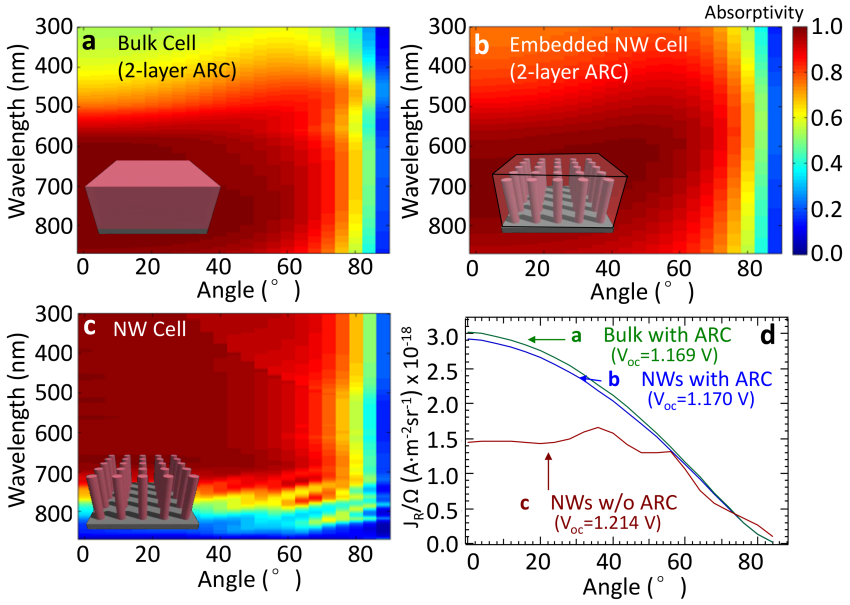

Figure 4.5: Reduced dark current in nanowire structures. Angular dependence of the absorption spectrum for (a) a bulk (80 μm thick) GaAs solar cell, (b) a GaAs nanowire solar cell (embedded in a dielectric) with a period of 300 nm, a radius of 75 nm, and length of 80 μm, and (c) a GaAs nanowire solar cell with a period of 200 nm, a radius of 40 nm, and a length of 2 μm. The devices in (a) and (b) have a double-layer ARC on top, and all cells have a perfect back reflector. The nanowire solar cells have decreased absorption (and hence emission) near the bandedge for angles $> \theta_s$. (d) The current density corresponding to the three structures (a-c) decreases, showing an improved V_{oc} for the nanowire devices.

the concepts discussed in this manuscript. For nanostructured PV, non-radiative recombination is likely dominated by surface recombination. InP has shown excellent promise for nanostructured PV with unpassivated nanowire structures yielding surface recombination velocities as low as 170 cm/s [98, 99]. Finally, implementation of high quality optical structures with the appropriate angular and frequency dependence may be further guided by concepts from metamaterials, metasurfaces,

and transformation optics, which have previously yielded broadband angular selectivity [100, 101].

In conclusion, we have used the principle of detailed balance to determine the maximum efficiency for nanostructured photovoltaic devices. Because the principle of detailed balance requires knowledge of the absorption within the structure rather than the detailed geometry or arrangement, any specific nanostructure (regardless of configuration) will be bounded by this limit. The role of the geometry, period, disorder, etc. are all included by considering the absorption spectrum. The ideal nanostructured devices result in an efficiency of 42%, which is equivalent to the result of Shockley and Queisser when considering full optical concentration. This improvement comes strictly from an improvement of the open-circuit voltage, and not from an improvement in the current. We have assumed that the cell is limited by radiative emission and is under direct illumination in order to achieve the maximum efficiency limit. As with other forms of optical concentration, the efficiency is reduced if part of the incident illumination is diffuse (e.g. if 25% of the incident light is diffuse, the maximum efficiency is reduced to 38%). For future nanostructured devices to take advantage of these benefits, high quality surface passivation and reduced non-radiative recombination are needed. From an optical design point-of-view, nanostructures should be created that have limited absorption for angles and wavelengths that do not match the incident illumination. When this condition is achieved, new high efficiency nanostructured PV devices will be possible.

Chapter 5: Effective bandgap modification and optical concentration

The limiting efficiency for photovoltaic energy conversion based on a semiconductor p-n junction is typically determined using the method of detailed balance put forth by Shockley and Queisser. Here, we describe how this theory is altered in the presence of a photonic structure that is capable of modifying the absorption and emission of photons and optimize a device with optical loss. By incorporating specifically designed photonic structures, higher maximum efficiencies can be achieved for low bandgap materials by restricting the absorption and emission of above bandgap photons. Similarly, restriction of the emission angle leads to increased optical concentration. We consider how both of these effects are modified in the presence of a nonideal photonic structure. Further, we find that the energy of the photonic bandgap that is needed for maximum efficiency depends critically on the reflectivity of the photonic crystal.

5.1 Introduction

In order to calculate the limiting efficiency of a solar cell, Shockley and Queisser developed a formalism that is based on the detailed balance of absorption and emission of photons that occurs at open circuit [5]. In the absence of nonradiative (NR) recombination and with infinite carrier mobility, the maximum efficiency is determined, which depends solely on the material's bandgap. Their method has been further generalized over the years [6, 97, 102–104] and is often the starting point for considering more advanced solar energy conversion processes [58].

Because the maximum conversion efficiency depends solely on the bandgap, it is worthwhile to explore further the connection between the bandgap energy and the efficiency. The semiconductor bandgap is important because it determines both which photons can be absorbed, and at open circuit, which photons must be emitted. Absorption of above bandgap photons gives rise to a current density J_L, which can be withdrawn from the device. Under open-circuit conditions, the cell still absorbs light; however, no current is removed by the external circuit. In order to maintain a detailed balance, radiative recombination leads to a flux of photons out of the cell equal in number to those entering the cell. The emitted flux comes from recombination across the bandgap. Thus, in the ideal case considered by Shockley and Queisser, the bandgap alone is all that is need to describe the absorption and emission processes, which are necessary to determine the conversion efficiency. The modification of the absorption and emission of a cell can lead to spectral shifts and effective bandgap modifications of the device [56, 109, 110]. We previously found

that the introduction of even small amounts of loss in a photonic crystal (PC) that is placed atop a solar cell can result in significant efficiency degradations [56]. In the following analysis, we optimize the photonic bandgap energy depending on PC loss and find that with appropriate bandgap selection, the cell efficiency still improves. For a 90% reflective PC atop a 0.67-eV semiconductor, the unoptimized device yields an efficiency of 15.0%, while the optimized device yields 23.8%.

We also note that this effect is physically distinct from thermophotovoltaic devices where an intermediate structure is thermally isolated from the cell and is used as a modified emitter to effectively change the incident spectrum on the device [105, 106].

5.2 Photonic aspects of detailed balance

In order to modify the semiconductor absorption and emission, we place a PC on top of the structure (see Fig. 5.1), where the PC has a photonic bandgap that extends from the semiconductor bandgap energy E_g^{SC} to the photonic bandgap energy E_g^{PC} (where $E_g^{SC} < E_g^{PC}$). This modification has two effects on the cell. First, J_L is decreased because incident photons with energies between E_g^{SC} and E_g^{PC} will be reflected off the top surface and will not reach the cell. Second, emission from the cell will be similarly limited. Photons that are created by radiative recombination will have energies greater than E_g^{SC} ; however, only photons with energies greater than E_g^{PC} can escape the cell. Thus, photons with energies between E_g^{SC} and E_g^{PC} will be trapped within the cell, unable to escape. These photons can be reabsorbed

by the cell in a process called photon recycling. The continuous absorption and reemission leads to a high concentration of carriers and, hence, an increased open-circuit voltage. Thus, the addition of a PC to the top of the cell leads to a decrease in the current density and an increase in the open-circuit voltage.

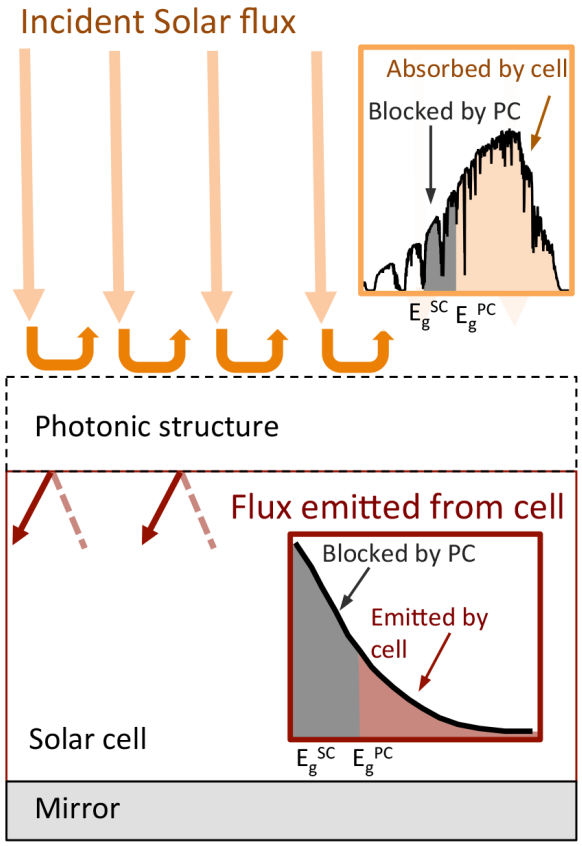

Figure 5.1: PC structure reflects incident light from the sun and traps internally emitted light from the cell. This effect has two consequences. First, there is a decrease in the current due to fewer photons making it into the cell (top). Second, there is an increase in the voltage due to a buildup of the internal luminescence and, hence, carrier concentration because photons emitted near the semiconductor bandgap do not have enough energy to escape and are reflected by the PC (bottom).

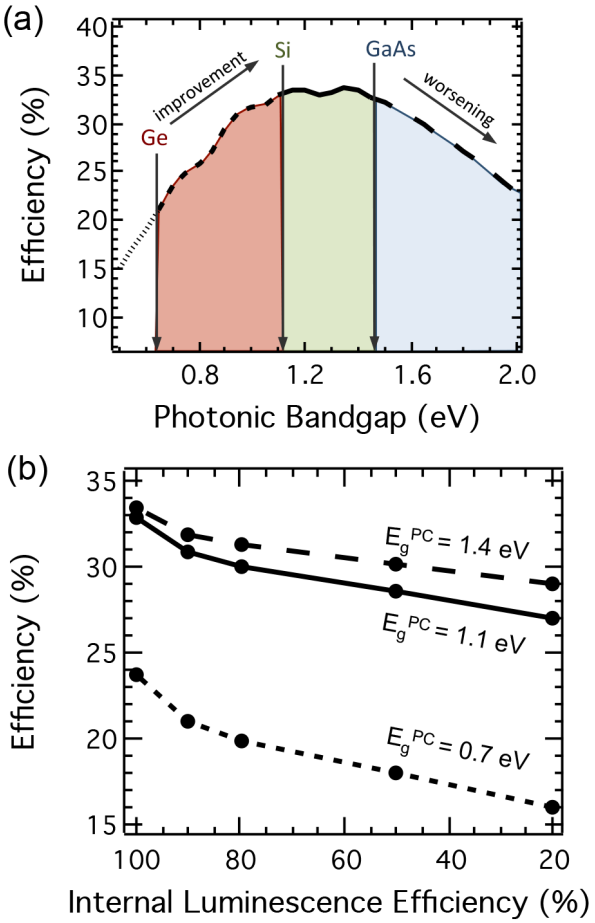

Figure 5.2: Addition of an ideal PC causes the solar cell to behave as although it has a modified semiconductor bandgap energy. (a) PC improves the efficiency of low-bandgap semiconductors but has a detrimental effect on high-bandgap semiconductors. (b) Reduction in the internal luminescence decreases the overall cell efficiency; however, improvements persist for low-bandgap materials.

In order to determine the maximum efficiency, the equations of Shockley and Queisser can be used if the semiconductor bandgap energy is replaced with the photonic bandgap energy (see [56] for details). Fig. 5.2(a) shows this calculation under AM 1.5G illumination, again in the absence of NR recombination. For low

bandgap materials (< 1.1 eV), the addition of a PC improves the efficiency. While for higher bandgap materials (> 1.4 eV), the PC decreases the efficiency. For materials with bandgaps between 1.1 and 1.4 eV, the effects are relatively small. A few typical solar cell materials are shown in Fig. 5.2(a). For a low bandgap material like Ge, the current is high, but the voltage is low. Thus, restricting the absorption and emission allows the device to work at a higher voltage, which leads to an efficiency improvement. For a material like GaAs, there is already a nearly perfect balance between the voltage and current. Improving the voltage, while decreasing the current has a detrimental effect on the device performance [see Fig. 5.2(a)]. We should also note that under ideal conditions, it would appear that $V_{OC} > E_g^{SC}/q$ when $E_g^{PC} \gg E_g^{SC}$. This would suggest that lasing may be possible within the solar cell; however, as we shall see below, the introduction of optical loss reduces the carrier concentrations to levels such that $V_{OC} < E_g^{SC}/q$.

5.3 Effect of loss mechanisms

The total current density in the cell without NR recombination can be written as $J_{tot} = J_L - J_{dark}$, where $J_{dark} = J_0 \left[\exp(qV/k_BT) - 1\right]$,$J_0$ is the reverse-bias saturation current density, q is the electron charge, V is the bias voltage, k_B is Boltzmann's constant, and T is the temperature of the cell. At open circuit, the absorbed solar photons create electron-hole pairs that subsequently recombine and reemit photons (photon recycling). Because only photons within the critical angle of the escape cone will exit the material, there is an intensity buildup within the

semiconductor. The internal fluorescence within the cell is $4n^2/sin^2\theta_e$ larger than the luminescence that escapes [107], where n is the index of refraction of the semiconductor, and θ_e is the emission half angle from the cell, which is usually $\pi/2$. If we allow an additional NR recombination pathway defined by a NR recombination current density J_{NR}, then the internal luminescence efficiency can be written as

$$\eta_{int} = \frac{J_{dark}\,(4n^2/sin\theta_e)}{J_{dark}\,(4n^2/sin\theta_e) + J_{NR}} \tag{5.1}$$

where the total current is now $J_{tot} = J_L - J_{dark} - J_{NR}$. Nonideal internal fluorescence reduces the overall efficiency of the photovoltaic device [see Fig. 5.2(b)]; however, the PC is still able to improve the efficiency of a low-bandgap semiconductor. As depicted in Fig. 5.2(b), even for low internal fluorescence, an ideal PC can improve the efficiency of a 0.7-eV bandgap material by $\sim 13\%$ in absolute efficiency.

A very high quality photonic material is important to realize the aforementioned efficiency improvements. As an example, we consider a material with $E_g^{SC} =$ 0.67 eV covered by a PC with reflectivity R and a photonic bandgap from E_g^{SC} to E_g^{PC} . $R = 90\%$ means that 90% of the incident photons over the energy range from E_g^{SC} to E_g^{PC} will be reflected from the cell, and 90% of the internal luminescence that would typically escape will be trapped within the cell. Fig. 5.3 shows that the largest efficiency gains are achieved with $R \geq 90\%$. Similarly, for $R < 100\%$, the E_g^{PC} required for maximum efficiency reduces rapidly with decreasing R (see Table I).

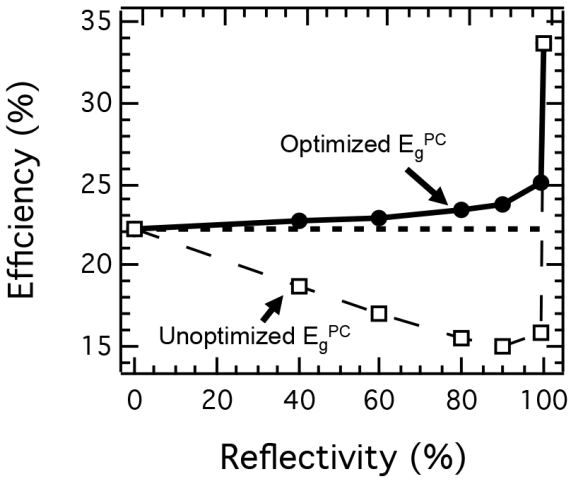

Figure 5.3: Highly reflective PC is needed for significant improvement of the cell efficiency.

Table I. Optimized E_g^{PC} for maximum efficiency given R and $E_g^{SC} = 0.67$ eV

$E_g^{SC}(eV)$	R(%)	Optimized E_g^{PC}(eV)	η(%)
0.67	- -	- -	22.3
0.67	100	1.37	33.6
0.67	99	0.79	25.1
0.67	90	0.73	23.8
0.67	80	0.72	23.4
0.67	40	0.71	22.7

Effect of nonideal PCs. The photonic bandgap energy necessary for highest photovoltaic efficiency depends on the reflectivity of the PC. R = 100% corresponds to an ideal PC that reflects all incident light that exists within the photonic bandgap. The top row corresponds to the reference cell with no PC.

The current-voltage characteristic of a cell clearly demonstrates the decrease in current and the increase in voltage upon the addition of a PC. The PC reduces the maximum current by limiting absorption, but the overall cell performance improves because of an increase in the open-circuit voltage. Fig. 5.4 shows this effect for a solar cell made from a material with a bandgap energy of 0.67 eV (e.g., Ge)

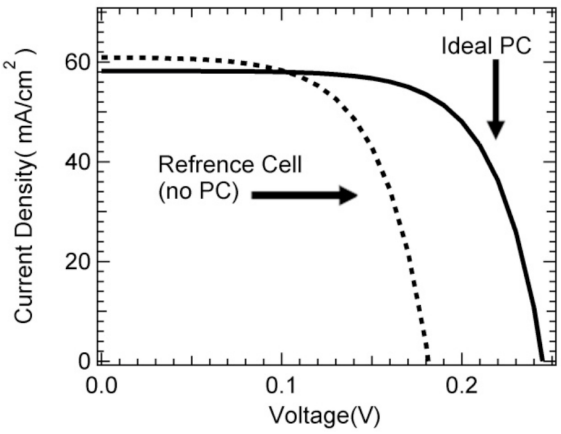

Figure 5.4: Current-voltage characteristic of a $E_g^{SC} = 0.67$ eV solar cell with (solid line) and without (dotted line) a PC. The addition of a PC increases the open-circuit voltage but decreases the short-circuit current density.

and$\eta_{int} = 0.1\%$. The addition of an ideal PC with energy bandgap from 0.67 to 0.74 eV results in a 2.9% absolute efficiency gain. Even with realistic material parameters, efficiency gains of several percent are possible. As an example, a solar cell's efficiency improves by 2.0% absolute for a PC with R = 90% compared with no PC. Table II shows the relevant cell parameters.

Table II. Device parameters for a $E_g^{SC} = 0.67$ eV solar cell

	$R(\%)$	$J_{sc}(mA/cm^2)$	$V_{oc}(V)$	$\eta(\%)$
Reference Cell	–	61.0	0.182	6.84
Ideal PC	100	58.2	0.245	9.75
PC	90	58.5	0.226	8.80

The photonic crystal reduces the short circuit current, increase the open circuit voltage, and increase the energy conversion efficiency.

5.4 Emission angle restriction with optical losses

It is well known that the emission solid angle plays an important role in determining the cell's V_{OC} [6, 84, 85, 111–114]. In fact, the improvement in the V_{OC} due to restricting the emission angle is comparable with the improvement in the V_{OC} due to light concentration. In both cases, the voltage improvement is caused by an increase of the carrier densities. When the emission half angle θ_e is limited to that of the sun's half-angle $\theta_s = 0.267°$, the efficiency reaches that of 46 000 suns concentration.

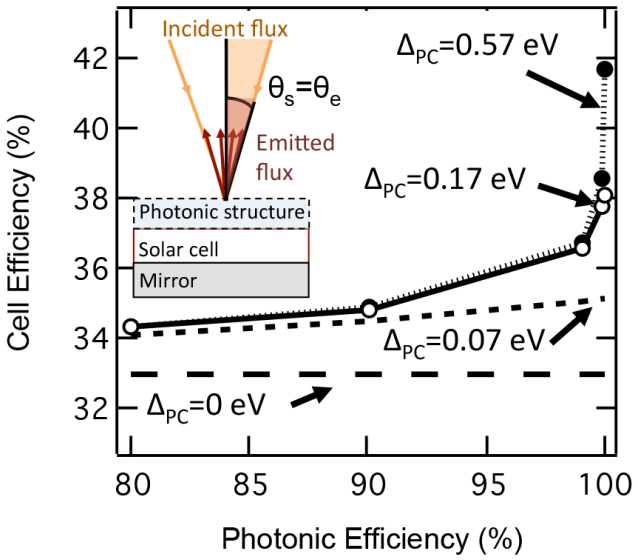

Figure 5.5: Large efficiency enhancements are achieved for relative small bandwidth ΔPC photonic structures. However, these structures need a high photonic efficiency. Inset: A photonic structure is used to reduce the emission half-angle from the cell, which is typically 90°, to that of the sun, $\theta_s = 0.267°$.

The main limitation on emission angle restriction is generally thought to be

due to NR recombination [6]. However, highquality GaAs is thought to have an internal florescence yield of 99.7% [96], making it an excellent material choice. A GaAs solar cell that has a fully restricted emission angle may be able to achieve efficiencies>40% under 1 sun illumination if a photonic structure can be designed that is capable of fully restricting the emission of all photons. It is also known that PC structures can be used to modify the outcoupling of light in LEDs through a modification of the spontaneous emission radiation pattern [108], which could be useful for experimental realization.

Two important parameters that must be considered for emission angle restriction using realistic photonic structures are the bandwidth of the photonic structure ΔPC and the photonic efficiency, η_{ph} , i.e., the fraction of photons that are restricted in their emission angle compared with the total number of photons that are emitted. If angle restriction is only possible over a range of wavelengths or $\eta_{ph} \neq 100\%$, then the overall cell efficiency enhancement will be decreased (see Fig. 5.5).

Only a relatively small bandwidth is needed for significant efficiency improvement. A photonic structure with a bandwidth of only $\Delta PC = 170$ meV yields a $\sim 3\%$ absolute efficiency improvement for $\eta_{ph} = 100\%$, and a structure with $\Delta PC = 570$ meV yields an efficiency $> 40\%$. However, when $\eta_{ph} \neq 100\%$, the maximum achievable efficiency is significantly lower. While a perfect photonic structure could allow for a solar conversion efficiency of near 42%, a photonic structure with $\eta_{ph} = 99\%$ results in a solar conversion efficiency below 37%. Thus, the development of extremely high-quality photonic structures is necessary.

Finally, we note the importance of high internal fluorescence yield. Fig. 5.6

shows the current-voltage characteristic for a semiconductor with E_g^{SC} =1.43 eV and $\eta_{int} = 99.7\%$ (e.g., highquality GaAs) that is fully angle restricted ($\theta_e = \theta_s$ and $\eta_{ph} = 100\%$,). For this case, an absolute efficiency enhancement of 1.7% is found.

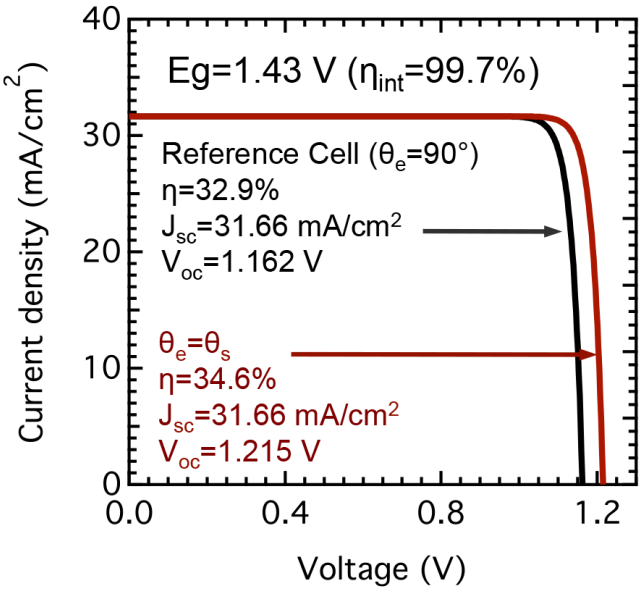

Figure 5.6: Current-voltage characteristic of a solar cell with $E_g^{SC} = 1.43$ eV and $\eta_{int} = 99.7\%$. The addition of a photonic structure to reduce the emission angle has no effect on the short-circuit current but improves the open-circuit voltage.

5.5 Conclusion

We have shown a degree of freedom in a solar cell design by incorporating photonic structures that are constructed to restrict photon absorption and emission. Nonideal reflectivity and NR recombination are considered and found to play an important role in determining the maximum achievable efficiency. Such structures are capable of improving efficiencies by several percent when realistic material

parameters are used. In addition to high-quality photovoltaic materials, the quality of the photonic structures is equally important. This leads us to emphasize the importance of developing new photonic structures for photovoltaics.

Chapter 6: All-photonic semiconductor bandgap engineering through photon-recycling

Optoelectronic devices are the backbone of today's high tech industry, where different semiconductors are used to perform different functionalities. Wide-bandgap materials (e.g. SiC and GaN) are often used for power electronics, having bandgaps > 2 eV; while lower bandgap materials (e.g. Si and GaAs) are usually used for photodetectors, solar cells, diodes, and integrated circuits. In order to achieve light absorption or emission at different wavelengths, different atoms are typically required to create a new lattice with a different semiconductor bandgap. Here we show that the semiconductor bandgap of a material need not be an intrinsic property of that material but can be changed through photonic structuring of the surrounding layers. GaAs has a natural bandgap of 1.43 eV; however, we show that optical reflectors can be used to induce photon-recycling effects, which results in a bandgap shift of up to 0.13 eV. When a p-n junction is created within the GaAs, we find that its electrical properties are also shifted resulting in an $11.3 \pm 3.7\%$reduction in the radiative part of dark current and a 1.71 ± 0.24 mV improvement in the open-circuit voltage of the device under 0.6 sun's equivalent illumination. These results show that both the optical and electrical properties of a semiconductor can

be modified purely by photonic manipulation, which enables a fundamentally new method for designer semiconductor structures and device. We anticipate that our result will enable a range of optoelectronic devices including light emitting diodes, phototransistors, and optical isolators.

6.1 Introduction

The bandgap of a semiconductor is usually thought to be an intrinsic property of the material, which results from the arrangement of atoms of a particular type within the lattice [115]. The semiconductor bandgap plays an important role in optoelectronic devices, where photons with energy in excess of the bandgap energy are absorbed, resulting in carrier generation. Similarly, radiative recombination of carriers results in light emission near the bandgap energy. Methods to engineer the semiconductor bandgap typically require a modification of the atomic species or stoichiometry (e.g. by molecular beam epitaxy [116, 117], quantum confinement [118,119], or induced lattice strain [120–123]. However, all of these methods require the mechanical manipulation of the lattice. In this chapter, we show that the semiconductor bandgap can be modified purely by photonic structuring, rather than atomic rearrangement. This concept relies on the trapping of emitted light from the semiconductor using frequency selective mirrors and recycling the emission to create additional carriers. These carriers, in turn, increase the quasi-Fermi level splitting between electrons and holes compared to the case when no selective reflectors are in place. Optically, we observe a shift in both the absorption and emission wavelengths, and electrically, we measure a reduction in the dark current of a p-n junction. Finally, we show that this concept can be used to improve the performance of a solar cell by increasing its open-circuit voltage.

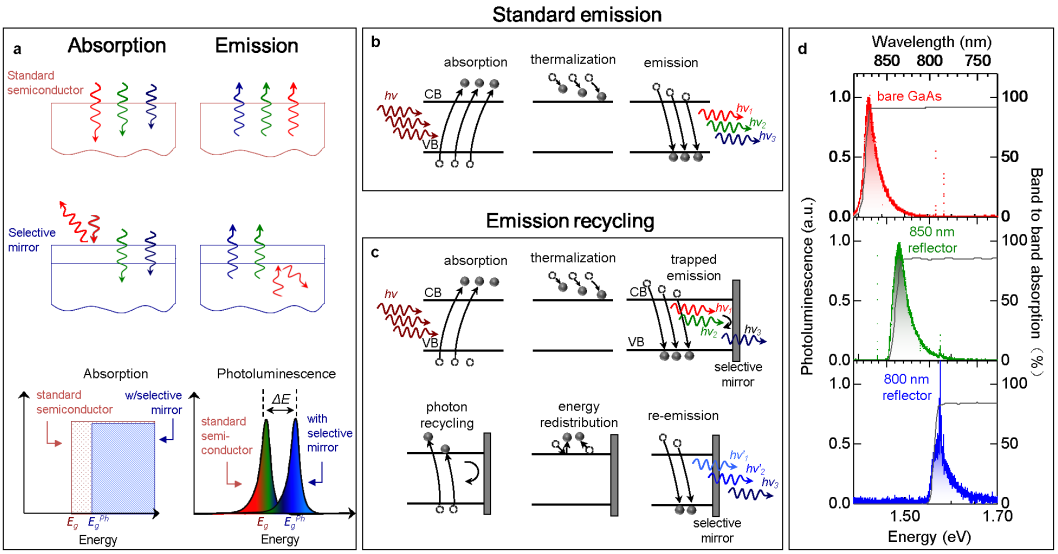

Figure 6.1: A photonic approach to semiconductor bandgap engineering. (a) A standard semiconductor absorbs photons with energy in excess of the semiconductor bandgap, and the recombining carriers result in emission near the semiconductor bandgap energy, E_g. The addition of a wavelength selective mirror, blocks certain wavelengths of light from both entering and exiting the semiconductor, resulting in absorption only above the photonic bandgap of the mirror, E_g^{ph}, and emission near the photonic bandgap. (b) For a standard semiconductor, absorption results in carrier generation, followed both thermalization to the band-edge, and subsequent photon emission, with a spectrum peaked near the semiconductor bandgap. (c) The addition of a selective mirror causes light that would traditionally be emitted to be trapped and reabsorbed (photon recycling). The newly generated carriers exchange energy with other carriers in the conduction band, and recombination and photon emission occurs again. Only photons emitted with an energy above the photonic bandgap energy of the mirror will escape to be detected. (d) Experiments show that a GaAs wafer can have both its absorption and emission shifted upon the addition of a wavelength selective mirror.

6.2 Wavelength dependent absorption and photoluminescence

The semiconductor bandgap of a material can be determined from measurements of its wavelength dependent absorption and photoluminescence; however, the addition of a wavelength dependent reflector can modify both absorption and emission (Fig. 6.1(a)). A semiconductor will normally absorb incident light above its bandgap, generating carriers. These carriers quickly thermalize (within picoseconds to nanoseconds) with the lattice and each other before finally recombining to generate photons with energy near the semiconductor bandgap energy (Fig. 6.1(b)). When a selective reflector is added to the top of the semiconductor, the emission is reflected back and reabsorbed, resulting in photon (emission) recycling (Fig. 6.1(c)). The reabsorbed photons generate new carriers that interact with the lattice and the other carriers. This interaction results in a redistribution of the energy before carrier recombination yields secondary photon emission. Only photons emitted with an energy higher than the cut-off energy for the selective reflector will escape, resulting in photoluminescent emission. The photons that are not emitted will be reabsorbed and continue the recycling process until either a photon is generated with enough energy to pass through the reflector, get absorbed in a region of the sample where no carriers are generated, or the generated carriers recombine non-radiatively.

Experiments were conducted using a GaAs solar cell (M-Comm) and three selective reflectors to show the shift of the semiconductor bandgap based on absorption and photoluminescence measurements (Fig. 6.1(d)). The absorption was measured using an integrating sphere setup in combination with photoluminescence to ensure

that all measured absorption near the band-edge resulted in carrier generation rather than parasitic absorption [124, 125]. At low temperatures, the photoluminescence spectrum is well described by a single Gaussian distribution, while at higher temperatures, the spectrum is more accurately described by a sum of Gaussian peaks representing a distribution of states within the bands [126]. For the GaAs device without any reflectors, a fit of the photoluminescence spectrum yields a bandgap of 1.424 eV (872.45 nm), as expected for GaAs at room temperature, which also corresponds to the onset of band-to-band absorption (Fig. 6.1(d)). The addition of a short-pass selective reflector with cut-off wavelength $\lambda_{cut-off} = 850$ nm results in a shift of the absorption onset within the GaAs as a result of photon reflection for $\lambda_{cut-off} > 850$ nm. Thus, while the GaAs device alone is able to absorb photons in the range 850 - 872.45 nm, the combined structure (GaAs plus reflector) is not. Similarly, there is a shift of the photoluminescence, which implies a new bandgap energy for the device of 1.462 eV (849.8 nm). When a short-pass reflector with $\lambda_{cut-off} = 800$ nm is used, a bandgap energy of 1.553 eV (800.0 nm) is found.

The photoluminescence spectrum not only indicates the energy of newly formed bandgap, but its absolute intensity shows that the carriers have a higher average energy when the reflector is used – indicating a true modification of the electronic response. In the absence of emission recycling, the energy dependent photoluminescence for the devices with the reflectors would never surpass that of the standalone GaAs device. However, through emission recycling, the average energy of the carriers is increased and the photoluminescence intensity of the device with reflectors is higher than the GaAs alone (Fig. 6.2).

A micro-photoluminescence system is used to determine the calibrated photoluminescence (Fig. 6.2(a)). A 660 nm wavelength diode laser is used to excited carriers within the GaAs, and the photoluminescence is collected by an objective (100X magnification, NA = 0.7), which is subsequently sent to a CCD camera and spectrometer (Fig. 6.2(a)). The reflectors enhance photon recycling for light emitted with wavelengths between the cut-off wavelength of the reflector and the original band edge of the GaAs (i.e. for all emitted photons that can be reflected back into the GaAs). These photons serve as a secondary source of illumination, which create additional carriers and lead to a higher free carrier density within the device. The higher density leads to an increase in PL intensity for photons with energy above reflectors' cut-off energy. Because the internal fluorescence yield η_{int} of our device is less than 100% ($\sim$ 83%), repeated recycling has diminishing returns, limiting the total possible bandgap shift. Figure 6.2(b), shows that the calibrated photoluminescence for high energy photons can be increased with the addition of the reflectors. Because the measured photoluminescence intensity depends on the laser power density and beam size, which are modified when the reflector is placed on top of the device, these parameters are measured and used to calibrate the photoluminescence intensity.

In addition to the optical detection of a bandgap modification, the semiconductor's electronic properties are also modified. As the bandgap of a semiconductor is increased, its dark current is diminished as a result of reduced radiative recombination. The band-to-band recombination rate in a semiconductor is given by $R_{bb} = Bpn$, where n and p are the electron and hole concentrations, respectively, and B is the

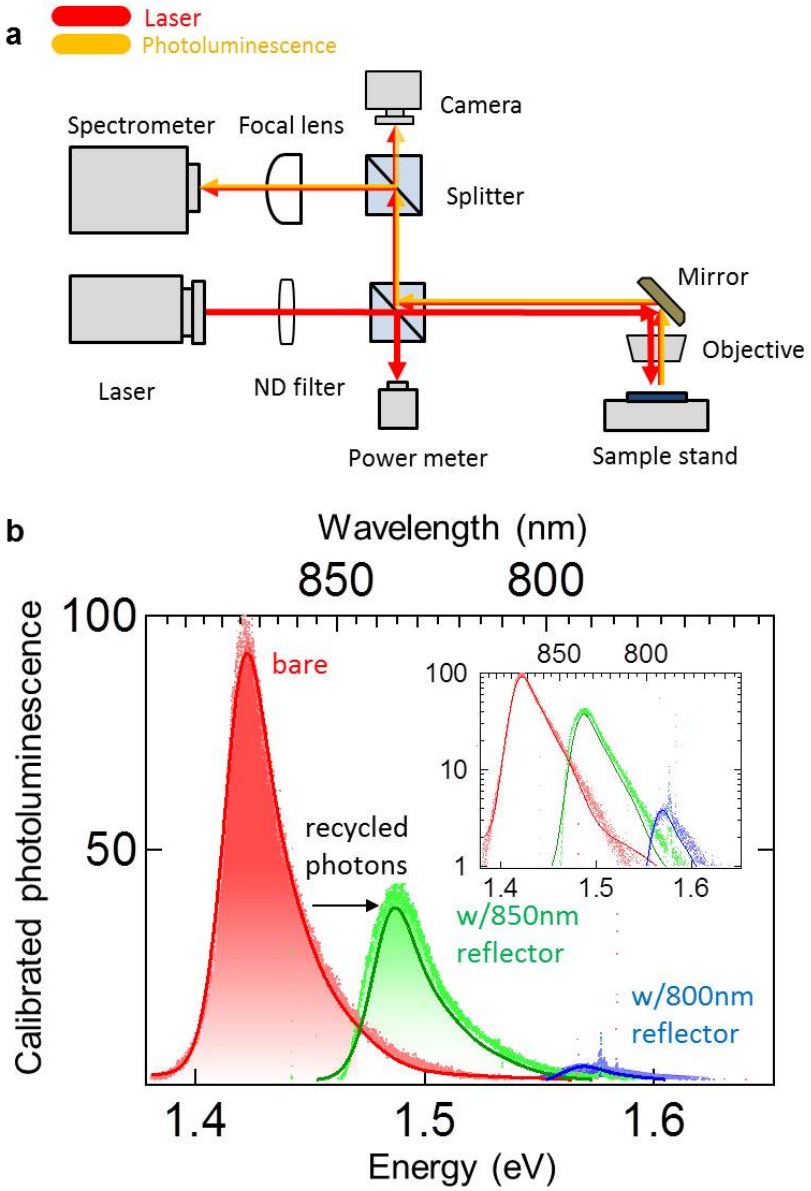

Figure 6.2: Photoluminescence measurements show energy transferred through photon recycling. (a) Schematic of micro-photoluminescence measurements. (b) Calibrated photoluminescence measurements show that the emission that occurs when the reflectors are used has more higher energy photons than the emission of the bare semiconductor. The increased photon flux at higher energies is a result of energy transfer between excited carriers facilitated by photon recycling.

radiative recombination coefficient, which depends on the absorptivity, and hence the semiconductor bandgap [127, 128]. As the semiconductor bandgap increases, the radiative rate decreases, as does the saturation current density, $J_0 = qR_{bb}$. The current-voltage characteristic for a simple p-n junction in the dark can be described by a two-diode model [86, 129]:

$$J_{dark}(V) = J_1\left(e^{\frac{q[V-J_{dark}(V)R_s]}{k_BT}} - 1\right) + J_2\left(e^{\frac{q[V-J_{dark}(V)R_s]}{nk_BT}} - 1\right) + \frac{V - J_{dark}(V)R_s}{R_{shunt}} \tag{6.1}$$

where V is the applied voltage, J_1 is the dark current density component corresponding to a diode ideality factor of one (primarily due to radiative recombination in a high-quality device), J_2 is the current density component that corresponds to an ideality factor of $n = 2$ (primarily non-radiative recombination within the junction under low level injection), k_B is the Boltzmann constant, T is the room temperature, q is the electron charge, R_s is the series resistance and R_{shunt} is the shunt resistance [9, 11, 12, 86]. Thus, if the filters are used to increase the semiconductor bandgap, they will also cause a reduction in the dark current component corresponding to radiative recombination.

6.3 Current-voltage characteristics under dark and light conditions

To experimentally determine the effect of a bandgap modification on the optoelectronic response of a device, we measured the dark current characteristics of a GaAs p-n junction device with and without the wavelength-selective optical reflec-

tors. The reflectors are placed atop the cell ($\sim$ 1.5 mm away from the sample to avoid the influence on top contact). To avoid systematic artifacts, the reflectors are placed atop the device in a random order for each applied voltage, and the resulting current is measured. To minimize the noise induced by the ambient surroundings (e.g. temperature fluctuations and electromagnetic noise), the current is recorded for 100 s for each reflector (and for the bare sample), and the resulting 20 data points are average before the next voltage setting. Note: the placement of a glass slide on top of the device instead of a reflector had negligible effect on the dark current.

The experimental dark current measurements were fit to the two-diode model (Equation 6.1) in the high voltage region (from 0.6 V to 1.05 V), where radiative emission contributes most to the dark current. As is shown in Figure 6.3(a), the model represents the experimental data well at higher voltages, where radiative emission plays a significant role in the optoelectronic behavior, but begins to deviate at lower voltages, where the recombination in the junction begins to dominate. The current-voltage characteristics are used to determine the diode parameters for a device with and without the different optical reflectors, and the only parameter that significantly changed was the dark current density component corresponding to radiative recombination, J_1, which was reduced with the addition of the reflectors (Fig. 6.3(b)). Further, the reduction in the dark current is most significant for reflectors with a higher energy cut-off, corresponding to increased effective energy bandgap. Finally, as the distance between the reflector and the device is increased, the photon recycling is reduced as more photons escape the device (Fig. 6.3(c)).

This behavior can be explained by a simple geometric model where the emitted photons at a higher emission angle (relative to the surface normal) are less likely to be reflected back into the device. As a result, as the spacing between the reflector and the device approaches 1 cm, the dark current for all devices approaches the same value.

To understand how this photonic approach to semiconductor bandgap shifting influences the performance of solar cells, we analyze the variation of the open-circuit voltage caused by a change in the cells' emission wavelength through the addition of a photonic reflector. For an ideal solar cell, the open-circuit voltage is given by:

$$V_{oc} = \frac{k_B T}{q} \ln\left(\frac{J_L}{J_{dark}} + 1\right) \tag{6.2}$$

where J_L is the light generated current. If the dark current near V_{oc} is dominated by radiative emission, the dark current can be suppressed using the wavelength selective reflectors. To determine the shift in V_{oc}, we keep J_L fixed to ensure that any changes in V_{oc} are due to the reduction in the dark current and not a result of changes in J_L due to the reflectors response at shorter wavelengths modifying J_L. Figure 6.4 shows the I-V characteristics for four devices: the bare solar cell and the solar cells with three different reflectors with cut-off wavelengths of 850 nm, 800 nm, and 750 nm. After applying the photonic reflectors, the open-circuit voltage increases by 1.51 ± 0.25,1.59 ± 0.30 and 1.71 ± 0.24 mV, as is shown in Fig. 6.4(b). Because the enhancement comes from the decrease in dark current, the shorter cut-off wavelength of reflector enables more photon recycling and hence a higher open-circuit voltage. This enables the sample with 750 nm reflector to

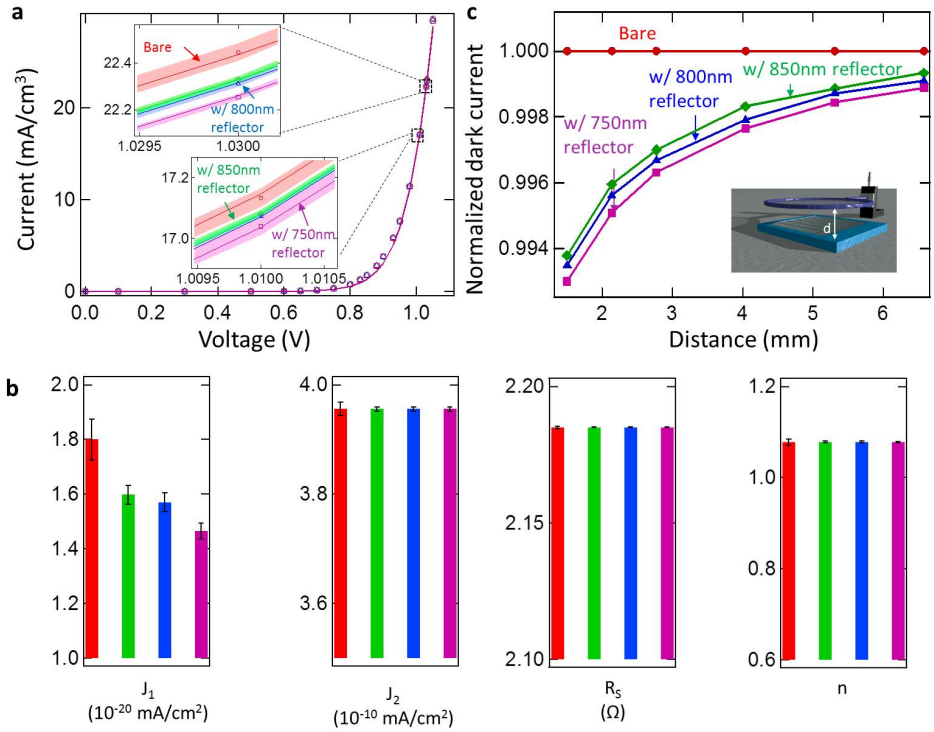

Figure 6.3: Optical modification of the dark current. (a) Dark I-V measurement for a bare GaAs p-n junction device (red circle) and the same device with the addition of a wavelength selective reflector with cut-off wavelengths of 850 nm (green diamond), 800 nm (blue triangle) and 750 nm (purple square). The solid lines correspond to the fitting of two-diode model of the GaAs devices with and without reflectors. The shadowed areas correspond to three standard deviations of the data from the mean. (b) Most fitting parameters for two-diode model remain unchanged upon the addition of the reflectors; however, J_1, which corresponds to the dark current component related to radiative recombination, is reduce when the reflectors are used. The error bars correspond to three standard deviations of the data from the mean. (c) As the reflectors are vertically displaced from the device, the photon recycling is reduced and the dark current tends toward its value without the reflector.

have the highest open-circuit voltage. I-V measurements were performed 50 times on different days to show the robustness of the measurements and minimize the influence of thermal variations or other fluctuations on short-circuit current density. In all measurements, the V_{oc} is enhanced by $1-2$ mV with the addition of the reflector. Further enhancement in the V_{oc} is expected for devices with higher internal fluorescence yield, (e.g. a cell with an internal fluorescence yield of 99.7%, the improvement of the open−circuit voltage using the 750 nm reflector would be 4.6 mV).

6.4 Conclusion

In conclusion, we have shown that photon recycling can be used to effectively modify the semiconductor energy bandgap through photonic structuring. This effect enables the tuning of the energy bandgap of a semiconductor without rearranging the atoms in the lattice. We have observed a shift in the optical (absorption and emission) and electrical (dark current) response and have applied this concept to a solar cell to improve its open-circuit voltage. Future work with high internal fluorescence yield semiconductors will enhance the effect and may find uses in many optoelectronic devices.

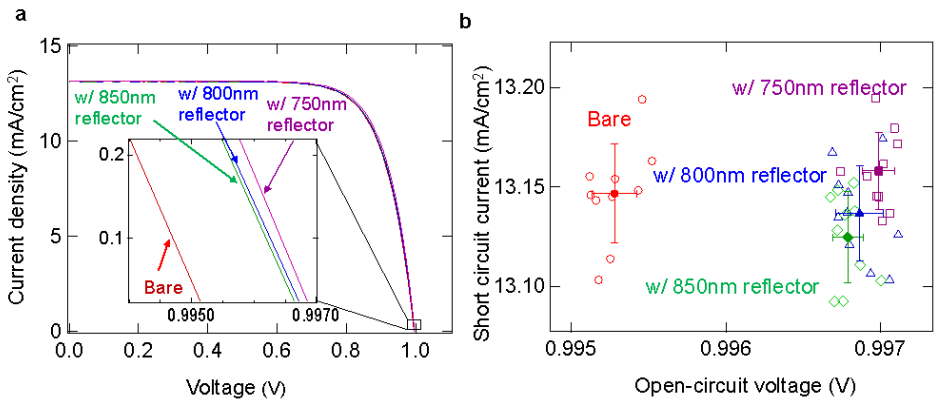

Figure 6.4: Measured improvement of the open-circuit voltage of a GaAs solar cell. (a) I-V measurements under a solar simulator with a spectrum corresponding to the AM 1.5G spectrum with an intensity of $\sim$ 0.6 suns. Data are the average of 10 measurements for each the bare GaAs (red) and GaAs with reflectors with cut-off wavelengths of 850 nm (green), 800 nm (blue), and 750 nm (purple). (b) Open-circuit voltage and short circuit-current for different current-voltage runs. For similar short-circuit current densities, the open-circuit voltage is increased by 1.51 ± 0.25, 1.59 ± 0.30 and 1.71 ± 0.24 mV for the solar cell containing reflectors with cut-off wavelengths of 850 nm (green), 800 nm (blue), and 750 nm (purple), respectively. The error bars represent the standard deviation of the measured mean.

Chapter 7: Improved voltage response based on engineered spontaneous emission

In order to obtain a high photovoltaic (PV) efficiency, a solar cell must operate at both a high current and voltage. The current is determined by the semiconductor's ability to convert above-bandgap photons into electron-hole pairs that can be collected, while the maximum achievable voltage depends on maximizing the carrier densities and minimizing recombination within the cell. For a high quality semiconductor like GaAs, which has been shown to have an internal fluorescence yield of 99.7%, non-radiative recombination can be minimized to the point where the PV efficiency is limited by radiative emission from the cell. Here we show an improvement in output voltage and efficiency by engineering the spontaneous emission rate using photonic crystal structures. The proposed device is composed of a GaAs PV cell that has been nano-patterned with photonic crystals in order to control carrier spontaneous emission and, as a result, increase device output voltage. In the proposed device, this emission control is achieved by tuning the bandgap of the photonic crystal structure near the semiconductor band edge. Under these operating conditions, the open circuit voltage is increased by a factor of $-\frac{k_B T}{q} \ln [F_p]$, where F_p is defined as the ratio of the spontaneous emission rate in the nanopatterned solar cell to the

spontaneous emission rate in bulk GaAs. By engineering small F_p the voltage of the device can be significantly improved, leading to photovoltaic efficiencies of $\sim$ 36% from a single junction device.

7.1 Introduction

The development of advanced photovoltaic technologies is critical to reducing the cost per watt of alternative energy. Currently only $\sim$ 10% of the US energy production comes from renewables (including hydropower and biomass) and only <0.1% is from solar. Recently the National Renewable Laboratory (NREL) released a study suggesting that by 2050 nearly 80% of the power in the US could be generated by renewable sources, while keeping the grid stable. However, to achieve target, solar generation needs to increase to cover $>$ 10% of energy production.

In order to make solar photovoltaics cost competitive with fossil fuel based technologies, it is crucial to reduce inefficiencies that limit the solar power conversion. For a material with a given bandgap energy, the short-circuit current is limited by the cell's ability to absorb above bandgap energy photons, and the open-circuit voltage is limited by the bandgap energy. The efficiency of the solar cell is proportional to the product of these two quantities. Therefore, it is essential to maximize them simultaneously in order to achieve the optimal solar cell efficiency determined by the Shockley-Queisser limit. For the short circuit current, experimentally measured values are already very close to their fundamental limit. However, the experimentally achieved open-circuit voltages still fall 300-400 mV below the funda-

mental limit imposed by the semiconductor bandgap due to spontaneous emission related losses. In solar cells limited by radiative recombination, such as GaAs, the open-circuit voltage can be improved by modifying spontaneous emission. Thus, it is possible to achieve significant increase in solar cell efficiency by understanding and engineering carrier spontaneous emission.

Here we describe a new type of photovoltaic structure, which achieves enhanced solar cell efficiency by reducing spontaneous emission using photonic crystal structures (Fig. 7.1). Photonic crystals are materials with a periodic index of refraction. These materials can strongly modify the spontaneous emission rate by altering the local density of states of the electromagnetic field [130–133]. In particular, photonic crystals exhibit a photonic energy bandgap, which is a spectral band where the density of states vanishes. In this spectral band, spontaneous emission is strongly suppressed [132]. By aligning the photonic bandgap of the photonic crystal structure with the electronic bandgap of the solar cell material, it becomes possible to reduce spontaneous emission and hence improve the electronic, photovoltaic efficiency of the device. Our strategy differs significantly from previous photonic approaches, which have focused almost exclusively on using photonic structures to increase the probability of absorption. Here, we show a modification of the electronic properties of the carriers by engineering the photonic properties of the solar cells-a concept that has not been investigated yet for improving photovoltaic performance. We have performed a theoretical analysis of this approach and estimate that by using a spontaneous emission suppression factor of only 10, a single junction device that is limited by Auger recombination can achieve nearly 35% power conversion

efficiency under 1 - sun illumination.

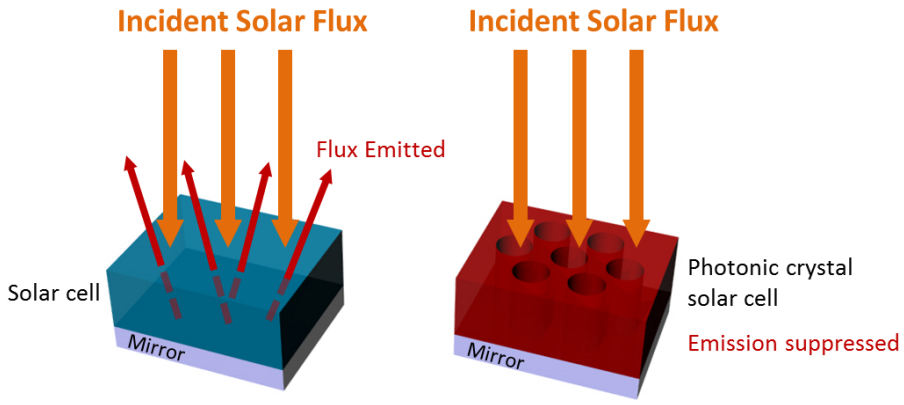

Figure 7.1: Schematic of emission suppression using a photonic crystal based solar cell. A traditional cell emits photons at energies near the semiconductor bandgap energy, which reduces its open circuit voltage (left). A photonic crystal is used to suppress emission (right), which will allow the V_{oc} to increase beyond that of the traditional Shockley-Queisser formulation.

For solar cells made of high quality materials, like GaAs, one must go beyond device physics models, which ignore certain aspects of the energy conversion process. Specifically, device models typically ignore photon recycling, i.e. the re-emission of photons from recombining electron-hole pairs; however, this phenomenon is very important to the understanding of solar cells. By taking advantage of photon recycling effects, the efficiency of a solar cell can be improved by several percent, a fact which was recently demonstrated in the current single junction record efficiency cell. A simple device model would not have predicted this improvement and is thus inadequate for describing a new class of high efficiency solar cells. In addition to simple optical management of recycled photons, e.g. using a back reflector as de-

picted in Fig. 7.2(b), the rate at which the recombination occurs is of even greater importance. By slowing down the recombination rate, carrier densities are elevated, and hence the open circuit voltage increases. Figure 7.2 shows how optical management of recycled photons can lead to an efficiency improvement (a and b) but that suppression of recombination leads to a significantly larger improvement in the power conversion efficiency (Fig. 7.2(c)).

7.2 The standard solar cell

In order to take into account recycled photons, we use a thermodynamic model, as Shockley and Queisser did [5], to determine the ultimate limiting efficiency of a solar cell. Under illumination, there is a balance between the incoming solar flux, the outgoing flux due to radiative recombination, photons removed from the system by non-radiative (NR) recombination, and photons removed via charge excitation that generates current. The rate equation is then:

$$\frac{J}{q} = N_{absorbed} - N_{existing} = \gamma_{in} - \gamma^0_{emit} \tag{7.1}$$

where J is the total current density drawn from the device, q is the unit charge, γ_{in} is the absorbed incident flux from the sun,

γ^0_{emit} is the flux emitted from the cell, and γ^0_{NR} is the flux that is lost from intrinsic non-radiative recombination. At open circuit conditions, the total current is zero and the rate equation becomes:

$$\gamma_{in} = \gamma^0_{emit} + \gamma^0_{NR} \tag{7.2}$$

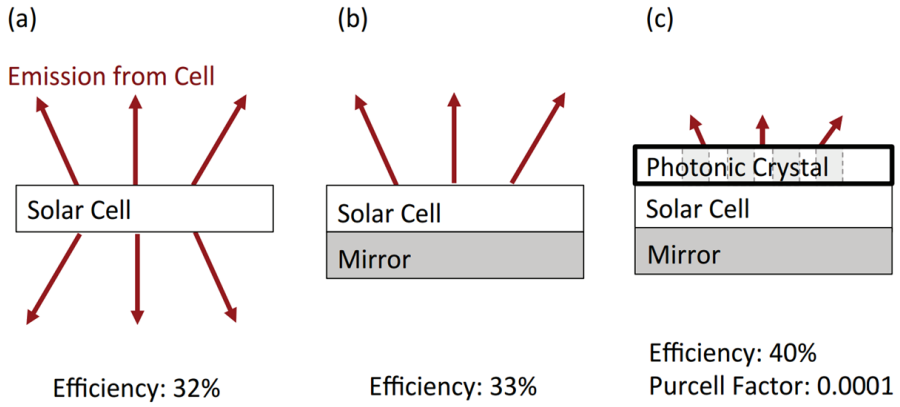

Figure 7.2: Spontaneous emission limits the maximum achievable carrier concentration and hence operating voltage of a cell. (a) For a typical solar cell either on an index matched substrate or in air, radiative emission results in photons exiting the cell from both sides. (b) The addition of a back reflector limits emission out of the back of the cell and leads to a modest improvement of carrier density and the efficiency. (c) The addition of a photonic structure yielding a Purcell factor of 0.0001 leads to an ideal solar conversion efficiency of 40% under 1 - sun illumination by significantly suppressing emission.

or in terms of the external luminescence efficiency,

$$\gamma_{in} = \gamma^0_{emit}/\eta^0_{ext} \tag{7.3}$$

where

$$\eta^0_{ext} = \frac{\gamma^0_{emit}}{\gamma^0_{emit} + \gamma^0_{NR}} \tag{7.4}$$

and $q\gamma^0_{emit}$ is the minimum dark current allowed by thermodynamics, which is determined from the theory of detailed balance. Eq. [7.3] then yields the standard diode J-V characteristic:

$$J_L = J_0 \frac{\left(e^{\frac{qV_{oc}}{k_B T}} - 1\right)}{\eta^0_{ext}} \tag{7.5}$$

where J_L is the light generated current and J_0 is the reverse saturation current (related to γ^0_{emit}). Solving for the open circuit voltage, V_{oc}, we obtain

$$V_{oc} \approx \frac{k_B T}{q} \ln\left(\frac{J_L}{J_0}\right) + \frac{k_B T}{q} \ln\left(\eta_{ext}^0\right) \tag{7.6}$$

The first term corresponds to the max V_{oc}, and the second term describes how the V_{oc} is reduced for imperfect external luminescence efficiency [134]. J_0, and hence the emission rate, depends on the emissivity, absorption, and geometry, which determines how the photons exit the sample (see also Fig. 7.2(a), (b)). The dielectric environment surrounding the cell will effect its emission and hence V_{oc} and efficiency [6].

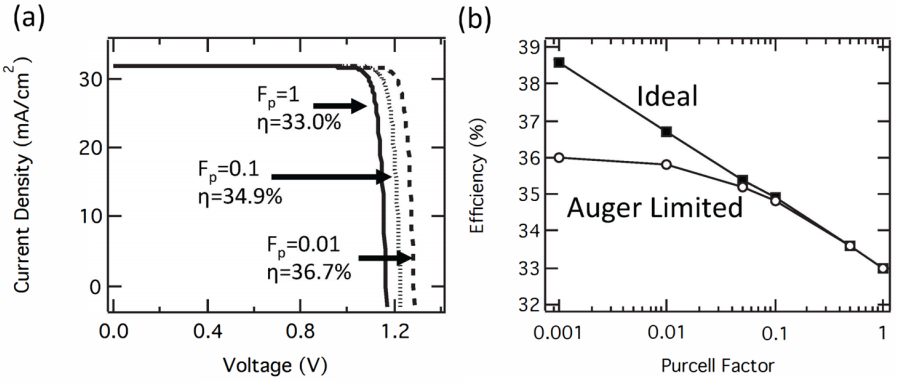

Figure 7.3: (a) Current-voltage characteristic for an ideal GaAs solar cell with three different values of the Purcell factor. A Purcell factor of $F_p = 1$ corresponds to no suppression of the radiative rate. $F_p < 1$ leads to a voltage increase and hence an improvement of the cell's power conversion efficiency. (b) For a solar cell that is limited by Auger recombination, the limiting efficiency is $\sim 36\%$ for reasonable values of F_p.

7.3 Purcell effect on a solar cell

The spontaneous emission rate of the emitters within a solar cell can be altered by modifying the density of optical states that the emitter (in this case, recombining electrons and holes) can emit into. The change in the emission rate is known as

the Purcell effect and is described by a Purcell factor, F_p [130]. The rate balance equation (Eq. [7.2]) becomes:

$$\gamma_{in} = F_p \gamma^0_{emit} + \gamma_{NR} + \gamma_{abs} \tag{7.7}$$

where we have assumed that the internal non-radiative rate has not changed, $\gamma_{NR} = \gamma^0_{NR}$; however, a new set of non-radiative channels exist resulting in the rate γ_{abs}. We also assume that the absorption and emission occur at significantly different frequencies or are for different optical modes, such that the absorption rate is minimally affected. The V_{oc} can then be written as:

$$V_{oc} \approx \frac{k_B T}{q} \ln\left(\frac{J_L}{J_0}\right) - \frac{k_B T}{q} \ln\left(F + \frac{\gamma_{abs}}{\gamma^0_{ext}} + \frac{1-\eta^0_{ext}}{\eta^0_{ext}}\right) \tag{7.8}$$

For an ideal optical structure with $\gamma_{abs} \to 0$ and no Purcell modification, $F_p = 1$, Eq. [7.8] reduces to that of Eq. [7.6]. If we additionally assume an ideal material, $\eta^0_{ext} \to 1$, we recover the maximum V_{oc} of Shockley and Queisser's original analysis. In our new treatment, the maximum possible theoretical voltage under ideal considerations is instead:

$$V_{oc} \approx \frac{k_B T}{q} \ln\left(\frac{J_L}{J_0}\right) - \frac{k_B T}{q} \ln\left(F_p\right) \tag{7.9}$$

However, for any real material, non-radiative recombination limits the applicability of Eq. [7.9], and Eqs. [7.7] and [7.8] must be used. The fundamental limit to η^0_{ext} for GaAs can be obtained by considering non-radiative Auger recombination only. Fig. 7.3(b) shows the efficiency as a function of Purcell factor for both the ideal case (no NR recombination) and the case of Auger recombination. Further, we note that we have used the Purcell factor to modify the emission rate without modifying the

absorption rate in the above expressions. This is valid when the emission wavelength is sufficiently different than the absorption wavelength.

7.4 Conclusions

In conclusion, we have shown the effect of spontaneous emission engineering on a solar cell. We find that the efficiency can be significantly improved, which opens new opportunities to achieve high efficiency devices.

Chapter 8: Conclusion and future outlook

In this thesis, we focused on two major directions in boosting the power conversion efficiency of solar cells. One is modifying the absorption and the other is modifying the emission of photons from the device. Detailed techniques were presented, discussed and demonstrated, including: path length enhancement using plasmonic nanoparticles, light emitting scatterers using quantum dots, and optical concentration, angle restriction, and bandgap shifting using nanophotonic principles. The use of plasmonic effects and quantum dots help increase the cells' absorption and results in larger short-circuit currents. The addition of nanophotonic elements and bandgap shifting structures can modify the cells' emission, thus improve the open-circuit voltage. The metal nanoparticles, depending on their size, shape, material and position, can increase the optical path length within the semiconductor and reduce the reflection through the excitation of surface plasmons. Adding an extra layer of quantum dots between the active material and back contact can help recycle the otherwise wasted photons, improving the absorption of an ultra-thin polymer solar cell by 28%. Nanophotonic elements introduce nanoscale concentration effects to increase the current density, modify emission spectrum and boost open-circuit voltage. The bandgap shifting effect uses photonic structures to forbid

the emission at certain wavelength range, reduce the dark current and improve the open-circuit voltage of a GaAs solar cell whose internal florescence quantum yield is only $\sim 80\%$ by 1.5 mV under 0.6 suns. In this chapter, we discuss methods for further improvements in device efficiency using these concepts.

8.1 Plasmonic nanoparticles

Plasmonic nanoparticles plays an important role in solving the trade-off between high photon absorption, which requires thick films, and efficient carrier extraction, which needs thin films. We have shown that several parameters should be taken into account in designing the nanoparticles. When applying these principles in real world situations, one must consider the effect of individual nanoparticles, the interaction between different nanoparticles, and trade-offs due to loss in the metals. Similarly, different cell technologies result in devices with different bandgap energies, absorption coefficients, and thicknesses, requiring different optimizations for each type of devices. The following considerations will be needed for each type of cell:

(1) period/correlation of positions. Although the deposition of plasmonic nanoparticles can dramatically improve the optical path length, a high particle density is not always desired. In fact, because the plasmonic nanoparticles have high absorptivity themselves, high particle densities may lead to a high loss and a reduced photo-generated current. Optimization must consider the balance between optical losses due to light absorption within the particles and light absorption within

the semiconductor.

(2) variation in size. Fabricated samples may not be as good as expected because the actual nanoparticles have a wide distribution of sizes. Designs which focus on broader resonances or those which are less sensitive to fabrication variations in size and position will be benifital for widespread implementation.

8.2 Quantum dots used in solar cells

The addition of a layer of quantum dots has been shown to improve the absorption within an ultra thin polymer solar cell by 28% through engineered photon recycling between a 20 nm quantum dots layer and a 50 nm P3HT:PCBM. Interestingly, the absorption of certain wavelengths can exceed 100% because of the absorption and emission of quantum dots can happen at different wavelength. Although such an improvement is significant, we must note that it is largely determined by the efficiency of absorption and re-emission process of quantum dots (claimed to be $\sim 100\%$ by commercial sellers).

In addition to maintain high efficiency, quantum dots used in solar cells also requires high thermal stability. The change in temperature brings photoluminescence emission wavelength shifts. The quantum dots are designed to emit at the edge of solar cells' bandgap. While blue shifts in the emission wavelength have minimal effect on the resulting photocurrent, a red shift can lead to a lack of absorption within the semiconductor. While we have pointed out that the ultra-thin solar cells can benefit from waveguiding effects introduced by quantum dots even if it couldn't

even emit, the thermal shifts in the emission spectrum need to be taken into account to wisely choose where the photoluminescence band of the quantum dots lies.

8.3 Nanopatterning

Nanopatterning offers a important alternative to improve solar cells' efficiency through microscale/nanoscale concentration. The reduced volume of nanopatterned solar cell can potentially increase the light generated current density and thus result in an enhancement of the open-circuit voltage. Ideally, this concentration effect helps increase the solar cells' efficiency from 30.9% to 41.7%. Although it surpasses the Shockley-Queisser limit of planner solar cells, it doesn't exceed the efficiency limit of concentrated solar cells. To break that limit, one must use third generation techniques such as multi-exciton generation.

Although GaAs solar cells are mainly discussed in this thesis, it is worthwhile to notice that GaAs is not the best material for nanopatterning, because of its high surface non-radiative recombination velocity. The increased surface area of GaAs solar cells caused by nanopatterning can seriously hinder the improvement in solar cell efficiency. Furthermore, the nanopatterned solar cells should be carefully designed according to the local condition of incident illumination. We have shown that for different diffusive illumination conditions the best cut-off energy for nanoscale concentration changes. Because the illumination condition varies by areas, to get the highest power conversion efficiency, the percentage of diffusive illumination should be carefully considered during the design phase.

8.4 Bandgap shifting

Bandgap shifting introduces an all photonic way to alter the effective bandgap of semiconductors. We, for the first time, have demonstrated that by simply putting a wavelength selective reflector atop, a GaAs solar cell enables a voltage enhancement of 1.7 mV for a solar cell. Noticing that our internal florescence quantum yield of our sample is $\sim 83\%$, we expected to see a much bigger voltage enhancement by using a high quality GaAs solar cell. Future experience should thus be conducted on high radiative efficiency devices.

Appendix A: The Munday Lab software for detailed balance calculation

A.1 Introduction

As is described in this thesis, the detailed balance model is very important in determining the upper bound of the efficiency of solar cells. We generalized the detailed balance model in nano, photonic, multi-junction structures and used Matlab to run the calculations (Fig. A.1).

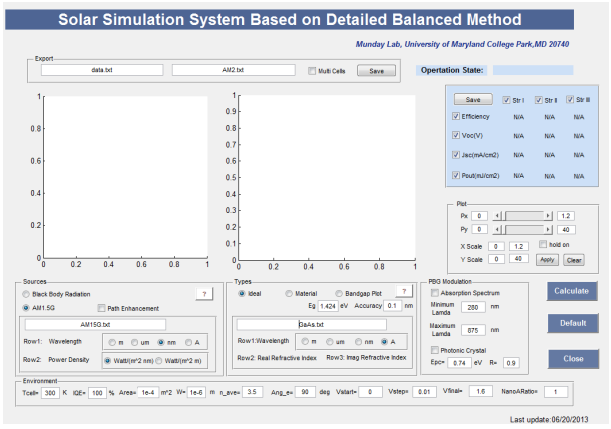

Figure A.1: The Munday Lab software for detailed balance calculation

A.2 Code

```
function varargout = ALL(varargin)
% ALL MATLAB code for ALL.fig
%      ALL, by itself, creates a new ALL or raises the existing
%      singleton*.
%
%      H = ALL returns the handle to a new ALL or the handle to
%      the existing singleton*.
%
%      ALL('CALLBACK',hObject,eventData,handles,...) calls the
    local
%      function named CALLBACK in ALL.M with the given input
    arguments.
%
%      ALL('Property','Value',...) creates a new ALL or raises
    the
%      existing singleton*.  Starting from the left, property
    value pairs are
%      applied to the GUI before ALL_OpeningFcn gets called.  An
%      unrecognized property name or invalid value makes
    property application
%      stop.  All inputs are passed to ALL_OpeningFcn via
    varargin.
%
%      *See GUI Options on GUIDE's Tools menu.  Choose "GUI
    allows only one
%      instance to run (singleton)".
%
% See also: GUIDE, GUIDATA, GUIHANDLES

% Edit the above text to modify the response to help ALL

% Last Modified by GUIDE v2.5 18-Sep-2014 19:04:44

% Begin initialization code - DO NOT EDIT
gui_Singleton = 1;
gui_State = struct('gui_Name',       mfilename, ...
                   'gui_Singleton',  gui_Singleton, ...
                   'gui_OpeningFcn', @ALL_OpeningFcn, ...
                   'gui_OutputFcn',  @ALL_OutputFcn, ...
                   'gui_LayoutFcn',  [] , ...
                   'gui_Callback',   []);
if nargin && ischar(varargin{1})
    gui_State.gui_Callback = str2func(varargin{1});
end
```

```
38
39 if nargout
40     [varargout{1:nargout}] = gui_mainfcn(gui_State, varargin{:})
           ;
41 else
42     gui_mainfcn(gui_State, varargin{:});
43 end
44 % End initialization code - DO NOT EDIT
45
46
47 % --- Executes just before ALL is made visible.
48 function ALL_OpeningFcn(hObject, eventdata, handles, varargin)
49 % This function has no output args, see OutputFcn.
50 % hObject    handle to figure
51 % eventdata  reserved - to be defined in a future version of
       MATLAB
52 % handles    structure with handles and user data (see GUIDATA)
53 % varargin   command line arguments to ALL (see VARARGIN)
54
55 % Choose default command line output for ALL
56 handles.output = hObject;
57
58 % Update handles structure
59 guidata(hObject, handles);
60
61 % UIWAIT makes ALL wait for user response (see UIRESUME)
62 % uiwait(handles.figure1);
63 Openning=['Welcome to Munday Lab Solar Simulation System
                ,
64           'this system is based on detailed balance method
                        ,
65           '
                ,
66           'file opennig, please wait.....
                                        ,
67           '          for technical support please contact
                 ylxu@umd.edu ']
68  fid=fopen('default_material.dat','rt');
69  %A=
70  set(findobj(gcf,'Tag','MatAddress'),'string',fscanf(fid,'%s'));
71  %fclose(fid);
72  fid=fopen('default_source.dat','rt');
73  set(findobj(gcf,'Tag','AM15'),'string',fscanf(fid,'%s'));
74  %fclose(fid);
75
76 fid=fopen('default_savepath.dat','rt');
```

```
77 set(findobj(gcf,'Tag','edit28'),'string',fscanf(fid,'%s'));
78
79 % --- Outputs from this function are returned to the command
       line.
80 function varargout = ALL_OutputFcn(hObject, eventdata, handles)
81 % varargout  cell array for returning output args (see VARARGOUT
       );
82 % hObject    handle to figure
83 % eventdata  reserved - to be defined in a future version of
       MATLAB
84 % handles    structure with handles and user data (see GUIDATA)
85
86 % Get default command line output from handles structure
87 varargout{1} = handles.output;
88
89
90 % --- Executes on button press in pushbutton1.
91 function pushbutton1_Callback(hObject, eventdata, handles)
92 % hObject    handle to pushbutton1 (see GCBO)
93 % eventdata  reserved - to be defined in a future version of
       MATLAB
94 % handles    structure with handles and user data (see GUIDATA)
95 %hObject.Type3
96 ConsiderARC=get(findobj(gcf,'Tag','ARC'),'value');
97 BAND=get(findobj(gcf,'Tag','Type3'),'value');
98 str1=get(findobj(gcf,'Tag','str1'),'value');
99 str2=get(findobj(gcf,'Tag','str2'),'value');
100 str3=get(findobj(gcf,'Tag','str3'),'value');
101 holdon=get(findobj(gcf,'Tag','holdon'),'value');
102 Vol_start=str2double(get(findobj(gcf,'Tag','edit29'),'string'));
103 Vol_step=str2double(get(findobj(gcf,'Tag','edit30'),'string'));
104 Vol_stop=str2double(get(findobj(gcf,'Tag','edit31'),'string'));
105 Area=str2double(get(findobj(gcf,'Tag','Area'),'string'));
106 rate=(str2double(get(findobj(gcf,'Tag','pathratio'),'string')))
       ^2;
107 electron=1.6e-19;
108 W=str2double(get(findobj(gcf,'Tag','Width'),'string')); %m   1um
109 n=str2double(get(findobj(gcf,'Tag','nassume'),'string'));
110 c=3e8; %m/s
111 h=6.626068e-34; % J.s
112 T=str2double(get(findobj(gcf,'Tag','Tcell'),'string')); %k
113 Splitmin=str2double(get(findobj(gcf,'Tag','splitmin'),'string'))
       ;
114 Splitmax=str2double(get(findobj(gcf,'Tag','splitmax'),'string'))
       ;
115 theta_emit=str2double(get(findobj(gcf,'Tag','angleemi'),'string'
       ))*pi/180;
```

```
116 wavelengthstep=str2double(get(findobj(gcf,'Tag','edit45'),'
    string'));%nm
117
118 bolzman_k=1.3806503e-23;% J/k
119
120 lam_min=max(1e-9,str2double(get(findobj(gcf,'Tag','splitmin'),'
    string'))*1e-9);
121 inc_num=1;
122 lamda_pcry=(h*c/electron/str2double(get(findobj(gcf,'Tag','PCEpc
    '),'string')));
123 if get(findobj(gcf,'Tag','PCsADD'),'value')
124     pcsrefl=str2double(get(findobj(gcf,'Tag','edit41'),'string')
        );
125 else
126     pcsrefl=0;
127 end
128
129 %%%%%%%%%%%%%%%source
130 if get(findobj(gcf,'Tag','Source1'),'value')
131     Ts=str2double(get(findobj(gcf,'Tag','BBR2'),'string'));
132     stp=1;
133 elseif get(findobj(gcf,'Tag','Source2'),'value')
134     stp=2;
135     file2=load(get(findobj(gcf,'Tag','AM15'),'string'));%'E:\
        Yunlu\independent study\AM15G.txt');
136     %AAA=get(findobj(gcf,'Tag','AM15'),'string')
137
138     UNIT=0;
139     UNIT=UNIT+get(findobj(gcf,'Tag','UNT1'),'value')*1;
140     UNIT=UNIT+get(findobj(gcf,'Tag','UNT2'),'value')*6;
141     UNIT=UNIT+get(findobj(gcf,'Tag','UNT3'),'value')*9;
142     UNIT=UNIT+get(findobj(gcf,'Tag','UNT4'),'value')*10;
143
144     file2_lam=file2(1:length(file2),1)/(10^UNIT); %m
145
146     UNITT=0;
147     UNITT=UNITT+get(findobj(gcf,'Tag','UNTT1'),'value')*1;
148     UNITT=UNITT+get(findobj(gcf,'Tag','UNTT2'),'value')*9;
149
150     file2_ene=file2(1:length(file2),2)*10^9; %W/(m^2 m)
151
152     if min(file2_lam)>lam_min
153         lam_min=min(file2_lam);
154     end
155 end
156
157 Eg00=str2double(get(findobj(gcf,'Tag','Eg'),'string'));
```

```
158
159 file=load(get(findobj(gcf,'Tag','MatAddress'),'string'));%'E:\
    Yunlu\independent study\GaAs.txt');
160       TUNIT=0;
161       TUNIT=TUNIT+get(findobj(gcf,'Tag','TUNT1'),'value')*1;
162       TUNIT=TUNIT+get(findobj(gcf,'Tag','TUNT2'),'value')*6;
163       TUNIT=TUNIT+get(findobj(gcf,'Tag','TUNT3'),'value')*9;
164       TUNIT=TUNIT+get(findobj(gcf,'Tag','TUNT4'),'value')*10;
165 file_lam=file(1:length(file),1)/(10^TUNIT); %axtom-> meters
166 file_n=file(1:length(file),2);
167 file_k=file(1:length(file),3);
168
169 if min(file_lam)>lam_min
170     lam_min=min(file_lam);
171 end
172
173 if BAND==0
174     Estart=Eg00;
175 else
176     Estart=str2double(get(findobj(gcf,'Tag','Eminn'),'string'));
177     %lam_min=1e-9;
178 end
179 %if ((get(findobj(gcf,'Tag','Type1'),'value'))|(get(findobj(gcf
    ,'Tag','Type2'),'value')) )
180 numctr=0;
181
182 Estepp=str2double(get(findobj(gcf,'Tag','Estepp'),'string'));
183 global eff1
184 eff1=zeros(length(Estart:Estepp:Eg00),1);
185 global eff2
186 eff2=zeros(length(Estart:Estepp:Eg00),1);
187 global eff3
188 eff3=zeros(length(Estart:Estepp:Eg00),1);
189
190 for(E00=Estart:Estepp:Eg00)
191     numctr=numctr+1;
192
193     Eg=E00;
194     lamDC=(((lam_min)*1e9):wavelengthstep:(h*c/(electron*Eg)*1e9
        ))/1e9; %m the range of lamda;
195     if get(findobj(gcf,'Tag','Absmod'),'value')
196         lam=(((lam_min)*1e9):wavelengthstep:min(((h*c/(electron*
            Eg)*1e9)),str2double(get(findobj(gcf,'Tag','splitmax'
            ),'string'))))/1e9; %m the range of lamda;
197     else
198         lam=lamDC;
199     end
```

```
200     %photo generated current
201     real_n=interp1(file_lam,file_n,lam);
202     imga_k=interp1(file_lam,file_k,lam);
203     alpha=4*pi*imga_k./lam;
204     %dark current
205     real_nDC=interp1(file_lam,file_n,lamDC);
206     imga_kDC=interp1(file_lam,file_k,lamDC);
207     alphaDC=4*pi*imga_kDC./lamDC;
208     %%%%%%%%%%%%
209     %rate=6.955e8/149597870700;
210     %rate=1;
211     if stp==1
212         E=h*c./lam;
213         %ENE=pi*2/h^3/c^2*h*c*E.^2./(exp(E./bolzman_k/Ts)-1).*(h
                *c./lam.^2)./lam/rate;
214         ENE=2/h^3/c^2*h*c*E.^2./(exp(E./bolzman_k/Ts)-1).*(h*c./
                lam.^2)./lam; %per Area/Wavelength/solid angle
215         lam_total=(1:1:7000)*1e-9;
216         E_total=h*c./lam_total;
217         %ENE_total=pi*2/h^3/c^2*h*c*E_total.^2./(exp(E_total./
                bolzman_k/Ts)-1).*(h*c./lam_total.^2)./lam_total/rate
                ;
218         ENE_total=2/h^3/c^2*h*c*E_total.^2./(exp(E_total./
                bolzman_k/Ts)-1).*(h*c./lam_total.^2)./lam_total
                *0.0000108579*2*pi;%/; %per Area/Wavelength/solid
                angle
219         %PL=1351*Area
220         PL=sum(ENE_total)*1e-9*Area; %why not 2pi? cos theta
221     elseif stp==2
222         ENE=interp1(file2_lam,file2_ene,lam);
223         PL=0;
224         for(i=2:(length(file2_lam)-1))
225             PL=PL+file2_ene(i)*(file2_lam(i+1)-file2_lam(i-1))
                    /2*Area;
226         end
227
228     end
229
230 PL
231
232     SourcePower1=zeros(10,length(ENE));
233     SourcePower2=zeros(10,length(ENE));
234     SourcePower1(1,1:length(ENE))=ENE;
235     SourcePower2(1,1:length(ENE))=ENE;
236     af1=1;
237     af2=1;
238     ar1=1;
```

```
239         ar2=1;
240         ConsiderAbs=get(findobj(gcf,'Tag','Type2'),'value');
241         %%%%%%%%% add jsc judgement
242             %for(cellthick0=0.01:0.01:5) %um
243         I1=0;
244         I2=0;
245         I3=0;
246         global IL1
247         IL1=0;
248         global IL2
249         IL2=0;
250         %dark current
251         the=0:theta_emit/180:theta_emit;
252         I_dens=zeros(length(the),length(lamDC));
253         II_dens=zeros(length(the),length(lamDC));
254         III_dens=zeros(length(the),length(lamDC));
255         darkcurrent=max(lamDC);
256         max(lamDC)
257         for(j=1:length(lamDC))%calculation
258             for (i=1:length(the))
259                 theta=the(i);
260                 lamda=lamDC(j);
261                 E=h*c/lamda;
262                 if lamda> lamda_pcry
263                     reflectivity_yita=pcsrefl;
264                 else
265                     reflectivity_yita=0;
266                 end
267                 thetai=acos(sqrt(1-sin(theta)^2/n^2));
268                 thetaC=asin(1/real_nDC(j));
269                 if ConsiderARC==0
270                     ARC=1;%NRefractive(j)^2*4; %%%%%%%%%%%%%%%%%this
                            is for AR coating
271                 else
272                     ARC=real_nDC(j)^2*4;
273                 end
274                 if ConsiderAbs
275                     af1=1-exp(-alphaDC(j)*W*ARC./cos(thetai));
276                     af2=1-exp(-2*alphaDC(j)*W*ARC./cos(thetai));
277                     ar1=1-exp(-alphaDC(j)*W*ARC./cos(theta));
278                     ar2=1-exp(-2*alphaDC(j)*W*ARC./cos(theta));
279                 end
280                 bE=2*E^2/h^3/c^2/(exp((E)/bolzman_k/T)-1);
281                 if(theta<thetaC)
282                     I_dens(i,j)=2*pi*1.6e-19*Area*(af1+ar1*real_nDC(j
                            )^2)*bE*cos(theta)*sin(theta)*(h*c/lamda^2)
                            *(1-reflectivity_yita);
```

```
283             else
284                 I_dens(i,j)=2*pi*1.6e-19*Area*(af1+ar2*real_nDC(j
                        )^2)*bE*cos(theta)*sin(theta)*(h*c/lamda^2)
                        *(1-reflectivity_yita);
285             end
286             II_dens(i,j)=2*pi*1.6e-19*Area*af2      *bE*cos(theta)
                    *sin(theta)*(h*c/lamda^2)*(1-reflectivity_yita);
287             III_dens(i,j)=2*pi*1.6e-19*Area*(2*af1)*bE*cos(theta)
                    *sin(theta)*(h*c/lamda^2)*(1-reflectivity_yita);
288         end
289     end
290
291     %%%%%%integration
292     I1_tempdens=zeros(1,length(the));
293     I2_tempdens=zeros(1,length(the));
294     I3_tempdens=zeros(1,length(the));
295
296     for(i=1:1:length(the))
297         I1_tempdens(i)=trapz(lamDC,I_dens(i,:));
298         I2_tempdens(i)=trapz(lamDC,II_dens(i,:));
299         I3_tempdens(i)=trapz(lamDC,III_dens(i,:));
300     end
301     I1=trapz(the,I1_tempdens);
302     I2=trapz(the,I2_tempdens);
303     I3=trapz(the,I3_tempdens);
304
305
306     %photo generated current
307     if stp==1
308         the=0:(0.267/180*pi)/180:(0.267/180*pi);
309     elseif stp==2
310         the=0:(90/180*pi)/180:(90/180*pi); % just because int(2
                cosx sinx x=0:pi/2)=1
311     end
312     IL1_dens=zeros(length(the),length(lam));
313     IL2_dens=zeros(length(the),length(lam));
314     photongcurrent=max(lam);
315     for(j=1:length(lam))%calculation
316         for (i=1:length(the))
317             theta=the(i);
318             lamda=lam(j);
319             E=h*c/lamda;
320             if lamda> lamda_pcry
321                 reflectivity_yita=pcsrefl;
322             else
323                 reflectivity_yita=0;
324             end
```

```
325             thetai=acos(sqrt(1-sin(theta)^2/n^2));
326             thetaC=asin(1/real_n(j));
327             if ConsiderARC==0
328                 ARC=1;%NRefractive(j)^2*4; %%%%%%%%%%%%%%%%%this
                        is for AR coating
329             else
330                 ARC=real_n(j)^2*4;
331             end
332
333             if ConsiderAbs
334                 af1=1-exp(-alpha(j)*W*ARC./cos(thetai));
335                 af2=1-exp(-2*alpha(j)*W*ARC./cos(thetai));
336                 ar1=1-exp(-alpha(j)*W*ARC./cos(theta));
337                 ar2=1-exp(-2*alpha(j)*W*ARC./cos(theta));
338             end
339             if stp==1
340                 IL1_dens(i,j)=1.6e-19*af1*SourcePower1(1,j)*2*pi*
                        cos(theta)*sin(theta)/(h*c/lamda)*Area*(1-
                        reflectivity_yita);
341                 IL2_dens(i,j)=1.6e-19*af2*SourcePower2(1,j)*2*pi*
                        cos(theta)*sin(theta)/(h*c/lamda)*Area*(1-
                        reflectivity_yita);
342                       %(i,j)=SourcePower1(1,j)*2*pi*cos(theta)
                            *sin(theta)*Area*(1-reflectivity_yita
                            );
343             elseif stp==2
344                 IL1_dens(i,j)=1.6e-19*af1*SourcePower1(1,j)*2*cos
                        (theta)*sin(theta)/(h*c/lamda)*Area*(1-
                        reflectivity_yita);
345                 IL2_dens(i,j)=1.6e-19*af2*SourcePower2(1,j)*2*cos
                        (theta)*sin(theta)/(h*c/lamda)*Area*(1-
                        reflectivity_yita);
346             end
347             if i==1
348                 topmost=1;
349                 lowest=0;
350             elseif i==length(the)
351                 topmost=0;
352                 lowest=1;
353             else
354                 topmost=1;
355                 lowest=1;
356             end
357             SourcePower1(2,j)=SourcePower1(2,j)+(1-af1)*2*
                    SourcePower1(1,j)*cos(theta)*sin(theta)*(the(i+
                    topmost)-the(i-lowest))/2;
```

```
358                 SourcePower2(2,j)=SourcePower2(2,j)+(1-af1)*2*
                        SourcePower2(1,j)*cos(theta)*sin(theta)*(the(i+
                        topmost)-the(i-lowest))/2;
359             end
360         end
361         %%%%%%integration
362         IL1_tempdens=zeros(1,length(the));
363         IL2_tempdens=zeros(1,length(the));
364         for(i=1:1:length(the))
365         IL1_tempdens(i)=trapz(lam,IL1_dens(i,:));
366         IL2_tempdens(i)=trapz(lam,IL2_dens(i,:));
367         end
368         IL1=trapz(the,IL1_tempdens)
369         IL2=trapz(the,IL2_tempdens)
370
371
372
373     %%%%%%  Electrical property
374     global Voltage;
375     Voltage=Vol_start:Vol_step:Vol_stop;
376     IQE=str2double(get(findobj(gcf,'Tag','intqeff'),'string'))/100;
377     global I_s1;
378     global I_s2;
379     global I_s3;
380     AreaRATIO=str2double(get(findobj(gcf,'Tag','edit44'),'string'))
            ;
381     I_s1=IL1*AreaRATIO-(I1)*(exp(1.6e-19.*Voltage/bolzman_k/T)-1)
            *(1+4*n^2*(1/IQE-1)/(sin(theta_emit)^2));
382     I_s2=IL2*AreaRATIO-(I2)*(exp(1.6e-19.*Voltage/bolzman_k/T)-1)
            *(1+4*n^2*(1/IQE-1)/(sin(theta_emit)^2));
383     I_s3=IL1*AreaRATIO-(I3)*(exp(1.6e-19.*Voltage/bolzman_k/T)-1)
            *(1+4*n^2*(1/IQE-1)/(sin(theta_emit)^2));
384     AreaRATIO
385     I1
386     IL1
387     I2
388     I3
389     PL=PL*AreaRATIO;
390     enhancement=(1+4*n^2*(1/IQE-1)/(sin(theta_emit)^2));
391
392
393     global PMout1;
394     global PMout2;
395     global PMout3;
396     PMout1=max(I_s1.*Voltage);
397     PMout2=max(I_s2.*Voltage);
398     PMout3=max(I_s3.*Voltage);
```

```
399   eff1(numctr)=max(I_s1.*Voltage)/PL;
400   eff2(numctr)=max(I_s2.*Voltage)/PL;
401   eff3(numctr)=max(I_s3.*Voltage)/PL;
402                 %FF1=sum(I_s1(1:max(find(I_s1>=0)))*Vol_step)/(IL1
                        .*log(IL1/I1+1)*T*bolzman_k/electron)
403                % if abs(I_s1*1000-15.9)<1
404                 %    W
405                 %     break
406                 %end
407           %SourcePower1(2,1:length(ENE))./SourcePower1(1,1:length(
                  ENE))
408           %%%%%%%%%%%%%%%%%%%source2%%%%%%%%%%%%%%%%%%%%
409       if get(findobj(gcf,'Tag','MulC'),'value')
410       rownum=2;
411       fid=fopen(get(findobj(gcf,'Tag','edit36'),'string'),'wt');
412       Output=[(lam*1e9)',(SourcePower1(2,1:length(ENE))/1e9)'];
413
414       for i=1:length(Output)
415
416           fprintf(fid,'%4d',Output(i,1));
417           fprintf(fid,'%14d',Output(i,2));
418           fprintf(fid,'\n');
419       end
420       fclose(fid);
421       end
422
423   end
424   set(findobj(gcf,'Tag','operation'),'string','Calculation
          Completed');
425   %%%%%%%%%%%%%%%%efficiency
426   if get(findobj(gcf,'Tag','effcheck'),'value')
427       if get(findobj(gcf,'Tag','str1'),'value')
428       set(findobj(gcf,'Tag','eff1'),'string',num2str(max(eff1)));
429       end
430       if get(findobj(gcf,'Tag','str2'),'value')
431       set(findobj(gcf,'Tag','eff2'),'string',num2str(max(eff2)));
432       end
433       if get(findobj(gcf,'Tag','str3'),'value')
434       set(findobj(gcf,'Tag','eff3'),'string',num2str(max(eff3)));
435       end
436   end
437   %%%%%%%%%%%%Voc
438       global Voc1
439       Voc1=log(IL1*AreaRATIO/I1/(1+4*n^2*(1/IQE-1)/(sin(theta_emit
              )^2))+1)*T*bolzman_k/electron;
440       global Voc2
```

```
441         Voc2=log(IL2*AreaRATIO/I2/(1+4*n^2*(1/IQE-1)/(sin(theta_emit
                )^2))+1)*T*bolzman_k/electron;
442         global Voc3
443         Voc3=log(IL1*AreaRATIO/I3/(1+4*n^2*(1/IQE-1)/(sin(theta_emit
                )^2))+1)*T*bolzman_k/electron;
444
445     if get(findobj(gcf,'Tag','voccheck'),'value')
446
447         if get(findobj(gcf,'Tag','str1'),'value')
448         set(findobj(gcf,'Tag','voc1'),'string',num2str(Voc1));
449         end
450         if get(findobj(gcf,'Tag','str2'),'value')
451         set(findobj(gcf,'Tag','voc2'),'string',num2str(Voc2));
452         end
453         if get(findobj(gcf,'Tag','str3'),'value')
454         set(findobj(gcf,'Tag','voc3'),'string',num2str(Voc3));
455         end
456     end
457     %%%%%%%%%%%%%%%%Isc
458     if get(findobj(gcf,'Tag','isccheck'),'value')
459         if get(findobj(gcf,'Tag','str1'),'value')
460         set(findobj(gcf,'Tag','isc1'),'string',num2str(max(IL1*1000)
                ));
461         end
462         if get(findobj(gcf,'Tag','str2'),'value')
463         set(findobj(gcf,'Tag','isc2'),'string',num2str(max(IL2*1000)
                ));
464         end
465         if get(findobj(gcf,'Tag','str3'),'value')
466         set(findobj(gcf,'Tag','isc3'),'string',num2str(max(IL1*1000)
                ));
467         end
468     end
469     if get(findobj(gcf,'Tag','poutcheck'),'value')
470         if get(findobj(gcf,'Tag','str1'),'value')
471         set(findobj(gcf,'Tag','pout1'),'string',num2str(PMout1*1000)
                );
472         end
473         if get(findobj(gcf,'Tag','str2'),'value')
474         set(findobj(gcf,'Tag','pout2'),'string',num2str(PMout2*1000)
                );
475         end
476         if get(findobj(gcf,'Tag','str3'),'value')
477         set(findobj(gcf,'Tag','pout3'),'string',num2str(PMout3*1000)
                );
478         end
479     end
```

```
480 %%%%%%%%%%%%%%%plot
481 set(gcf,'currentaxes',handles.axes1);
482 if holdon==0
483     cla reset;
484 end
485 if stp==1
486         plot(lam_total*1e9,ENE_total);
487         hold on;
488         plot([Splitmin,Splitmin],[0,max(ENE_total)],'r');
489         hold on;
490         plot([Splitmax,Splitmax],[0,max(ENE_total)],'r');
491         text(Splitmax,max(ENE_total)*0.8,'\leftarrow Abs Spectrum
              ');
492         hold on;
493
494         plot([lamda_pcry*1e9,lamda_pcry*1e9],[0,max(ENE_total)],'
              green');
495         text(lamda_pcry*1e9,max(ENE_total),'\leftarrow Epc');
496         hold on;
497
498         plot([max(lamDC)*1e9,max(lamDC)*1e9],[0,max(ENE_total)],'
              black');
499         text(max(lamDC)*1e9,max(ENE_total)*0.9,'\leftarrow Rad
              Spectrum');
500         hold on;
501 elseif stp==2
502         plot(file2_lam*1e9,file2_ene);
503         hold on;
504         plot([Splitmin,Splitmin],[0,max(file2_ene)],'r');
505         hold on;
506         plot([Splitmax,Splitmax],[0,max(file2_ene)],'r');
507         text(Splitmax,max(file2_ene)*0.8,'\leftarrow Abs Spectrum
              ');
508         hold on;
509
510         plot([lamda_pcry*1e9,lamda_pcry*1e9],[0,max(file2_ene)],'
              green');
511         text(lamda_pcry*1e9,max(file2_ene),'\leftarrow Photonic
              Bandgap');
512         hold on;
513
514
515         plot([max(lamDC)*1e9,max(lamDC)*1e9],[0,max(file2_ene)],'
              black');
516         text(max(lamDC)*1e9,max(file2_ene)*0.9,'\leftarrow Rad
              Spectrum');
517         hold on;
```

```
518 end
519 xlabel('Wavelength(nm)');
520 ylabel('Power/(Area Wavelength)');
521
522 set(gcf,'currentaxes',handles.axes2);
523 if holdon==0
524     cla reset;
525 end
526 if BAND==0
527         if str1==1
528           plot(Voltage,I_s1*1000,'r');
529           hold on;
530         end
531         if str2==1
532            plot(Voltage,I_s2*1000,'black');
533            hold on;
534         end
535         if str3==1
536           plot(Voltage,I_s3*1000);
537           hold on;
538         end
539         xlabel('Voltage(V)');
540         ylabel('CurrentDensity(mA/cm^2)');
541         set(gca,'xlim',[0,max([Voc1,Voc2,Voc3])*1.2]);
542         set(gca,'ylim',[0,max([IL1,IL2]*1000)*1.1]);
543         %%maximum output power (related voltage)
544         Pout1=I_s1.*Voltage;
545         text(Voltage(find(Pout1==max(Pout1))),I_s2(find(Pout1==max
              (Pout1)))*1000*1.05,['V1=',num2str(Voltage(find(Pout1==
              max(Pout1))))]);
546         text(Voltage(find(Pout1==max(Pout1))),I_s2(find(Pout1==max
              (Pout1)))*1000,'\downarrow');
547         Pout2=I_s2.*Voltage;
548         text(Voltage(find(Pout2==max(Pout2))),I_s2(find(Pout2==max
              (Pout2)))*1000,['\leftarrowV2=',num2str(Voltage(find(
              Pout2==max(Pout2))))]);
549         %Pout3=I_s3.*Voltage;
550         %text(Voltage(find(Pout3==max(Pout3))),I_s2(find(Pout3==
              max(Pout3)))*1000,['\leftarrowV2=',num2str(Voltage(find
              (Pout3==max(Pout3))))]);
551
552 else
553          if str1==1
554       plot(Estart:Estepp:Eg,eff1,'r');
555           hold on;
556         end
557         if str2==1
```

```
558       plot(Estart:Estepp:Eg,eff2,'black');
559            hold on;
560         end
561         if str3==1
562       plot(Estart:Estepp:Eg,eff3);
563           hold on;
564         end
565         xlabel('BandGap(eV)');
566         ylabel('Efficiency');
567 end
568
569 %elseif get(findobj(gcf,'Tag','Type3'),'value')
570     %bandgap();
571 %end
572
573
574
575
576 %set(gcf,'currentaxes',handles.axes1);
577
578
579
580 function AM15_Callback(hObject, eventdata, handles)
581 % hObject    handle to AM15 (see GCBO)
582 % eventdata  reserved - to be defined in a future version of
    MATLAB
583 % handles    structure with handles and user data (see GUIDATA)
584
585 % Hints: get(hObject,'String') returns contents of AM15 as text
586 %        str2double(get(hObject,'String')) returns contents of
    AM15 as a double
587
588
589 % --- Executes during object creation, after setting all
    properties.
590 function AM15_CreateFcn(hObject, eventdata, handles)
591 % hObject    handle to AM15 (see GCBO)
592 % eventdata  reserved - to be defined in a future version of
    MATLAB
593 % handles    empty - handles not created until after all
    CreateFcns called
594
595 % Hint: edit controls usually have a white background on Windows
    .
596 %       See ISPC and COMPUTER.
597 if ispc && isequal(get(hObject,'BackgroundColor'), get(0,'
    defaultUicontrolBackgroundColor'))
```

```
598         set(hObject,'BackgroundColor','white');
599 end
600
601
602
603 function MatAddress_Callback(hObject, eventdata, handles)
604 % hObject    handle to MatAddress (see GCBO)
605 % eventdata  reserved - to be defined in a future version of
        MATLAB
606 % handles    structure with handles and user data (see GUIDATA)
607
608 % Hints: get(hObject,'String') returns contents of MatAddress as
         text
609 %        str2double(get(hObject,'String')) returns contents of
        MatAddress as a double
610
611
612 % --- Executes during object creation, after setting all
        properties.
613 function MatAddress_CreateFcn(hObject, eventdata, handles)
614 % hObject    handle to MatAddress (see GCBO)
615 % eventdata  reserved - to be defined in a future version of
        MATLAB
616 % handles    empty - handles not created until after all
        CreateFcns called
617
618 % Hint: edit controls usually have a white background on Windows
        .
619 %       See ISPC and COMPUTER.
620 if ispc && isequal(get(hObject,'BackgroundColor'), get(0,'
        defaultUicontrolBackgroundColor'))
621     set(hObject,'BackgroundColor','white');
622 end
623
624
625 % --- Executes on button press in ARC.
626 function ARC_Callback(hObject, eventdata, handles)
627 % hObject    handle to ARC (see GCBO)
628 % eventdata  reserved - to be defined in a future version of
        MATLAB
629 % handles    structure with handles and user data (see GUIDATA)
630
631 % Hint: get(hObject,'Value') returns toggle state of ARC
632
633
634
635 function BBR2_Callback(hObject, eventdata, handles)
```

```
636 % hObject    handle to BBR2 (see GCBO)
637 % eventdata  reserved - to be defined in a future version of
    MATLAB
638 % handles    structure with handles and user data (see GUIDATA)
639
640 % Hints: get(hObject,'String') returns contents of BBR2 as text
641 %        str2double(get(hObject,'String')) returns contents of
    BBR2 as a double
642
643
644 % --- Executes during object creation, after setting all
    properties.
645 function BBR2_CreateFcn(hObject, eventdata, handles)
646 % hObject    handle to BBR2 (see GCBO)
647 % eventdata  reserved - to be defined in a future version of
    MATLAB
648 % handles    empty - handles not created until after all
    CreateFcns called
649
650 % Hint: edit controls usually have a white background on Windows
    .
651 %       See ISPC and COMPUTER.
652 if ispc && isequal(get(hObject,'BackgroundColor'), get(0,'
    defaultUicontrolBackgroundColor'))
653     set(hObject,'BackgroundColor','white');
654 end
655
656
657
658 function Tcell_Callback(hObject, eventdata, handles)
659 % hObject    handle to Tcell (see GCBO)
660 % eventdata  reserved - to be defined in a future version of
    MATLAB
661 % handles    structure with handles and user data (see GUIDATA)
662
663 % Hints: get(hObject,'String') returns contents of Tcell as text
664 %        str2double(get(hObject,'String')) returns contents of
    Tcell as a double
665
666
667 % --- Executes during object creation, after setting all
    properties.
668 function Tcell_CreateFcn(hObject, eventdata, handles)
669 % hObject    handle to Tcell (see GCBO)
670 % eventdata  reserved - to be defined in a future version of
    MATLAB
```

```
671 % handles    empty - handles not created until after all
    CreateFcns called
672
673 % Hint: edit controls usually have a white background on Windows
    .
674 %       See ISPC and COMPUTER.
675 if ispc && isequal(get(hObject,'BackgroundColor'), get(0,'
    defaultUicontrolBackgroundColor'))
676     set(hObject,'BackgroundColor','white');
677 end
678
679
680
681 function edit7_Callback(hObject, eventdata, handles)
682 % hObject    handle to edit7 (see GCBO)
683 % eventdata  reserved - to be defined in a future version of
    MATLAB
684 % handles    structure with handles and user data (see GUIDATA)
685
686 % Hints: get(hObject,'String') returns contents of edit7 as text
687 %        str2double(get(hObject,'String')) returns contents of
    edit7 as a double
688
689
690 % --- Executes during object creation, after setting all
    properties.
691 function edit7_CreateFcn(hObject, eventdata, handles)
692 % hObject    handle to edit7 (see GCBO)
693 % eventdata  reserved - to be defined in a future version of
    MATLAB
694 % handles    empty - handles not created until after all
    CreateFcns called
695
696 % Hint: edit controls usually have a white background on Windows
    .
697 %       See ISPC and COMPUTER.
698 if ispc && isequal(get(hObject,'BackgroundColor'), get(0,'
    defaultUicontrolBackgroundColor'))
699     set(hObject,'BackgroundColor','white');
700 end
701
702
703 % --- Executes on button press in str1.
704 function str1_Callback(hObject, eventdata, handles)
705 % hObject    handle to str1 (see GCBO)
706 % eventdata  reserved - to be defined in a future version of
    MATLAB
```

```
707 % handles    structure with handles and user data (see GUIDATA)
708
709 % Hint: get(hObject,'Value') returns toggle state of str1
710 global IL1
711 global Voc1
712 global eff1
713 global PMout1
714 if get(findobj(gcf,'Tag','str1'),'value')
715     if get(findobj(gcf,'Tag','isccheck'),'value')
716         set(findobj(gcf,'Tag','isc1'),'string',num2str(IL1*1000)
              );
717     end
718     if get(findobj(gcf,'Tag','voccheck'),'value')
719         set(findobj(gcf,'Tag','voc1'),'string',num2str(Voc1));
720     end
721     if get(findobj(gcf,'Tag','effcheck'),'value')
722         set(findobj(gcf,'Tag','eff1'),'string',num2str(eff1));
723     end
724     if get(findobj(gcf,'Tag','effcheck'),'value')
725         set(findobj(gcf,'Tag','pout1'),'string',num2str(PMout1
              *1000));
726     end
727
728
729 else
730     set(findobj(gcf,'Tag','isc1'),'string','N/A');
731     set(findobj(gcf,'Tag','voc1'),'string','N/A');
732     set(findobj(gcf,'Tag','eff1'),'string','N/A');
733     set(findobj(gcf,'Tag','pout1'),'string','N/A');
734
735 end
736
737 % --- Executes on button press in pushbutton3.
738 function pushbutton3_Callback(hObject, eventdata, handles)
739 % hObject    handle to pushbutton3 (see GCBO)
740 % eventdata  reserved - to be defined in a future version of
     MATLAB
741 % handles    structure with handles and user data (see GUIDATA)
742  fid=fopen('default_material.dat','wt');
743  fprintf(fid,'%s',get(findobj(gcf,'Tag','MatAddress'),'string'))
       ;
744  fclose(fid);
745
746  fid=fopen('default_source.dat','wt');
747  fprintf(fid,'%s',get(findobj(gcf,'Tag','AM15'),'string'));
748  fclose(fid);
749
```

```
750  fid=fopen('default_savepath.dat','wt');
751  fprintf(fid,'%s',get(findobj(gcf,'Tag','edit28'),'string'));
752 fclose(fid);
753
754
755 % --- Executes on button press in pushbutton4.
756 function pushbutton4_Callback(hObject, eventdata, handles)
757 % hObject    handle to pushbutton4 (see GCBO)
758 % eventdata  reserved - to be defined in a future version of
    MATLAB
759 % handles    structure with handles and user data (see GUIDATA)
760 close;
761
762 % --- Executes on button press in holdon.
763 function holdon_Callback(hObject, eventdata, handles)
764 % hObject    handle to holdon (see GCBO)
765 % eventdata  reserved - to be defined in a future version of
    MATLAB
766 % handles    structure with handles and user data (see GUIDATA)
767
768 % Hint: get(hObject,'Value') returns toggle state of holdon
769
770
771 % --- Executes on button press in voccheck.
772 function voccheck_Callback(hObject, eventdata, handles)
773 % hObject    handle to voccheck (see GCBO)
774 % eventdata  reserved - to be defined in a future version of
    MATLAB
775 % handles    structure with handles and user data (see GUIDATA)
776
777 % Hint: get(hObject,'Value') returns toggle state of voccheck
778 global Voc1
779 global Voc2
780 global Voc3
781 if get(findobj(gcf,'Tag','voccheck'),'value')
782     if get(findobj(gcf,'Tag','str1'),'value')
783     set(findobj(gcf,'Tag','voc1'),'string',num2str(Voc1));
784     end
785     if get(findobj(gcf,'Tag','str2'),'value')
786     set(findobj(gcf,'Tag','voc2'),'string',num2str(Voc2));
787     end
788     if get(findobj(gcf,'Tag','str3'),'value')
789     set(findobj(gcf,'Tag','voc3'),'string',num2str(Voc3));
790     end
791 else
792     set(findobj(gcf,'Tag','voc1'),'string','N/A');
793     set(findobj(gcf,'Tag','voc2'),'string','N/A');
```

```
794      set(findobj(gcf,'Tag','voc3'),'string','N/A');
795  end
796
797  % --- Executes on button press in effcheck.
798  function effcheck_Callback(hObject, eventdata, handles)
799  % hObject    handle to effcheck (see GCBO)
800  % eventdata  reserved - to be defined in a future version of
        MATLAB
801  % handles    structure with handles and user data (see GUIDATA)
802
803  % Hint: get(hObject,'Value') returns toggle state of effcheck
804  global eff1;
805  global eff2;
806  global eff3;
807
808  if get(findobj(gcf,'Tag','effcheck'),'value')
809      if get(findobj(gcf,'Tag','str1'),'value')
810      set(findobj(gcf,'Tag','eff1'),'string',num2str(max(eff1)));
811      end
812      if get(findobj(gcf,'Tag','str2'),'value')
813      set(findobj(gcf,'Tag','eff2'),'string',num2str(max(eff2)));
814      end
815      if get(findobj(gcf,'Tag','str3'),'value')
816      set(findobj(gcf,'Tag','eff3'),'string',num2str(max(eff3)));
817      end
818  else
819      set(findobj(gcf,'Tag','eff1'),'string','N/A');
820      set(findobj(gcf,'Tag','eff2'),'string','N/A');
821      set(findobj(gcf,'Tag','eff3'),'string','N/A');
822  end
823
824
825  function X1_Callback(hObject, eventdata, handles)
826  % hObject    handle to X1 (see GCBO)
827  % eventdata  reserved - to be defined in a future version of
        MATLAB
828  % handles    structure with handles and user data (see GUIDATA)
829
830  % Hints: get(hObject,'String') returns contents of X1 as text
831  %        str2double(get(hObject,'String')) returns contents of
        X1 as a double
832
833
834  % --- Executes during object creation, after setting all
        properties.
835  function X1_CreateFcn(hObject, eventdata, handles)
836  % hObject    handle to X1 (see GCBO)
```

```
837 % eventdata  reserved - to be defined in a future version of
    MATLAB
838 % handles    empty - handles not created until after all
    CreateFcns called
839
840 % Hint: edit controls usually have a white background on Windows
    .
841 %       See ISPC and COMPUTER.
842 if ispc && isequal(get(hObject,'BackgroundColor'), get(0,'
    defaultUicontrolBackgroundColor'))
843     set(hObject,'BackgroundColor','white');
844 end
845
846
847
848 function X2_Callback(hObject, eventdata, handles)
849 % hObject    handle to X2 (see GCBO)
850 % eventdata  reserved - to be defined in a future version of
    MATLAB
851 % handles    structure with handles and user data (see GUIDATA)
852
853 % Hints: get(hObject,'String') returns contents of X2 as text
854 %        str2double(get(hObject,'String')) returns contents of
    X2 as a double
855
856
857 % --- Executes during object creation, after setting all
    properties.
858 function X2_CreateFcn(hObject, eventdata, handles)
859 % hObject    handle to X2 (see GCBO)
860 % eventdata  reserved - to be defined in a future version of
    MATLAB
861 % handles    empty - handles not created until after all
    CreateFcns called
862
863 % Hint: edit controls usually have a white background on Windows
    .
864 %       See ISPC and COMPUTER.
865 if ispc && isequal(get(hObject,'BackgroundColor'), get(0,'
    defaultUicontrolBackgroundColor'))
866     set(hObject,'BackgroundColor','white');
867 end
868
869
870
871 function Y1_Callback(hObject, eventdata, handles)
872 % hObject    handle to Y1 (see GCBO)
```

```
873 % eventdata  reserved - to be defined in a future version of
    MATLAB
874 % handles    structure with handles and user data (see GUIDATA)
875
876 % Hints: get(hObject,'String') returns contents of Y1 as text
877 %        str2double(get(hObject,'String')) returns contents of
    Y1 as a double
878
879
880 % --- Executes during object creation, after setting all
    properties.
881 function Y1_CreateFcn(hObject, eventdata, handles)
882 % hObject    handle to Y1 (see GCBO)
883 % eventdata  reserved - to be defined in a future version of
    MATLAB
884 % handles    empty - handles not created until after all
    CreateFcns called
885
886 % Hint: edit controls usually have a white background on Windows
    .
887 %       See ISPC and COMPUTER.
888 if ispc && isequal(get(hObject,'BackgroundColor'), get(0,'
    defaultUicontrolBackgroundColor'))
889     set(hObject,'BackgroundColor','white');
890 end
891
892
893
894 function Y2_Callback(hObject, eventdata, handles)
895 % hObject    handle to Y2 (see GCBO)
896 % eventdata  reserved - to be defined in a future version of
    MATLAB
897 % handles    structure with handles and user data (see GUIDATA)
898
899 % Hints: get(hObject,'String') returns contents of Y2 as text
900 %        str2double(get(hObject,'String')) returns contents of
    Y2 as a double
901
902
903 % --- Executes during object creation, after setting all
    properties.
904 function Y2_CreateFcn(hObject, eventdata, handles)
905 % hObject    handle to Y2 (see GCBO)
906 % eventdata  reserved - to be defined in a future version of
    MATLAB
907 % handles    empty - handles not created until after all
    CreateFcns called
```

```
908
909 % Hint: edit controls usually have a white background on Windows
        .
910 %       See ISPC and COMPUTER.
911 if ispc && isequal(get(hObject,'BackgroundColor'), get(0,'
    defaultUicontrolBackgroundColor'))
912     set(hObject,'BackgroundColor','white');
913 end
914
915
916 % --- Executes on button press in pushbutton2.
917 function pushbutton2_Callback(hObject, eventdata, handles)
918 % hObject    handle to pushbutton2 (see GCBO)
919 % eventdata  reserved - to be defined in a future version of
    MATLAB
920 % handles    structure with handles and user data (see GUIDATA)
921 set(gca,'xlim',[str2double(get(findobj(gcf,'Tag','X1'),'string')
    ),str2double(get(findobj(gcf,'Tag','X2'),'string'))]);
922 set(gca,'ylim',[str2double(get(findobj(gcf,'Tag','Y1'),'string')
    ),str2double(get(findobj(gcf,'Tag','Y2'),'string'))]);
923
924
925
926 % --- Executes on button press in str3.
927 function str3_Callback(hObject, eventdata, handles)
928 % hObject    handle to str3 (see GCBO)
929 % eventdata  reserved - to be defined in a future version of
    MATLAB
930 % handles    structure with handles and user data (see GUIDATA)
931
932 % Hint: get(hObject,'Value') returns toggle state of str3
933 global IL1
934 global Voc3
935 global eff3
936 global PMout3
937 if get(findobj(gcf,'Tag','str3'),'value')
938     if get(findobj(gcf,'Tag','isccheck'),'value')
939         set(findobj(gcf,'Tag','isc3'),'string',num2str(IL1*1000)
            );
940     end
941     if get(findobj(gcf,'Tag','voccheck'),'value')
942         set(findobj(gcf,'Tag','voc3'),'string',num2str(Voc3));
943     end
944     if get(findobj(gcf,'Tag','effcheck'),'value')
945         set(findobj(gcf,'Tag','eff3'),'string',num2str(eff3));
946     end
947     if get(findobj(gcf,'Tag','effcheck'),'value')
```

```
948             set(findobj(gcf,'Tag','pout3'),'string',num2str(PMout3
                    *1000));
949         end
950
951     else
952         set(findobj(gcf,'Tag','isc3'),'string','N/A');
953         set(findobj(gcf,'Tag','voc3'),'string','N/A');
954         set(findobj(gcf,'Tag','eff3'),'string','N/A');
955         set(findobj(gcf,'Tag','pout3'),'string','N/A');
956
957     end
958
959     % --- Executes on button press in str2.
960     function str2_Callback(hObject, eventdata, handles)
961     % hObject    handle to str2 (see GCBO)
962     % eventdata  reserved - to be defined in a future version of
            MATLAB
963     % handles    structure with handles and user data (see GUIDATA)
964
965     % Hint: get(hObject,'Value') returns toggle state of str2
966     global IL2
967     global Voc2
968     global eff2
969     global PMout2
970     if get(findobj(gcf,'Tag','str2'),'value')
971         if get(findobj(gcf,'Tag','isccheck'),'value')
972             set(findobj(gcf,'Tag','isc2'),'string',num2str(IL2*1000)
                    );
973         end
974         if get(findobj(gcf,'Tag','voccheck'),'value')
975             set(findobj(gcf,'Tag','voc2'),'string',num2str(Voc2));
976         end
977         if get(findobj(gcf,'Tag','effcheck'),'value')
978             set(findobj(gcf,'Tag','eff2'),'string',num2str(eff2));
979         end
980             if get(findobj(gcf,'Tag','effcheck'),'value')
981             set(findobj(gcf,'Tag','pout2'),'string',num2str(PMout2
                    *1000));
982         end
983
984     else
985         set(findobj(gcf,'Tag','isc2'),'string','N/A');
986         set(findobj(gcf,'Tag','voc2'),'string','N/A');
987         set(findobj(gcf,'Tag','eff2'),'string','N/A');
988         set(findobj(gcf,'Tag','pout2'),'string','N/A');
989
990     end
```

```
991
992 % --- Executes on button press in Type2.
993 function Type2_Callback(hObject, eventdata, handles)
994 % hObject    handle to Type2 (see GCBO)
995 % eventdata  reserved - to be defined in a future version of
    MATLAB
996 % handles    structure with handles and user data (see GUIDATA)
997
998 % Hint: get(hObject,'Value') returns toggle state of Type2
999 set(findobj(gcf,'Tag','Type12Pan'),'visible','on');
1000 set(findobj(gcf,'Tag','text17'),'string','Eg');
1001 set(findobj(gcf,'Tag','Eg'),'string','1.424');
1002 set(findobj(gcf,'Tag','Emin'),'visible','off');
1003 set(findobj(gcf,'Tag','Eminn'),'visible','off');
1004 set(findobj(gcf,'Tag','Estep'),'visible','off');
1005 set(findobj(gcf,'Tag','Estepp'),'visible','off');
1006 % --- Executes on button press in Type3.
1007 function Type3_Callback(hObject, eventdata, handles)
1008 % hObject    handle to Type3 (see GCBO)
1009 % eventdata  reserved - to be defined in a future version of
    MATLAB
1010 % handles    structure with handles and user data (see GUIDATA)
1011
1012 % Hint: get(hObject,'Value') returns toggle state of Type3
1013 set(findobj(gcf,'Tag','Type12Pan'),'visible','off');
1014 set(findobj(gcf,'Tag','text17'),'string','Emax');
1015 set(findobj(gcf,'Tag','Eg'),'string','2');
1016 set(findobj(gcf,'Tag','Emin'),'visible','on');
1017 set(findobj(gcf,'Tag','Eminn'),'visible','on');
1018 set(findobj(gcf,'Tag','Estep'),'visible','on');
1019 set(findobj(gcf,'Tag','Estepp'),'visible','on');
1020
1021 % --- Executes on button press in Type1.
1022 function Type1_Callback(hObject, eventdata, handles)
1023 % hObject    handle to Type1 (see GCBO)
1024 % eventdata  reserved - to be defined in a future version of
    MATLAB
1025 % handles    structure with handles and user data (see GUIDATA)
1026
1027 % Hint: get(hObject,'Value') returns toggle state of Type1
1028 set(findobj(gcf,'Tag','Type12Pan'),'visible','on');
1029 set(findobj(gcf,'Tag','text17'),'string','Eg');
1030 set(findobj(gcf,'Tag','Eg'),'string','1.424');
1031 set(findobj(gcf,'Tag','Emin'),'visible','off');
1032 set(findobj(gcf,'Tag','Eminn'),'visible','off');
1033 set(findobj(gcf,'Tag','Estep'),'visible','off');
1034 set(findobj(gcf,'Tag','Estepp'),'visible','off');
```

```
1035
1036
1037
1038 function edit17_Callback(hObject, eventdata, handles)
1039 % hObject    handle to edit17 (see GCBO)
1040 % eventdata  reserved - to be defined in a future version of
     MATLAB
1041 % handles    structure with handles and user data (see GUIDATA)
1042
1043 % Hints: get(hObject,'String') returns contents of edit17 as
     text
1044 %        str2double(get(hObject,'String')) returns contents of
     edit17 as a double
1045
1046
1047 % --- Executes during object creation, after setting all
     properties.
1048 function edit17_CreateFcn(hObject, eventdata, handles)
1049 % hObject    handle to edit17 (see GCBO)
1050 % eventdata  reserved - to be defined in a future version of
     MATLAB
1051 % handles    empty - handles not created until after all
     CreateFcns called
1052
1053 % Hint: edit controls usually have a white background on Windows
     .
1054 %       See ISPC and COMPUTER.
1055 if ispc && isequal(get(hObject,'BackgroundColor'), get(0,'
     defaultUicontrolBackgroundColor'))
1056     set(hObject,'BackgroundColor','white');
1057 end
1058
1059
1060 % --- Executes on button press in radiobutton17.
1061 function radiobutton17_Callback(hObject, eventdata, handles)
1062 % hObject    handle to radiobutton17 (see GCBO)
1063 % eventdata  reserved - to be defined in a future version of
     MATLAB
1064 % handles    structure with handles and user data (see GUIDATA)
1065
1066 % Hint: get(hObject,'Value') returns toggle state of
     radiobutton17
1067
1068
1069 % --- Executes during object creation, after setting all
     properties.
1070 function radiobutton18_CreateFcn(hObject, eventdata, handles)
```

```
1071 % hObject    handle to radiobutton18 (see GCBO)
1072 % eventdata  reserved - to be defined in a future version of
     MATLAB
1073 % handles    empty - handles not created until after all
     CreateFcns called
1074
1075
1076 % --- If Enable == 'on', executes on mouse press in 5 pixel
     border.
1077 % --- Otherwise, executes on mouse press in 5 pixel border or
     over radiobutton18.
1078 function radiobutton18_ButtonDownFcn(hObject, eventdata, handles
     )
1079 % hObject    handle to radiobutton18 (see GCBO)
1080 % eventdata  reserved - to be defined in a future version of
     MATLAB
1081 % handles    structure with handles and user data (see GUIDATA)
1082
1083
1084 % --- Executes on button press in Source2.
1085 function Source2_Callback(hObject, eventdata, handles)
1086 % hObject    handle to Source2 (see GCBO)
1087 % eventdata  reserved - to be defined in a future version of
     MATLAB
1088 % handles    structure with handles and user data (see GUIDATA)
1089
1090 % Hint: get(hObject,'Value') returns toggle state of Source2
1091 set(findobj(gcf,'Tag','AM'),'visible','on');
1092 set(findobj(gcf,'Tag','BBR1'),'visible','off');
1093 set(findobj(gcf,'Tag','BBR2'),'visible','off');
1094 set(findobj(gcf,'Tag','BBR3'),'visible','off');
1095 set(findobj(gcf,'Tag','pathratio'),'visible','off');
1096 set(findobj(gcf,'Tag','pathrr'),'visible','off');
1097
1098 % --- Executes on button press in Source1.
1099 function Source1_Callback(hObject, eventdata, handles)
1100 % hObject    handle to Source1 (see GCBO)
1101 % eventdata  reserved - to be defined in a future version of
     MATLAB
1102 % handles    structure with handles and user data (see GUIDATA)
1103
1104 % Hint: get(hObject,'Value') returns toggle state of Source1
1105 set(findobj(gcf,'Tag','AM'),'visible','off');
1106 set(findobj(gcf,'Tag','BBR1'),'visible','on');
1107 set(findobj(gcf,'Tag','BBR2'),'visible','on');
1108 set(findobj(gcf,'Tag','BBR3'),'visible','on');
1109 set(findobj(gcf,'Tag','pathratio'),'visible','on');
```

```
1110 set(findobj(gcf,'Tag','pathrr'),'visible','on');
1111
1112
1113
1114 function Eg_Callback(hObject, eventdata, handles)
1115 % hObject    handle to Eg (see GCBO)
1116 % eventdata  reserved - to be defined in a future version of
       MATLAB
1117 % handles    structure with handles and user data (see GUIDATA)
1118
1119 % Hints: get(hObject,'String') returns contents of Eg as text
1120 %        str2double(get(hObject,'String')) returns contents of
       Eg as a double
1121
1122
1123 % --- Executes during object creation, after setting all
       properties.
1124 function Eg_CreateFcn(hObject, eventdata, handles)
1125 % hObject    handle to Eg (see GCBO)
1126 % eventdata  reserved - to be defined in a future version of
       MATLAB
1127 % handles    empty - handles not created until after all
       CreateFcns called
1128
1129 % Hint: edit controls usually have a white background on Windows
       .
1130 %       See ISPC and COMPUTER.
1131 if ispc && isequal(get(hObject,'BackgroundColor'), get(0,'
       defaultUicontrolBackgroundColor'))
1132     set(hObject,'BackgroundColor','white');
1133 end
1134
1135
1136 % --- Executes on button press in pushbutton5.
1137 function pushbutton5_Callback(hObject, eventdata, handles)
1138 % hObject    handle to pushbutton5 (see GCBO)
1139 % eventdata  reserved - to be defined in a future version of
       MATLAB
1140 % handles    structure with handles and user data (see GUIDATA)
1141 set(gcf,'currentaxes',handles.axes1);
1142 cla reset;
1143 set(gcf,'currentaxes',handles.axes2);
1144 cla reset;
1145
1146
1147
1148 function Area_Callback(hObject, eventdata, handles)
```

```
1149 % hObject    handle to Area (see GCBO)
1150 % eventdata  reserved - to be defined in a future version of
     MATLAB
1151 % handles    structure with handles and user data (see GUIDATA)
1152
1153 % Hints: get(hObject,'String') returns contents of Area as text
1154 %        str2double(get(hObject,'String')) returns contents of
     Area as a double
1155
1156
1157 % --- Executes during object creation, after setting all
     properties.
1158 function Area_CreateFcn(hObject, eventdata, handles)
1159 % hObject    handle to Area (see GCBO)
1160 % eventdata  reserved - to be defined in a future version of
     MATLAB
1161 % handles    empty - handles not created until after all
     CreateFcns called
1162
1163 % Hint: edit controls usually have a white background on Windows
     .
1164 %       See ISPC and COMPUTER.
1165 if ispc && isequal(get(hObject,'BackgroundColor'), get(0,'
     defaultUicontrolBackgroundColor'))
1166     set(hObject,'BackgroundColor','white');
1167 end
1168
1169
1170
1171 function Width_Callback(hObject, eventdata, handles)
1172 % hObject    handle to Width (see GCBO)
1173 % eventdata  reserved - to be defined in a future version of
     MATLAB
1174 % handles    structure with handles and user data (see GUIDATA)
1175
1176 % Hints: get(hObject,'String') returns contents of Width as text
1177 %        str2double(get(hObject,'String')) returns contents of
     Width as a double
1178
1179
1180 % --- Executes during object creation, after setting all
     properties.
1181 function Width_CreateFcn(hObject, eventdata, handles)
1182 % hObject    handle to Width (see GCBO)
1183 % eventdata  reserved - to be defined in a future version of
     MATLAB
```

```
1184 % handles    empty - handles not created until after all
     CreateFcns called
1185
1186 % Hint: edit controls usually have a white background on Windows
     .
1187 %       See ISPC and COMPUTER.
1188 if ispc && isequal(get(hObject,'BackgroundColor'), get(0,'
     defaultUicontrolBackgroundColor'))
1189     set(hObject,'BackgroundColor','white');
1190 end
1191
1192
1193 % --- Executes during object creation, after setting all
     properties.
1194 function BBR1_CreateFcn(hObject, eventdata, handles)
1195 % hObject    handle to BBR1 (see GCBO)
1196 % eventdata  reserved - to be defined in a future version of
     MATLAB
1197 % handles    empty - handles not created until after all
     CreateFcns called
1198
1199
1200
1201 function Eminn_Callback(hObject, eventdata, handles)
1202 % hObject    handle to Eminn (see GCBO)
1203 % eventdata  reserved - to be defined in a future version of
     MATLAB
1204 % handles    structure with handles and user data (see GUIDATA)
1205
1206 % Hints: get(hObject,'String') returns contents of Eminn as text
1207 %        str2double(get(hObject,'String')) returns contents of
     Eminn as a double
1208
1209
1210 % --- Executes during object creation, after setting all
     properties.
1211 function Eminn_CreateFcn(hObject, eventdata, handles)
1212 % hObject    handle to Eminn (see GCBO)
1213 % eventdata  reserved - to be defined in a future version of
     MATLAB
1214 % handles    empty - handles not created until after all
     CreateFcns called
1215
1216 % Hint: edit controls usually have a white background on Windows
     .
1217 %       See ISPC and COMPUTER.
```

```
1218 if ispc && isequal(get(hObject,'BackgroundColor'), get(0,'
     defaultUicontrolBackgroundColor'))
1219     set(hObject,'BackgroundColor','white');
1220 end
1221
1222
1223
1224 function Estepp_Callback(hObject, eventdata, handles)
1225 % hObject    handle to Estepp (see GCBO)
1226 % eventdata  reserved - to be defined in a future version of
     MATLAB
1227 % handles    structure with handles and user data (see GUIDATA)
1228
1229 % Hints: get(hObject,'String') returns contents of Estepp as
     text
1230 %        str2double(get(hObject,'String')) returns contents of
     Estepp as a double
1231
1232
1233 % --- Executes during object creation, after setting all
     properties.
1234 function Estepp_CreateFcn(hObject, eventdata, handles)
1235 % hObject    handle to Estepp (see GCBO)
1236 % eventdata  reserved - to be defined in a future version of
     MATLAB
1237 % handles    empty - handles not created until after all
     CreateFcns called
1238
1239 % Hint: edit controls usually have a white background on Windows
     .
1240 %       See ISPC and COMPUTER.
1241 if ispc && isequal(get(hObject,'BackgroundColor'), get(0,'
     defaultUicontrolBackgroundColor'))
1242     set(hObject,'BackgroundColor','white');
1243 end
1244
1245
1246
1247 function nassume_Callback(hObject, eventdata, handles)
1248 % hObject    handle to nassume (see GCBO)
1249 % eventdata  reserved - to be defined in a future version of
     MATLAB
1250 % handles    structure with handles and user data (see GUIDATA)
1251
1252 % Hints: get(hObject,'String') returns contents of nassume as
     text
```

```
1253 %        str2double(get(hObject,'String')) returns contents of
     nassume as a double
1254
1255
1256 % --- Executes during object creation, after setting all
     properties.
1257 function nassume_CreateFcn(hObject, eventdata, handles)
1258 % hObject    handle to nassume (see GCBO)
1259 % eventdata  reserved - to be defined in a future version of
     MATLAB
1260 % handles    empty - handles not created until after all
     CreateFcns called
1261
1262 % Hint: edit controls usually have a white background on Windows
     .
1263 %       See ISPC and COMPUTER.
1264 if ispc && isequal(get(hObject,'BackgroundColor'), get(0,'
     defaultUicontrolBackgroundColor'))
1265     set(hObject,'BackgroundColor','white');
1266 end
1267
1268
1269 % --- Executes on button press in isccheck.
1270 function isccheck_Callback(hObject, eventdata, handles)
1271 % hObject    handle to isccheck (see GCBO)
1272 % eventdata  reserved - to be defined in a future version of
     MATLAB
1273 % handles    structure with handles and user data (see GUIDATA)
1274
1275 % Hint: get(hObject,'Value') returns toggle state of isccheck
1276 global IL1
1277 global IL2
1278 if get(findobj(gcf,'Tag','isccheck'),'value')
1279     if get(findobj(gcf,'Tag','str1'),'value')
1280     set(findobj(gcf,'Tag','isc1'),'string',num2str(max(IL1*1000)
         ));
1281     end
1282     if get(findobj(gcf,'Tag','str2'),'value')
1283     set(findobj(gcf,'Tag','isc2'),'string',num2str(max(IL2*1000)
         ));
1284     end
1285     if get(findobj(gcf,'Tag','str3'),'value')
1286     set(findobj(gcf,'Tag','isc3'),'string',num2str(max(IL1*1000)
         ));
1287     end
1288 else
1289     set(findobj(gcf,'Tag','isc1'),'string','N/A');
```

```
1290      set(findobj(gcf,'Tag','isc2'),'string','N/A');
1291      set(findobj(gcf,'Tag','isc3'),'string','N/A');
1292
1293  end
1294
1295
1296  % --- Executes on slider movement.
1297  function xslider_Callback(hObject, eventdata, handles)
1298  % hObject    handle to xslider (see GCBO)
1299  % eventdata  reserved - to be defined in a future version of
        MATLAB
1300  % handles    structure with handles and user data (see GUIDATA)
1301
1302  % Hints: get(hObject,'Value') returns position of slider
1303  %        get(hObject,'Min') and get(hObject,'Max') to determine
        range of slider
1304  minpos=str2double(get(findobj(gcf,'Tag','edit32'),'string'));
1305  maxpos=str2double(get(findobj(gcf,'Tag','edit33'),'string'));
1306
1307  midpos=get(findobj(gcf,'Tag','xslider'),'value')*(maxpos-minpos)
        +minpos;
1308  set(gca,'xlim',[str2double(get(findobj(gcf,'Tag','X1'),'string')
        )+midpos,str2double(get(findobj(gcf,'Tag','X2'),'string'))+
        midpos]);
1309
1310
1311  % --- Executes during object creation, after setting all
        properties.
1312  function xslider_CreateFcn(hObject, eventdata, handles)
1313  % hObject    handle to xslider (see GCBO)
1314  % eventdata  reserved - to be defined in a future version of
        MATLAB
1315  % handles    empty - handles not created until after all
        CreateFcns called
1316
1317  % Hint: slider controls usually have a light gray background.
1318  if isequal(get(hObject,'BackgroundColor'), get(0,'
        defaultUicontrolBackgroundColor'))
1319      set(hObject,'BackgroundColor',[.9 .9 .9]);
1320  end
1321
1322
1323  % --- Executes on slider movement.
1324  function ysilder_Callback(hObject, eventdata, handles)
1325  % hObject    handle to ysilder (see GCBO)
1326  % eventdata  reserved - to be defined in a future version of
        MATLAB
```

```
1327 % handles    structure with handles and user data (see GUIDATA)
1328
1329 % Hints: get(hObject,'Value') returns position of slider
1330 %        get(hObject,'Min') and get(hObject,'Max') to determine
         range of slider
1331 minpos=str2double(get(findobj(gcf,'Tag','edit34'),'string'));
1332 maxpos=str2double(get(findobj(gcf,'Tag','edit35'),'string'));
1333 midpos=get(findobj(gcf,'Tag','ysilder'),'value')*(maxpos-minpos)
         +minpos;
1334 set(gca,'ylim',[str2double(get(findobj(gcf,'Tag','Y1'),'string')
         )+midpos,str2double(get(findobj(gcf,'Tag','Y2'),'string'))+
         midpos]);
1335
1336
1337
1338
1339 % --- Executes during object creation, after setting all
         properties.
1340 function ysilder_CreateFcn(hObject, eventdata, handles)
1341 % hObject    handle to ysilder (see GCBO)
1342 % eventdata  reserved - to be defined in a future version of
         MATLAB
1343 % handles    empty - handles not created until after all
         CreateFcns called
1344
1345 % Hint: slider controls usually have a light gray background.
1346 if isequal(get(hObject,'BackgroundColor'), get(0,'
         defaultUicontrolBackgroundColor'))
1347     set(hObject,'BackgroundColor',[.9 .9 .9]);
1348 end
1349
1350
1351
1352 function angleemi_Callback(hObject, eventdata, handles)
1353 % hObject    handle to angleemi (see GCBO)
1354 % eventdata  reserved - to be defined in a future version of
         MATLAB
1355 % handles    structure with handles and user data (see GUIDATA)
1356
1357 % Hints: get(hObject,'String') returns contents of angleemi as
         text
1358 %        str2double(get(hObject,'String')) returns contents of
         angleemi as a double
1359
1360
1361 % --- Executes during object creation, after setting all
         properties.
```

```
1362 function angleemi_CreateFcn(hObject, eventdata, handles)
1363 % hObject    handle to angleemi (see GCBO)
1364 % eventdata  reserved - to be defined in a future version of
     MATLAB
1365 % handles    empty - handles not created until after all
     CreateFcns called
1366
1367 % Hint: edit controls usually have a white background on Windows
     .
1368 %       See ISPC and COMPUTER.
1369 if ispc && isequal(get(hObject,'BackgroundColor'), get(0,'
     defaultUicontrolBackgroundColor'))
1370     set(hObject,'BackgroundColor','white');
1371 end
1372
1373
1374
1375 function intqeff_Callback(hObject, eventdata, handles)
1376 % hObject    handle to intqeff (see GCBO)
1377 % eventdata  reserved - to be defined in a future version of
     MATLAB
1378 % handles    structure with handles and user data (see GUIDATA)
1379
1380 % Hints: get(hObject,'String') returns contents of intqeff as
     text
1381 %        str2double(get(hObject,'String')) returns contents of
     intqeff as a double
1382
1383
1384 % --- Executes during object creation, after setting all
     properties.
1385 function intqeff_CreateFcn(hObject, eventdata, handles)
1386 % hObject    handle to intqeff (see GCBO)
1387 % eventdata  reserved - to be defined in a future version of
     MATLAB
1388 % handles    empty - handles not created until after all
     CreateFcns called
1389
1390 % Hint: edit controls usually have a white background on Windows
     .
1391 %       See ISPC and COMPUTER.
1392 if ispc && isequal(get(hObject,'BackgroundColor'), get(0,'
     defaultUicontrolBackgroundColor'))
1393     set(hObject,'BackgroundColor','white');
1394 end
1395
1396
```

```
1397 %
     ------------------------------------------------------------------------

1398 function Untitled_1_Callback(hObject, eventdata, handles)
1399 % hObject    handle to Untitled_1 (see GCBO)
1400 % eventdata  reserved - to be defined in a future version of
     MATLAB
1401 % handles    structure with handles and user data (see GUIDATA)
1402
1403
1404 %
     ------------------------------------------------------------------------

1405 function Untitled_2_Callback(hObject, eventdata, handles)
1406 % hObject    handle to Untitled_2 (see GCBO)
1407 % eventdata  reserved - to be defined in a future version of
     MATLAB
1408 % handles    structure with handles and user data (see GUIDATA)
1409
1410
1411 %
     ------------------------------------------------------------------------

1412 function Untitled_3_Callback(hObject, eventdata, handles)
1413 % hObject    handle to Untitled_3 (see GCBO)
1414 % eventdata  reserved - to be defined in a future version of
     MATLAB
1415 % handles    structure with handles and user data (see GUIDATA)
1416
1417
1418 %
     ------------------------------------------------------------------------

1419 function Untitled_4_Callback(hObject, eventdata, handles)
1420 % hObject    handle to Untitled_4 (see GCBO)
1421 % eventdata  reserved - to be defined in a future version of
     MATLAB
1422 % handles    structure with handles and user data (see GUIDATA)
1423
1424
1425 %
     ------------------------------------------------------------------------

1426 function Untitled_5_Callback(hObject, eventdata, handles)
1427 % hObject    handle to Untitled_5 (see GCBO)
1428 % eventdata  reserved - to be defined in a future version of
     MATLAB
```

```
1429 % handles    structure with handles and user data (see GUIDATA)
1430 Output=['      All Rights Researved @ Munday Lab
                                        ';
1431          '      Institute of Researches in Electronics and Applied
                 Physics      ';
1432          '      University of Maryland, College Park, MD20740
                                ';
1433          '

              '];
1434 msgbox(Output,'Info');
1435
1436 %
     ------------------------------------------------------------------------


1437 function Untitled_7_Callback(hObject, eventdata, handles)
1438 % hObject    handle to Untitled_7 (see GCBO)
1439 % eventdata  reserved - to be defined in a future version of
    MATLAB
1440 % handles    structure with handles and user data (see GUIDATA)
1441 Output=['If you find any bugs, please email to : ylxu@umd.edu'];
1442 msgbox(Output,'Contact');
1443
1444
1445 % --- Executes on button press in pushbutton6.
1446 function pushbutton6_Callback(hObject, eventdata, handles)
1447 % hObject    handle to pushbutton6 (see GCBO)
1448 % eventdata  reserved - to be defined in a future version of
    MATLAB
1449 % handles    structure with handles and user data (see GUIDATA)
1450 Output=['   Sources:
                                                                    ,
1451          '      1.Black Body Radiation:  The source is an ideal
                 blackbody     '
1452          '           Type in (1)the blackbody temperature
                                ,
1453          '                      (2)the ratio of distance to
                 black body radius'
1454          '      2.AM1.5G: The source is defined by the user
                               ,
1455          '           Type in the power per unit area on the cell
                              ,
1456          '

              ,
1457          '   Format of Address
                                                                    ,
```

```
1458            '        diskname:\document(s) name...\filename.txt
                                                                  '
1459            '
                                                                    ,
1460            '   Format of material data:
                                                                    '
1461            '        Row1: Wavelength
                                                                    '
1462            '        Row2: Power per unit area per wavelength
                                                                  '
1463            '
                                                                    ,
1464            '   Path Enhancement:
                                                                    '
1465            '        This will bring a 4(n/sin(emission angle))^2
                    times enhancement'
1466            '        in calculating the path length
                                                                  '
1467            '
                                                                    ,
1468            '
                                                                    ,
1469            '
                                                                  '];
1470  msgbox(Output,'Source Selection Instruction');
1471
1472  % --- Executes on button press in pushbutton7.
1473  function pushbutton7_Callback(hObject, eventdata, handles)
1474  % hObject    handle to pushbutton7 (see GCBO)
1475  % eventdata  reserved - to be defined in a future version of
        MATLAB
1476  % handles    structure with handles and user data (see GUIDATA)
1477
1478
1479  % --- Executes on button press in pushbutton8.
1480  function pushbutton8_Callback(hObject, eventdata, handles)
1481  % hObject    handle to pushbutton8 (see GCBO)
1482  % eventdata  reserved - to be defined in a future version of
        MATLAB
1483  % handles    structure with handles and user data (see GUIDATA)
1484
1485
```

```
1486 % --- Executes on button press in pushbutton9.
1487 function pushbutton9_Callback(hObject, eventdata, handles)
1488 % hObject    handle to pushbutton9 (see GCBO)
1489 % eventdata  reserved - to be defined in a future version of
     MATLAB
1490 % handles    structure with handles and user data (see GUIDATA)
1491 Output=['    Types:                                                  ',
1492         '       1.Ideal: Consider 100% absorption                    ',
1493         '       2.Material: Consider absorption coefficient of
                materials    '
1494         '       3.Bandgap plot:solar cell efficiency vs bandgap
                of materials'
1495         '                          ideal absorption                  ',
1496         '
                ',
1497         '    Material data:                                          ',
1498         '       You need material data for type 1 and 2 in
                calculating Idark'
1499         '       Leave it as default if you want to calculate
                ideal case     '
1500         '
                ',
1501         '    Format of Address                                       ',
1502         '       diskname:\document(s) name...\filename.txt           ',
1503         '
                ',
1504         '    Format of material data:                                ',
1505         '       Row1: wavelength                                     ',
1506         '       Row2:Real Refractive Index,                          ',
1507         '       Row3:Imaginary Refractive Index                      ',
1508         '
                ',
```

```
1509            '
                    '
1510            '
                    '];
1511 msgbox(Output,'Type Selection Instruction');
1512
1513
1514
1515 function pathratio_Callback(hObject, eventdata, handles)
1516 % hObject    handle to pathratio (see GCBO)
1517 % eventdata  reserved - to be defined in a future version of
       MATLAB
1518 % handles    structure with handles and user data (see GUIDATA)
1519
1520 % Hints: get(hObject,'String') returns contents of pathratio as
       text
1521 %        str2double(get(hObject,'String')) returns contents of
       pathratio as a double
1522
1523
1524 %--- Executes during object creation, after setting all
       properties.
1525 function pathratio_CreateFcn(hObject, eventdata, handles)
1526 % hObject    handle to pathratio (see GCBO)
1527 % eventdata  reserved - to be defined in a future version of
       MATLAB
1528 % handles    empty - handles not created until after all
       CreateFcns called
1529
1530 % Hint: edit controls usually have a white background on Windows
       .
1531 %       See ISPC and COMPUTER.
1532 if ispc && isequal(get(hObject,'BackgroundColor'), get(0,'
       defaultUicontrolBackgroundColor'))
1533     set(hObject,'BackgroundColor','white');
1534 end
1535
1536
1537 %
       --------------------------------------------------------------------

1538 function Untitled_8_Callback(hObject, eventdata, handles)
1539 % hObject    handle to Untitled_8 (see GCBO)
1540 % eventdata  reserved - to be defined in a future version of
       MATLAB
```

```
% handles    structure with handles and user data (see GUIDATA)
if get(findobj(gcf,'Tag','Type3'),'value')
    rownum=1;
    fid=fopen(get(findobj(gcf,'Tag','edit28'),'string'),'wt');
    fprintf(fid,'%20s','Bandgap(eV)');
    if get(findobj(gcf,'Tag','str1'),'value')
        global eff1;
        fprintf(fid,'%20s','eff_str1');
        rownum=rownum+1;
    else
        eff1=[];
    end
    if get(findobj(gcf,'Tag','str2'),'value')
        global eff2;
        fprintf(fid,'%20s','eff_str2');
        rownum=rownum+1;
    else
        eff2=[];
    end
    if get(findobj(gcf,'Tag','str3'),'value')
        global eff3;
        fprintf(fid,'%20s','eff_str3');
        rownum=rownum+1;
    else
        eff3=[];
    end

    Estart=str2double(get(findobj(gcf,'Tag','Eminn'),'string'));
    Eg00=str2double(get(findobj(gcf,'Tag','Eg'),'string'));
    Estepp=str2double(get(findobj(gcf,'Tag','Estepp'),'string'))
        ;
    Eband=Estart:Estepp:Eg00;
    Output=[Eband',eff1,eff2,eff3];
    size(Output)

    fprintf(fid,'\n');
    for i=1:length(Output)
        for j=1:rownum
            fprintf(fid,'%20d',Output(i,j));
        end
        fprintf(fid,'\n');
    end
    fclose(fid);

else
    rownum=1;
    fid=fopen(get(findobj(gcf,'Tag','edit28'),'string'),'wt');
```

```
1587        fprintf(fid,'%20s','Voltage(V)');
1588        if get(findobj(gcf,'Tag','str1'),'value')
1589            global I_s1;
1590            fprintf(fid,'%20s','I_s1(A/m^2)');
1591            rownum=rownum+1;
1592        else
1593            I_s1=[];
1594        end
1595        if get(findobj(gcf,'Tag','str2'),'value')
1596            global I_s2;
1597            fprintf(fid,'%20s','I_s2(A/m^2)');
1598            rownum=rownum+1;
1599        else
1600            I_s2=[];
1601        end
1602        if get(findobj(gcf,'Tag','str3'),'value')
1603            global I_s3;
1604            fprintf(fid,'%20s','I_s3(A/m^2)');
1605            rownum=rownum+1;
1606        else
1607            I_s3=[];
1608        end
1609
1610        global Voltage;
1611        Output=[Voltage',I_s1',I_s2',I_s3'];
1612        fprintf(fid,'\n');
1613        for i=1:length(Output)
1614            for j=1:rownum
1615                fprintf(fid,'%20d',Output(i,j));
1616            end
1617            fprintf(fid,'\n');
1618        end
1619        fclose(fid);
1620    end
1621
1622
1623    function edit28_Callback(hObject, eventdata, handles)
1624    % hObject    handle to edit28 (see GCBO)
1625    % eventdata  reserved - to be defined in a future version of
        MATLAB
1626    % handles    structure with handles and user data (see GUIDATA)
1627
1628    % Hints: get(hObject,'String') returns contents of edit28 as
        text
1629    %        str2double(get(hObject,'String')) returns contents of
        edit28 as a double
1630
```

```
1631
1632 % --- Executes during object creation, after setting all
     properties.
1633 function edit28_CreateFcn(hObject, eventdata, handles)
1634 % hObject    handle to edit28 (see GCBO)
1635 % eventdata  reserved - to be defined in a future version of
     MATLAB
1636 % handles    empty - handles not created until after all
     CreateFcns called
1637
1638 % Hint: edit controls usually have a white background on Windows
     .
1639 %       See ISPC and COMPUTER.
1640 if ispc && isequal(get(hObject,'BackgroundColor'), get(0,'
     defaultUicontrolBackgroundColor'))
1641     set(hObject,'BackgroundColor','white');
1642 end
1643
1644
1645 % --- Executes on button press in pushbutton10.
1646 function pushbutton10_Callback(hObject, eventdata, handles)
1647 % hObject    handle to pushbutton10 (see GCBO)
1648 % eventdata  reserved - to be defined in a future version of
     MATLAB
1649 % handles    structure with handles and user data (see GUIDATA)
1650 if get(findobj(gcf,'Tag','Type3'),'value')
1651     rownum=1;
1652     fid=fopen(get(findobj(gcf,'Tag','edit28'),'string'),'wt');
1653     fprintf(fid,'%20s','Bandgap(eV)');
1654     if get(findobj(gcf,'Tag','str1'),'value')
1655         global eff1;
1656         fprintf(fid,'%20s','eff_str1');
1657         rownum=rownum+1;
1658     else
1659         eff1=[];
1660     end
1661     if get(findobj(gcf,'Tag','str2'),'value')
1662         global eff2;
1663         fprintf(fid,'%20s','eff_str2');
1664         rownum=rownum+1;
1665     else
1666         eff2=[];
1667     end
1668     if get(findobj(gcf,'Tag','str3'),'value')
1669         global eff3;
1670         fprintf(fid,'%20s','eff_str3');
1671         rownum=rownum+1;
```

```
1672        else
1673            eff3 = [];
1674        end
1675
1676        Estart=str2double(get(findobj(gcf,'Tag','Eminn'),'string'));
1677        Eg00=str2double(get(findobj(gcf,'Tag','Eg'),'string'));
1678        Estepp=str2double(get(findobj(gcf,'Tag','Estepp'),'string'))
                ;
1679        Eband=Estart:Estepp:Eg00;
1680        Output=[Eband',eff1,eff2,eff3];
1681        size(Output)
1682
1683        fprintf(fid,'\n');
1684        for i=1:length(Output)
1685            for j=1:rownum
1686                fprintf(fid,'%20d',Output(i,j));
1687            end
1688            fprintf(fid,'\n');
1689        end
1690        fclose(fid);
1691
1692    else
1693        rownum=1;
1694        fid=fopen(get(findobj(gcf,'Tag','edit28'),'string'),'wt');
1695        fprintf(fid,'%20s','Voltage(V)');
1696        if get(findobj(gcf,'Tag','str1'),'value')
1697            global I_s1;
1698            fprintf(fid,'%20s','I_s1(A/m^2)');
1699            rownum=rownum+1;
1700        else
1701            I_s1 = [];
1702        end
1703        if get(findobj(gcf,'Tag','str2'),'value')
1704            global I_s2;
1705            fprintf(fid,'%20s','I_s2(A/m^2)');
1706            rownum=rownum+1;
1707        else
1708            I_s2 = [];
1709        end
1710        if get(findobj(gcf,'Tag','str3'),'value')
1711            global I_s3;
1712            fprintf(fid,'%20s','I_s3(A/m^2)');
1713            rownum=rownum+1;
1714        else
1715            I_s3 = [];
1716        end
1717
```

```
1718        global Voltage;
1719        Output=[Voltage',I_s1',I_s2',I_s3'];
1720        fprintf(fid,'\n');
1721        for i=1:length(Output)
1722            for j=1:rownum
1723                fprintf(fid,'%20d',Output(i,j));
1724            end
1725            fprintf(fid,'\n');
1726        end
1727        fclose(fid);
1728    end
1729
1730
1731
1732
1733    function edit29_Callback(hObject, eventdata, handles)
1734    % hObject    handle to edit29 (see GCBO)
1735    % eventdata  reserved - to be defined in a future version of
        MATLAB
1736    % handles    structure with handles and user data (see GUIDATA)
1737
1738    % Hints: get(hObject,'String') returns contents of edit29 as
        text
1739    %        str2double(get(hObject,'String')) returns contents of
        edit29 as a double
1740
1741
1742    % --- Executes during object creation, after setting all
        properties.
1743    function edit29_CreateFcn(hObject, eventdata, handles)
1744    % hObject    handle to edit29 (see GCBO)
1745    % eventdata  reserved - to be defined in a future version of
        MATLAB
1746    % handles    empty - handles not created until after all
        CreateFcns called
1747
1748    % Hint: edit controls usually have a white background on Windows
        .
1749    %       See ISPC and COMPUTER.
1750    if ispc && isequal(get(hObject,'BackgroundColor'), get(0,'
        defaultUicontrolBackgroundColor'))
1751        set(hObject,'BackgroundColor','white');
1752    end
1753
1754
1755
1756    function edit30_Callback(hObject, eventdata, handles)
```

```
1757 % hObject    handle to edit30 (see GCBO)
1758 % eventdata  reserved - to be defined in a future version of
     MATLAB
1759 % handles    structure with handles and user data (see GUIDATA)
1760
1761 % Hints: get(hObject,'String') returns contents of edit30 as
     text
1762 %        str2double(get(hObject,'String')) returns contents of
     edit30 as a double
1763
1764
1765 % --- Executes during object creation, after setting all
     properties.
1766 function edit30_CreateFcn(hObject, eventdata, handles)
1767 % hObject    handle to edit30 (see GCBO)
1768 % eventdata  reserved - to be defined in a future version of
     MATLAB
1769 % handles    empty - handles not created until after all
     CreateFcns called
1770
1771 % Hint: edit controls usually have a white background on Windows
     .
1772 %       See ISPC and COMPUTER.
1773 if ispc && isequal(get(hObject,'BackgroundColor'), get(0,'
     defaultUicontrolBackgroundColor'))
1774     set(hObject,'BackgroundColor','white');
1775 end
1776
1777
1778
1779 function edit31_Callback(hObject, eventdata, handles)
1780 % hObject    handle to edit31 (see GCBO)
1781 % eventdata  reserved - to be defined in a future version of
     MATLAB
1782 % handles    structure with handles and user data (see GUIDATA)
1783
1784 % Hints: get(hObject,'String') returns contents of edit31 as
     text
1785 %        str2double(get(hObject,'String')) returns contents of
     edit31 as a double
1786
1787
1788 % --- Executes during object creation, after setting all
     properties.
1789 function edit31_CreateFcn(hObject, eventdata, handles)
1790 % hObject    handle to edit31 (see GCBO)
```

```
1791 % eventdata  reserved - to be defined in a future version of
     MATLAB
1792 % handles    empty - handles not created until after all
     CreateFcns called
1793
1794 % Hint: edit controls usually have a white background on Windows
     .
1795 %       See ISPC and COMPUTER.
1796 if ispc && isequal(get(hObject,'BackgroundColor'), get(0,'
     defaultUicontrolBackgroundColor'))
1797     set(hObject,'BackgroundColor','white');
1798 end
1799
1800
1801
1802 function edit32_Callback(hObject, eventdata, handles)
1803 % hObject    handle to edit32 (see GCBO)
1804 % eventdata  reserved - to be defined in a future version of
     MATLAB
1805 % handles    structure with handles and user data (see GUIDATA)
1806
1807 % Hints: get(hObject,'String') returns contents of edit32 as
     text
1808 %        str2double(get(hObject,'String')) returns contents of
     edit32 as a double
1809
1810
1811 % --- Executes during object creation, after setting all
     properties.
1812 function edit32_CreateFcn(hObject, eventdata, handles)
1813 % hObject    handle to edit32 (see GCBO)
1814 % eventdata  reserved - to be defined in a future version of
     MATLAB
1815 % handles    empty - handles not created until after all
     CreateFcns called
1816
1817 % Hint: edit controls usually have a white background on Windows
     .
1818 %       See ISPC and COMPUTER.
1819 if ispc && isequal(get(hObject,'BackgroundColor'), get(0,'
     defaultUicontrolBackgroundColor'))
1820     set(hObject,'BackgroundColor','white');
1821 end
1822
1823
1824
1825 function edit33_Callback(hObject, eventdata, handles)
```

```
1826 % hObject    handle to edit33 (see GCBO)
1827 % eventdata  reserved - to be defined in a future version of
     MATLAB
1828 % handles    structure with handles and user data (see GUIDATA)
1829
1830 % Hints: get(hObject,'String') returns contents of edit33 as
     text
1831 %        str2double(get(hObject,'String')) returns contents of
     edit33 as a double
1832
1833
1834 % --- Executes during object creation, after setting all
     properties.
1835 function edit33_CreateFcn(hObject, eventdata, handles)
1836 % hObject    handle to edit33 (see GCBO)
1837 % eventdata  reserved - to be defined in a future version of
     MATLAB
1838 % handles    empty - handles not created until after all
     CreateFcns called
1839
1840 % Hint: edit controls usually have a white background on Windows
     .
1841 %       See ISPC and COMPUTER.
1842 if ispc && isequal(get(hObject,'BackgroundColor'), get(0,'
     defaultUicontrolBackgroundColor'))
1843     set(hObject,'BackgroundColor','white');
1844 end
1845
1846
1847
1848 function edit34_Callback(hObject, eventdata, handles)
1849 % hObject    handle to edit34 (see GCBO)
1850 % eventdata  reserved - to be defined in a future version of
     MATLAB
1851 % handles    structure with handles and user data (see GUIDATA)
1852
1853 % Hints: get(hObject,'String') returns contents of edit34 as
     text
1854 %        str2double(get(hObject,'String')) returns contents of
     edit34 as a double
1855
1856
1857 % --- Executes during object creation, after setting all
     properties.
1858 function edit34_CreateFcn(hObject, eventdata, handles)
1859 % hObject    handle to edit34 (see GCBO)
```

```
1860 % eventdata  reserved - to be defined in a future version of
     MATLAB
1861 % handles    empty - handles not created until after all
     CreateFcns called
1862
1863 % Hint: edit controls usually have a white background on Windows
     .
1864 %       See ISPC and COMPUTER.
1865 if ispc && isequal(get(hObject,'BackgroundColor'), get(0,'
     defaultUicontrolBackgroundColor'))
1866     set(hObject,'BackgroundColor','white');
1867 end
1868
1869
1870
1871 function edit35_Callback(hObject, eventdata, handles)
1872 % hObject    handle to edit35 (see GCBO)
1873 % eventdata  reserved - to be defined in a future version of
     MATLAB
1874 % handles    structure with handles and user data (see GUIDATA)
1875
1876 % Hints: get(hObject,'String') returns contents of edit35 as
     text
1877 %        str2double(get(hObject,'String')) returns contents of
     edit35 as a double
1878
1879
1880 % --- Executes during object creation, after setting all
     properties.
1881 function edit35_CreateFcn(hObject, eventdata, handles)
1882 % hObject    handle to edit35 (see GCBO)
1883 % eventdata  reserved - to be defined in a future version of
     MATLAB
1884 % handles    empty - handles not created until after all
     CreateFcns called
1885
1886 % Hint: edit controls usually have a white background on Windows
     .
1887 %       See ISPC and COMPUTER.
1888 if ispc && isequal(get(hObject,'BackgroundColor'), get(0,'
     defaultUicontrolBackgroundColor'))
1889     set(hObject,'BackgroundColor','white');
1890 end
1891
1892
1893 % --- Executes on button press in MulC.
1894 function MulC_Callback(hObject, eventdata, handles)
```

```
1895 % hObject    handle to MulC (see GCBO)
1896 % eventdata  reserved - to be defined in a future version of
     MATLAB
1897 % handles    structure with handles and user data (see GUIDATA)
1898
1899 % Hint: get(hObject,'Value') returns toggle state of MulC
1900
1901
1902
1903 function edit36_Callback(hObject, eventdata, handles)
1904 % hObject    handle to edit36 (see GCBO)
1905 % eventdata  reserved - to be defined in a future version of
     MATLAB
1906 % handles    structure with handles and user data (see GUIDATA)
1907
1908 % Hints: get(hObject,'String') returns contents of edit36 as
     text
1909 %        str2double(get(hObject,'String')) returns contents of
     edit36 as a double
1910
1911
1912 % --- Executes during object creation, after setting all
     properties.
1913 function edit36_CreateFcn(hObject, eventdata, handles)
1914 % hObject    handle to edit36 (see GCBO)
1915 % eventdata  reserved - to be defined in a future version of
     MATLAB
1916 % handles    empty - handles not created until after all
     CreateFcns called
1917
1918 % Hint: edit controls usually have a white background on Windows
     .
1919 %       See ISPC and COMPUTER.
1920 if ispc && isequal(get(hObject,'BackgroundColor'), get(0,'
     defaultUicontrolBackgroundColor'))
1921     set(hObject,'BackgroundColor','white');
1922 end
1923
1924
1925 % --- Executes on button press in pushbutton11.
1926 function pushbutton11_Callback(hObject, eventdata, handles)
1927 % hObject    handle to pushbutton11 (see GCBO)
1928 % eventdata  reserved - to be defined in a future version of
     MATLAB
1929 % handles    structure with handles and user data (see GUIDATA)
1930
1931
```

```
1932 % --- Executes on button press in checkbox15.
1933 function checkbox15_Callback(hObject, eventdata, handles)
1934 % hObject    handle to checkbox15 (see GCBO)
1935 % eventdata  reserved - to be defined in a future version of
     MATLAB
1936 % handles    structure with handles and user data (see GUIDATA)
1937
1938 % Hint: get(hObject,'Value') returns toggle state of checkbox15
1939
1940
1941
1942 function splitmax_Callback(hObject, eventdata, handles)
1943 % hObject    handle to splitmax (see GCBO)
1944 % eventdata  reserved - to be defined in a future version of
     MATLAB
1945 % handles    structure with handles and user data (see GUIDATA)
1946
1947 % Hints: get(hObject,'String') returns contents of splitmax as
     text
1948 %        str2double(get(hObject,'String')) returns contents of
     splitmax as a double
1949
1950
1951 % --- Executes during object creation, after setting all
     properties.
1952 function splitmax_CreateFcn(hObject, eventdata, handles)
1953 % hObject    handle to splitmax (see GCBO)
1954 % eventdata  reserved - to be defined in a future version of
     MATLAB
1955 % handles    empty - handles not created until after all
     CreateFcns called
1956
1957 % Hint: edit controls usually have a white background on Windows
     .
1958 %       See ISPC and COMPUTER.
1959 if ispc && isequal(get(hObject,'BackgroundColor'), get(0,'
     defaultUicontrolBackgroundColor'))
1960     set(hObject,'BackgroundColor','white');
1961 end
1962
1963
1964
1965 function splitmin_Callback(hObject, eventdata, handles)
1966 % hObject    handle to splitmin (see GCBO)
1967 % eventdata  reserved - to be defined in a future version of
     MATLAB
1968 % handles    structure with handles and user data (see GUIDATA)
```

```
1969
1970 % Hints: get(hObject,'String') returns contents of splitmin as
     text
1971 %        str2double(get(hObject,'String')) returns contents of
     splitmin as a double
1972
1973
1974 % --- Executes during object creation, after setting all
     properties.
1975 function splitmin_CreateFcn(hObject, eventdata, handles)
1976 % hObject    handle to splitmin (see GCBO)
1977 % eventdata  reserved - to be defined in a future version of
     MATLAB
1978 % handles    empty - handles not created until after all
     CreateFcns called
1979
1980 % Hint: edit controls usually have a white background on Windows
     .
1981 %       See ISPC and COMPUTER.
1982 if ispc && isequal(get(hObject,'BackgroundColor'), get(0,'
     defaultUicontrolBackgroundColor'))
1983     set(hObject,'BackgroundColor','white');
1984 end
1985
1986
1987 % --- Executes on button press in PCs.
1988 function PCs_Callback(hObject, eventdata, handles)
1989 % hObject    handle to PCs (see GCBO)
1990 % eventdata  reserved - to be defined in a future version of
     MATLAB
1991 % handles    structure with handles and user data (see GUIDATA)
1992
1993 % Hint: get(hObject,'Value') returns toggle state of PCs
1994
1995
1996 % --- Executes on button press in poutcheck.
1997 function poutcheck_Callback(hObject, eventdata, handles)
1998 % hObject    handle to poutcheck (see GCBO)
1999 % eventdata  reserved - to be defined in a future version of
     MATLAB
2000 % handles    structure with handles and user data (see GUIDATA)
2001
2002 % Hint: get(hObject,'Value') returns toggle state of poutcheck
2003 global PMout1
2004 global PMout2
2005 global PMout3
2006 if get(findobj(gcf,'Tag','poutcheck'),'value')
```

```
2007        if get(findobj(gcf,'Tag','str1'),'value')
2008        set(findobj(gcf,'Tag','pout1'),'string',num2str(PMout1*1000)
                );
2009        end
2010        if get(findobj(gcf,'Tag','str2'),'value')
2011        set(findobj(gcf,'Tag','pout2'),'string',num2str(PMout2*1000)
                );
2012        end
2013        if get(findobj(gcf,'Tag','str3'),'value')
2014        set(findobj(gcf,'Tag','pout3'),'string',num2str(PMout3*1000)
                );
2015        end
2016    else
2017        set(findobj(gcf,'Tag','pout1'),'string','N/A');
2018        set(findobj(gcf,'Tag','pout2'),'string','N/A');
2019        set(findobj(gcf,'Tag','pout3'),'string','N/A');
2020
2021    end
2022
2023
2024
2025    function PCEpc_Callback(hObject, eventdata, handles)
2026    % hObject    handle to PCEpc (see GCBO)
2027    % eventdata  reserved - to be defined in a future version of
            MATLAB
2028    % handles    structure with handles and user data (see GUIDATA)
2029
2030    % Hints: get(hObject,'String') returns contents of PCEpc as text
2031    %        str2double(get(hObject,'String')) returns contents of
            PCEpc as a double
2032
2033
2034    %--- Executes during object creation, after setting all
            properties.
2035    function PCEpc_CreateFcn(hObject, eventdata, handles)
2036    % hObject    handle to PCEpc (see GCBO)
2037    % eventdata  reserved - to be defined in a future version of
            MATLAB
2038    % handles    empty - handles not created until after all
            CreateFcns called
2039
2040    % Hint: edit controls usually have a white background on Windows
            .
2041    %       See ISPC and COMPUTER.
2042    if ispc && isequal(get(hObject,'BackgroundColor'), get(0,'
            defaultUicontrolBackgroundColor'))
2043        set(hObject,'BackgroundColor','white');
```

```
2044 end
2045
2046
2047 % --- Executes on button press in checkbox18.
2048 function checkbox18_Callback(hObject, eventdata, handles)
2049 % hObject    handle to checkbox18 (see GCBO)
2050 % eventdata  reserved - to be defined in a future version of
       MATLAB
2051 % handles    structure with handles and user data (see GUIDATA)
2052
2053 % Hint: get(hObject,'Value') returns toggle state of checkbox18
2054
2055
2056
2057 function edit41_Callback(hObject, eventdata, handles)
2058 % hObject    handle to edit41 (see GCBO)
2059 % eventdata  reserved - to be defined in a future version of
       MATLAB
2060 % handles    structure with handles and user data (see GUIDATA)
2061
2062 % Hints: get(hObject,'String') returns contents of edit41 as
       text
2063 %        str2double(get(hObject,'String')) returns contents of
       edit41 as a double
2064
2065
2066 % --- Executes during object creation, after setting all
       properties.
2067 function edit41_CreateFcn(hObject, eventdata, handles)
2068 % hObject    handle to edit41 (see GCBO)
2069 % eventdata  reserved - to be defined in a future version of
       MATLAB
2070 % handles    empty - handles not created until after all
       CreateFcns called
2071
2072 % Hint: edit controls usually have a white background on Windows
       .
2073 %       See ISPC and COMPUTER.
2074 if ispc && isequal(get(hObject,'BackgroundColor'), get(0,'
       defaultUicontrolBackgroundColor'))
2075     set(hObject,'BackgroundColor','white');
2076 end
2077
2078
2079 % --- Executes on button press in Absmod.
2080 function Absmod_Callback(hObject, eventdata, handles)
2081 % hObject    handle to Absmod (see GCBO)
```

```
2082 % eventdata  reserved - to be defined in a future version of
     MATLAB
2083 % handles    structure with handles and user data (see GUIDATA)
2084
2085 % Hint: get(hObject,'Value') returns toggle state of Absmod
2086
2087
2088 % --- Executes on button press in PCsADD.
2089 function PCsADD_Callback(hObject, eventdata, handles)
2090 % hObject    handle to PCsADD (see GCBO)
2091 % eventdata  reserved - to be defined in a future version of
     MATLAB
2092 % handles    structure with handles and user data (see GUIDATA)
2093
2094 % Hint: get(hObject,'Value') returns toggle state of PCsADD
2095
2096
2097 % --- Executes during object creation, after setting all
     properties.
2098 function isc1_CreateFcn(hObject, eventdata, handles)
2099 % hObject    handle to isc1 (see GCBO)
2100 % eventdata  reserved - to be defined in a future version of
     MATLAB
2101 % handles    empty - handles not created until after all
     CreateFcns called
2102
2103
2104
2105 function edit44_Callback(hObject, eventdata, handles)
2106 % hObject    handle to edit44 (see GCBO)
2107 % eventdata  reserved - to be defined in a future version of
     MATLAB
2108 % handles    structure with handles and user data (see GUIDATA)
2109
2110 % Hints: get(hObject,'String') returns contents of edit44 as
     text
2111 %        str2double(get(hObject,'String')) returns contents of
     edit44 as a double
2112
2113
2114 % --- Executes during object creation, after setting all
     properties.
2115 function edit44_CreateFcn(hObject, eventdata, handles)
2116 % hObject    handle to edit44 (see GCBO)
2117 % eventdata  reserved - to be defined in a future version of
     MATLAB
```

```
2118 % handles    empty - handles not created until after all
     CreateFcns called
2119
2120 % Hint: edit controls usually have a white background on Windows
     .
2121 %       See ISPC and COMPUTER.
2122 if ispc && isequal(get(hObject,'BackgroundColor'), get(0,'
     defaultUicontrolBackgroundColor'))
2123     set(hObject,'BackgroundColor','white');
2124 end
2125
2126
2127 % --- Executes on button press in pushbutton12.
2128 function pushbutton12_Callback(hObject, eventdata, handles)
2129 % hObject    handle to pushbutton12 (see GCBO)
2130 % eventdata  reserved - to be defined in a future version of
     MATLAB
2131 % handles    structure with handles and user data (see GUIDATA)
2132 global Voltage;
2133 global I_s1;
2134 global I_s2;
2135 global I_s3;
2136 global PMout1;
2137 global PMout2;
2138 global PMout3;
2139 global Voc1
2140 global Voc2
2141 global Voc3
2142 fid=fopen(get(findobj(gcf,'Tag','edit28'),'string'),'wt');
2143 for i=1:length(Voltage)
2144
2145 fprintf(fid,'%20s',[num2str(I_s1(i)),',']);
2146 fprintf(fid,'%20s',[num2str(I_s2(i)),',']);
2147 fprintf(fid,'%20s',[num2str(I_s3(i)),',']);
2148 fprintf(fid,'%20s',num2str(Voltage(i)));
2149 fprintf(fid,'\n');
2150
2151 end
2152
2153
2154
2155 function edit45_Callback(hObject, eventdata, handles)
2156 % hObject    handle to edit45 (see GCBO)
2157 % eventdata  reserved - to be defined in a future version of
     MATLAB
2158 % handles    structure with handles and user data (see GUIDATA)
2159
```

```
2160 % Hints: get(hObject,'String') returns contents of edit45 as
     text
2161 %        str2double(get(hObject,'String')) returns contents of
     edit45 as a double
2162
2163
2164 % --- Executes during object creation, after setting all
     properties.
2165 function edit45_CreateFcn(hObject, eventdata, handles)
2166 % hObject    handle to edit45 (see GCBO)
2167 % eventdata  reserved - to be defined in a future version of
     MATLAB
2168 % handles    empty - handles not created until after all
     CreateFcns called
2169
2170 % Hint: edit controls usually have a white background on Windows
     .
2171 %       See ISPC and COMPUTER.
2172 if ispc && isequal(get(hObject,'BackgroundColor'), get(0,'
     defaultUicontrolBackgroundColor'))
2173     set(hObject,'BackgroundColor','white');
2174 end
```

Bibliography

[1] International Energy Outlook 2016, U.S. Energy Information Administration (2016)

[2] BP Energy Outlook 2035, BP Global (2014)

[3] W. Shockley, The theory of p-n junctions in semiconductors and p-n junction transistors. *Bell Syst. Tech. J.* **28**, 435 (1949).

[4] J. P. McKelvey, Solid state and semiconductor physics (Harper & Row), New York, (1966)

[5] W. Shockley and H. J. Queisser, Detailed balance limit of efficiency of p-n junction solar cells. *J. Appl. Phys.* **32**, 510 (1961)

[6] A. Marti, J. L. Balenzategui and R. F.Reyna, Photon recycling and Shockley's diode equation. *J. Appl. Phys.* **82**, 4067 (1997)

[7] P. Wurfel, S. Finkbeiner and E. Daub, Generalized Planck's radiation law for luminescence via indirect transitions. *A. Phys. A* **60**, 67(1995)

[8] A. Luque, S. Hegedus, Handbook of Photovoltaic Science and Engineering, *John Wiley and Sons*, United Kingdom (2011)

[9] M. Wolf and H. Rauschenbach, Series resistance effects on solar cell measurements , *Advanced Energy Conversion* **3**, 455(1963)

[10] H. Mullejans et al., Reliability of the routine 2-diode model fitting of PV modules, *Proceedings 19th European Photovoltaic Solar Energy Conference* 2459 (2004)

[11] S. P. Tobin, S. M. Vernon, C. Bajgar, S. J. Wojtczuk, M. R. Melloch, A. Keshavarzi, T. B. Stellwag, S. Venkatensan, M. S. Lundstrom and K. A. Emery, Assessment of MOCVD- and MBE-grown GaAs for highefficiency solar cell applications, *IEEE Trans. Electron Devices* **37(2)**, 469–477. (1990)

[12] M. T. Sheldon, C. N. Eisler and H. A. Atwater, GaAs passivation with trioctylphosphine sulde for enhanced solar cell efficiency and durability, *Adv. Energy Mater.* **2(3)**, 339–344 (2012)

[13] H. A. Macleod, Thin Film Optical Filters. (Institute of Physics, 2001).

[14] J. S. Rayleigh, On reflection of vibrations at the confines of two media between which the transition is gradual, *Proc. London Math. Soc.* **11**, 51–56 (1880).

[15] W. H. Southwell, Gradient-index antireflection coatings, *Opt. Lett.* **8**, 584–586 (1983).

[16] D. Poitras and J. A. Dobrowolski, Toward Perfect Antireflection Coatings. 2. Theory, *Appl. Opt.* **43**, 1286–1295 (2004).

[17] J. Q. Xi, et al. Optical thin-film materials with low refractive index for broadband elimination of Fresnel reflection, *Nat. Photon.* **1**, 176–179 (2007).

[18] S. J. Wilson and M. C. Hutley, The Optical Properties of 'Moth Eye' Antireflection Surfaces. *Optica Acta: International Journal of Optics* **29**, 993−1009 (1982).

[19] S. A. Maier, Plasmonics: Fundamentals and Applications. (Springer, 2007).

[20] H. A. Atwater and A. Polman, Plasmonics for improved photovoltaic devices, *Nat. Mater.* **9**, 205–213 (2010).

[21] V. E. Ferry, J. N. Munday and H. A. Atwater, Design Considerations for Plasmonic Photovoltaics, *Adv. Mater.* **22**, 4794–4808 (2010).

[22] S. Mokkapati and K. R. Catchpole, Nanophotonic light trapping in solar cells, *J. Appl. Phys.* **112**, 101101–19 (2012)

[23] H. R. Stuart and D. G. Hall, Absorption enhancement in silicon-on-insulator waveguides using metal island films, *Appl. Phys. Lett.* **69**, 2327–2329 (1996).

[24] C. F. Bohren and D. R. Huffman, Absorption and scattering of light by small particles, *Wiley Science Editions*, 1983.

[25] P. Spinelli, M. A. Verschuuren and A. Polman, Broadband omnidirectional antireflection coating based on subwavelength surface Mie resonators, *Nat. Commun.* **3**, 692 (2012).

[26] D. Pacifici, H. J. Lezec and H. A. Atwater, All-optical modulation by plasmonic excitation of CdSe quantum dots, *Nat. Photon.* **1**, 402−406 (2007).

[27] C. J. Brabec, Organic photovoltaics: technology and market, *Sol. Energy Mater. Sol. Cells* **83(2-3)**, 273-292 (2004).

[28] F. C. Krebs, S. A. Gevorgyan, and J. Alstrup, A roll-to-roll process to flexible polymer solar cells: model studies, manufacture and operational stability studies, *J. Mater. Chem.* **19(30)**, 5442 (2009).

[29] F. C. Krebs, T. Tromholt, and M. Jogensen, Upscaling of polymer solar cell fabrication using full roll-to-roll processing, *Nanoscale* **2(6)**, 873-886 (2010).

[30] A. J. Medford, M. R. Lilliedal, M. Jogensen, D. Aaro, H. Pakalski, J. Fyenbo, and F. C. Krebs, Grid-connected polymer solar panels: initial considerations of cost, lifetime, and practicality, *Opt. Express* **18(S3 Suppl 3)**, A272-A285 (2010).

[31] H. Zhou, Y. Zhang, J. Seifter, S. D. Collins, C. Luo, G. C. Bazan, T.-Q. Nguyen, and A. J. Heeger, HighEfficiency Polymer Solar Cells Enhanced by Solvent Treatment, *Adv. Mater.* **25(11)**, 1646-1652 (2013).

[32] J. You, L. Dou, Z. Hong, G. Li, and Y. Yang, Recent trends in polymer tandem solar cell research, *Prog. Polym. Sci.* **38(12)**, 1909-1928 (2013).

[33] L. Dou, J. You, J. Yang, C.-C. Chen, Y. He, S. Murase, T. Moriarty, K. Emery, G. Li, and Y. Yang, Tandem polymer solar cells featuring a spectrally matched low-bandgap polymer, *Nat. Photonics* **6(3)**, 180-185 (2012).

[34] O. Hagemann, M. Bjerring, N. C. Nielsen, and F. C. Krebs, All solution processed tandem polymer solar cells based on thermocleavable materials, *Sol. Energy Mater. Sol. Cells* **92(11)**, 1327-1335 (2008).

[35] J. You, L. Dou, K. Yoshimura, T. Kato, K. Ohya, T. Moriarty, K. Emery, C.-C. Chen, J. Gao, G. Li, and Y. Yang, A polymer tandem solar cell with 10.6% power conversion efficiency, *Nat Commun.* **4**, 1446 (2013).

[36] W. Li, A. Furlan, K. H. Hendriks, M. M. Wienk, and R. A. J. Janssen, Efficient Tandem and Triple-Junction Polymer Solar Cells, *J. Am. Chem. Soc.* **135(15)**, 5529-5532 (2013).

[37] J. You, C.-C. Chen, Z. Hong, K. Yoshimura, K. Ohya, R. Xu, S. Ye, J. Gao, G. Li, and Y. Yang, 10.2% Power Conversion Efficiency Polymer Tandem Solar Cells Consisting of Two Identical Sub-Cells, *Adv. Mater.* **25(29)**, 3973-3978 (2013).

[38] A. Luque and S. Hegedus, Handbook of Photovoltaic Science and Engineering. Wiley, 2003.

[39] W. U. Huynh, J. J. Dittmer, and A. P. Alivisatos, Hybrid Nanorod-Polymer Solar Cells, *Science* **295(5564)**, 2425-2427 (2002).

[40] L. Song and A. Uddin, Design of high efficiency organic solar cell with light trapping, *Opt. Express* **20(S5 Suppl 5)**, A606-A621 (2012).

[41] W. E. I. Sha, W. C. H. Choy, Y. Wu, and W. C. Chew, Optical and electrical study of organic solar cells with a 2D grating anode, *Opt. Express* **20(3)**, 2572-2580 (2012).

[42] S. Y. Chou and W. Ding, Ultrathin, high-efficiency, broad-band, omni-acceptance, organic solar cells enhanced by plasmonic cavity with subwavelength hole array, *Opt. Express* **21(S1 Suppl 1)**, A60-A76 (2013).

[43] H. Shen, P. Bienstman, and B. Maes, Plasmonic absorption enhancement in organic solar cells with thin active layers, *J. Appl. Phys.* **106(7)**, 073109 (2009).

[44] I. Kim, D. S. Jeong, T. S. Lee, W. S. Lee, and K.-S. Lee, Plasmonic nanograting design for inverted polymer solar cells, *Opt. Express* **20(S5 Suppl 5)**, A729-A739 (2012).

[45] E. Stratakis and E. Kymakis, Nanoparticle-based plasmonic organic photovoltaic devices, *Mater. Today* **16(4)**, 133-146 (2013).

[46] Q. Gan, F. J. Bartoli, and Z. H. Kafafi, Plasmonic-Enhanced Organic Photovoltaics: Breaking the 10% Efficiency Barrier, *Adv. Mater.* **25(17)**, 2385-2396 (2013).

[47] Z. Ye, S. Chaudhary, P. Kuang, and K.-M. Ho, Broadband light absorption enhancement in polymer photovoltaics using metal nanowall gratings as transparent electrodes, *Opt. Express* **20(11)**, 12213-12221 (2012).

[48] K. Q. Le, A. Abass, B. Maes, P. Bienstman, and A. Al? Comparing plasmonic and dielectric gratings for absorption enhancement in thin-film organic solar cells, *Opt. Express* **20(S1)**, A39-A50 (2012).

[49] H. A. Atwater and A. Polman, Plasmonics for improved photovoltaic devices, *Nat. Mater.* **9(3)**, 205-213 (2010).

[50] B. Yu, S. Goodman, A. Abdelaziz, and D. M. O'Carroll, Light-management in ultra-thin polythiophene films using plasmonic monopole nanoantennas, *Appl. Phys. Lett.* **101(15)**, 151106 (2012).

[51] A. J. Nozik, Quantum dot solar cells, *Physica E* **14**, 115-120(2002).

[52] Y. J. Lee, Y. C. Yao, M. T. Tsai, A. F. Liu, M. D. Yang, and J. T. Lai, Current matching using CdSe quantum dots to enhance the power conversion efficiency of InGaP/GaAs/Ge tandem solar cells, *Opt. Express* **21(S6)**, A953-A963 (2013).

[53] C. Cheng and X. Wang, A Comparative Study of Spectral Characteristics of CdSe and CdSe/ZnS Quantum Dots, *International Symposium on Biophotonics, Nanophotonics and Metamaterials, 2006.* Metamaterials, 366−369 (2006).

[54] The experimental absorption data (A.U.) was obtained from solution and has been converted into absorption (%) using typical k values for bulk.

[55] J. N. Munday and H. A. Atwater, Large integrated absorption enhancement in plasmonic solar cells by combining metallic gratings and antireflection coatings, *Nano Lett.* **11(6)**, 2195-2201 (2011).

[56] J. N. Munday, The effect of photonic bandgap materials on the Shockley-Queisser limit, *J. Appl. Phys.* **112**, 064501 (2012)

[57] P. Krogstrup,*et al.*.Single−nanowire solar cells beyond the Shockley-Queisser limit, *Nat. Photon.* **7**, 306 (2013)

[58] M. A. Green, Third generation photovoltaics: Ultra-high conversion efficiency at low cost, *Progress in Photovoltaics: Research and Applications* **9**, 123 (2001)

[59] R. Ross and A. Nozik, Efficiency of hot-carrier solar energy converters, *J. Appl. Phys.* **53**, 3813-3818 (1982)

[60] M. C. Hanna and A. J. Nozik, Solar conversion efficiency of photovoltaic and photoelectrolysis cells with carrier multiplication absorbers, *J. Appl. Phys.* **100**, 074510 (2006)

[61] M. C. Putnam,*et al.*. Si microwire-array solar cells - Royal Society of Chemistry, *Energ. Environ. Sci.* **3**, 1037 (2010)

[62] C. Yang, *et al.* Self-Assembled Wire Arrays and ITO Contacts for Silicon Nanowire Solar Cell Applications, *Chin. Phys. Lett.* **28**, 035202 (2011)

[63] J. Wang, Z. Li, N. Singh, S. Lee, Highly−ordered vertical Si nanowirenanowall decorated solar cells, *Opt. Express* **19**, 23078 (2011)

[64] J. Y. Jung, K. Zhou, J. H. Bang and J. H. Lee, Improved Photovoltaic Performance of Si Nanowire Solar Cells Integrated with ZnSe Quantum Dots, *J. Phys. Chem. C* **116**, 12409 (2012)

[65] B. R. Huang, Y. K. Yang, T. C. Lin, W. L. Yang, A simple and low-cost technique for silicon nanowire arrays based solar cells, *Solar Energ. Mat. Solar Cells* **98**, 357 (2012)

[66] C. E. Kendrick,*et al.*. Radial junction silicon wire array solar cells fabricated by gold-catalyzed vapor−liquid−solid growth, *Appl. Phys. Lett.***97**, 143108 (2010)

[67] H. P. T. Nguyen, Y. L. Chang, I. Shih, Z. Mi, InN pin nanowire solar cells on Si, *IEEE. J. Sel. Top. Quantum Electron.* **17**, 1062 (2011)

[68] G. Mariani, A. C. Scofield, C. H. Hung, D. L. Huffaker, GaAs nanopillar-array solar cells employing in situ surface passivation, *Nat. Commun.* **4**, 1497 (2013)

[69] G. E. Cirlin, *et al.*. Photovoltaic properties of p-doped GaAs nanowire arrays grown on n-type GaAs (111) B substrate, *Nanoscale Res. Lett.* **5**, 360 (2010)

[70] E. Nakai, M. Yoshimura, K. Tomioka, T. Fukui, GaAsInGaP CoreMultishell Nanowire-Array-Based Solar Cells, *Jap. J. Appl. Phys.* **52**, 055002 (2013)

[71] G. Mariani, *et al.*. Patterned radial GaAs nanopillar solar cells, *Nano Lett.* **11**, 2490 (2011)

[72] J. Wallentin, *et al.*. InP nanowire array solar cells achieving 13.8% efficiency by exceeding the ray optics limit, *Science* **339**, 1057 (2013)

[73] Y. Cui, *et al.*. Efficiency enhancement of InP nanowire solar cells by surface cleaning, *Nano Lett.* **13**, 4113 (2013)

[74] M. Yoshimura, E. Nakai, K. Tomioka, T. Fukui, Indium phosphide coreshell nanowire array solar cells with lattice-mismatched window layer, *Appl. Phys. Express* **6**, 052301 (2013)

[75] H. Goto, *et al.*. Growth of coreshell InP nanowires for photovoltaic application by selective−area metal organic vapor phase epitaxy, *Appl. Phys. Express* **2**, 035004 (2009)

[76] L. C. Hirst and N. J. Ekins-Daukes, Fundamental losses in solar cells, *Progress in Photovoltaics: Research and Applications,* **19**, 286 (2011)

[77] A. Polman, H. A. Atwater, Photonic design principles for ultrahigh−efficiency photovoltaics, *Nat. Mater.* **11**, 174 (2012)

[78] U. Rau, U. W. Paetzold, T. and Kirchartz, Thermodynamics of light management in photovoltaic devices, *Phys. Rev. B.* **90**, 035211 (2014)

[79] C. Henry, Limiting efficiencies of ideal single and multiple energy gap terrestrial solar cells, *J. Appl. Phys.* **51**, 4494 (1980)

[80] W. Ruppel and P. Wurfel, Upper limit for the conversion of solar energy, *Electron Devices, IEEE Transactions* **27**, 877 (1980)

[81] T. Markvart, Thermodynamics of losses in photovoltaic conversion, *Appl. Phys. Lett.* **91**, 064102 (2007)

[82] M. A. Green, Limits on the open-circuit voltage and efficiency of silicon solar cells imposed by intrinsic Auger processes, *IEEE Transactions on Electron Devices* **31**, 671 (1984)

[83] P. Cambell,and M. A. Green, The limiting efficiency of silicon solar cells under concentrated sunlight, *IEEE Transactions on Electron Devices* **33**, 234-239 (1986)

[84] G. L. Araujo and A. Marti, Absolute limiting efficiencies for photovoltaic energy conversion, *Solar Energy Materials and Solar Cells* **33**, 213-240 (1994)

[85] A. Braun; E. A. Katz, D. Feuermann, B. M. Kayes, J. M. Gordon, Photovoltaic performance enhancement by external recycling of photon emission, *Energy & Environmental Science* **6**, 1499-1503 (2013)

[86] E. D. Kosten, B. M. Kayes, H. A. Atwater, Experimental demonstration of enhanced photon recycling in angle−restricted GaAs solar cells, *Energy & Environmental Science* **7**, 1907-1912 (2014)

[87] G. L. Araujo1 and A. Marti, Electroluminescence coupling in multiple quantum well diodes and solar cells, *Appl. Phys. Lett.* **66**, 894 (1995)

[88] V. Liu and S. Fan,*S*4 : A free electromagnetic solver for layered periodic structures, *Comp. Phys. Commun* **183**, 2233-2244 (2012)

[89] S. Sandhu, Z. Yu, S. Fan, Detailed balance analysis of nanophotonic solar cells, *Opt. Exp.* **21**, 1209-1217 (2013)

[90] S. Sandhu, Z. Yu, S. Fan, Detailed balance analysis and enhancement of open-circuit voltage in single−nanowire solar cells, *Nano Lett.* **14**, 1011-1015 (2014)

[91] N. Anttu, Shockley-Queisser detailed balance efficiency limit for nanowire solar cells, *ACS Photon.* **2**, 446-453 (2015)

[92] M. A. Green, K. Emery, Y. Hishikawa, W. Warta, E. D. Dunlop, Solar cell efficiency tables (Version 45), *Progress in Photovoltaics: Research and Applications* **22**, 1 (2014)

[93] B. M. Kayes, H. A. Atwater and N. S. Lewis, Comparison of the device physics principles of planar and radial pn junction nanorod solar cells, *J. Appl. Phys.* **97**, 114302 (2005)

[94] C. Colombo,*et al.*. Gallium arsenide pin radial structures for photovoltaic applications, *Appl. Phys. Lett.* **94**, 173108 (2009)

[95] M. D. Kelzenberg,*et al.*.Enhanced absorption and carrier collection in Si wire arrays for photovoltaic applications, *Nat. Mater.* **9**, 239 (2010)

[96] I. Schnitzer, E. Yablonovitch, C. Caneau, and T. J. Gmitter, Ultrahigh spontaneous emission quantum efficiency, 99.7% internally and 72% externally, from AlGaAsGaAsAlGaAs double heterostructures, *Appl. Phys. Lett.* **62**, 131-133 (1993)

[97] O. D. Miller, E. Yablonovitch and S. R. Kurtz, Strong internal and external luminescence as solar cells approach the Shockley-Queisser limit, *IEEE Jornal of P.V.* **2**, 303-311 (2012)

[98] H. J. Joyce,*et al.*. Ultralow surface recombination velocity in InP nanowires probed by terahertz spectroscopy, *Nano Lett.* **12**, 5325-5330 (2012)

[99] H. J. Joyce,*et al.*. Electronic properties of GaAs, InAs and InP nanowires studied by terahertz spectroscopy. *Nanotechnology* **24**, 214006 (2013)

[100] Y. Shen, *et al.*. Optical broadband angular selectivity, *Science* **343**, 1499-1501 (2014)

[101] Y. Shen, *et al.*. Metamaterial broadband angular selectivity, *Phys. Rev. B* **90**, 125422 (2014)

[102] C. D. Mathers, Upper limit of efficiency for photovoltaic solar cells, *J. Appl. Phys.*, **48**, 3181-3182, 1977.

[103] G. L. Araujo and A. Marti, Generalized detailed balance theory to calculate the maximum efficiency of solar cells, *presented at the 11th E.C. Photovoltaic Solar Energy Conf.*, Montreux, Switzerland, 1992.

[104] O. D. Miller and E. Yablonovitch, The physics required to approach the Shockley-Queisser limit, *presented at the 37th IEEE Photovoltaic Specialists Conf.*, Seattle, WA, USA, 2011.

[105] E. Rephaeli and S. Fan, Absorber and emitter for solar thermophotovoltaic systems to achieve efficiency exceeding the Shockley-Queisser limit, *Opt. Exp.*, **17**, 15145-15159, 2009.

[106] M. Florescu et al., Improving solar cell efficiency using photonic bandgap materials, *Sol. Energy Mater. Sol. Cells*, **91**, 1599-1610, 2007.

[107] E. Yablonovitch, Statistical ray optics, *J. Opt. Soc. Amer.*, **72**, 899-907, 1982.

[108] S. Fan, P. R. Villeneuve, J. D. Joannopoulos, and E. F. Schubert, High extraction efficiency of spontaneous emission from slabs of photonic crystals, *Phys. Rev. Lett.*, **78**, 3294-3297, 1997.

[109] A. Niv, Z. R. Abrams, M. Gharghi, C. Gladden, and X. Zhang, Overcoming the bandgap limitation on solar cell materials, *Appl. Phys. Lett.*, **100**, 083901-1-083901-4, 2012.

[110] T. Markvart, Beyond the Yablonovitch limit: Trapping light by frequency shift, *Appl. Phys. Lett.*, **98**, 071107-1-071107-2, 2011.

[111] C. Ulbrich, S. Fahr, J. Upping, M. Peters, T. Kirchartz, C. Rockstuhl, R. Wehrspohn, A. Gombert, F. Lederer, and U. Rau, Directional selectivity and ultra-light-trapping in solar cells, *Phys. Status Solidi*, **205**, 2831-2843, 2008.

[112] M. Peters, J. C. Goldschmidt, and B. Blasi, Angular confinement and concentration in photovoltaic converters, *Sol. Energy Mater. Sol. Cells*, **94**, 1393-1398, 2010.

[113] T. Markvart, Thermodynamics of losses in photovoltaic conversion, *Appl. Phys. Lett.*, **91**, 064102, 2007.

[114] M. Peters, C. Ulbrich, J. C. Goldschmidt, J. Fernandez, G. Siefer, and B. Blasi, Directionally selective light trapping in a germanium solar cell, *Opt. Exp.*, **19**, A136-A145, 2011.

[115] N. W. Ashcroft and N. D. Mermin, Solid state physics. *New York: Holt, Rinehart and Winston*, 1976.

[116] A. Y. Cho and J. R. Arthur, Molecular beam epitaxy, *Prog. Solid State Chem.*, **10**, 157191, 1975.

[117] F. Capasso, Band-Gap Engineering: From Physics and Materials to New Semiconductor Devices, *Science*, **235(4785)**, 172176, 1987.

[118] A. P. Alivisatos, Semiconductor Clusters, Nanocrystals, and Quantum Dots, *Science*, **271(5251)**, 933937, 1996.

[119] M. Nolan, S. OCallaghan, G. Fagas, J. C. Greer, and T. Frauenheim, Silicon Nanowire Band Gap Modification, *Nano Lett.*, **7(1)**, 3438, 2007.

[120] C. P. Kuo, S. K. Vong, R. M. Cohen, and G. B. Stringfellow, Effect of mismatch strain on band gap in IIIV semiconductors, *J. Appl. Phys.*, **57(12)**, 54285432, 1985.

[121] I. C. Bassignana, C. J. Miner, and N. Puetz, Photoluminescence and double-crystal xray study of InGaAs/InP: Effect of mismatch strain on band gap, *J. Appl. Phys.*, **65(11)**, 42994305, 1989.

[122] M. S. Leite, E. C. Warmann, G. M. Kimball, S. P. Burgos, D. M. Callahan, and H. A. Atwater, Wafer-Scale Strain Engineering of Ultrathin Semiconductor Crystalline Layers, *Adv. Mater.*, **23(33)**, 38013807, 2011.

[123] J. R. Snchez-Prez, C. Boztug, F. Chen, F. F. Sudradjat, D. M. Paskiewicz, R. B. Jacobson, M. G. Lagally, and R. Paiella, Direct-bandgap light-emitting germanium in tensilely strained nanomembranes, *Proc. Natl. Acad. Sci.*, **108(47)**, 889318898, 2011.

[124] T. Trupke, E. Daub, and P. Wrfel, Absorptivity of silicon solar cells obtained from luminescence, *Sol. Energy Mater. Sol. Cells*, **53(12)**, 103114, 1998.

[125] C. Barugkin, T. Allen, T. K. Chong, T. P. White, K. J. Weber, and K. R. Catchpole, Light trapping efficiency comparison of Si solar cell textures using spectral photoluminescence, *Opt. Express*, **23(7)**, A391, 2015.

[126] L. Patrone, D. Nelson, V. I. Safarov, M. Sentis, W. Marine, and S. Giorgio, Photoluminescence of silicon nanoclusters with reduced size dispersion produced by laser ablation, *J. Appl. Phys.*, **87(8)**, 38293837, 2000.

[127] M. A. Green, Solar cells: operating principles, technology, and system applications. *Englewood Cliffs, NJ: Prentice-Hall, Inc.*, 1982.

[128] P. Wurfel, Ed., Physics of Solar Cells: From Principles to New Concepts. *Weinheim, Germany: Wiley-VCH Verlag GmbH*, 2005.

[129] M. Wolf, G. T. Noel, and R. J. Stirn, Investigation of the double exponential in the current-Voltage characteristics of silicon solar cells, *IEEE Trans. Electron Devices*, **24(4)**, 419428, 1977.

[130] E.Purcell, Proceedings of the American Physical Society, *Physical Rev.* **69(11-12)**,674-674(1946)

[131] O. J. F. Martin, C. Girard, et al. Generalized Field Propagator for Electromagnetic Scattering and Light Confinement, *Phys. Rev. Let.* **74(4)**, 526-529(1995)

[132] E. Yablonovitch, Inhibited Spontaneous Emission in Solid-State Physics and Electronics, *Phys. Rev. Let.* **58(20)** 2059-2062(1987)

[133] D. Englund, D. Fattal, et al. Controlling the Spontaneous Emission Rate of Single Quantum Dots in a Two Dimensional Photonic Crystal, *Phys. Rev. Let.* **95(1)** 013904(2005)

[134] R. T. Ross, Some Thermodynamics of Photochemical Systems, *J. Chem. Phys.* **46(12)**, 4590-4593(1967)